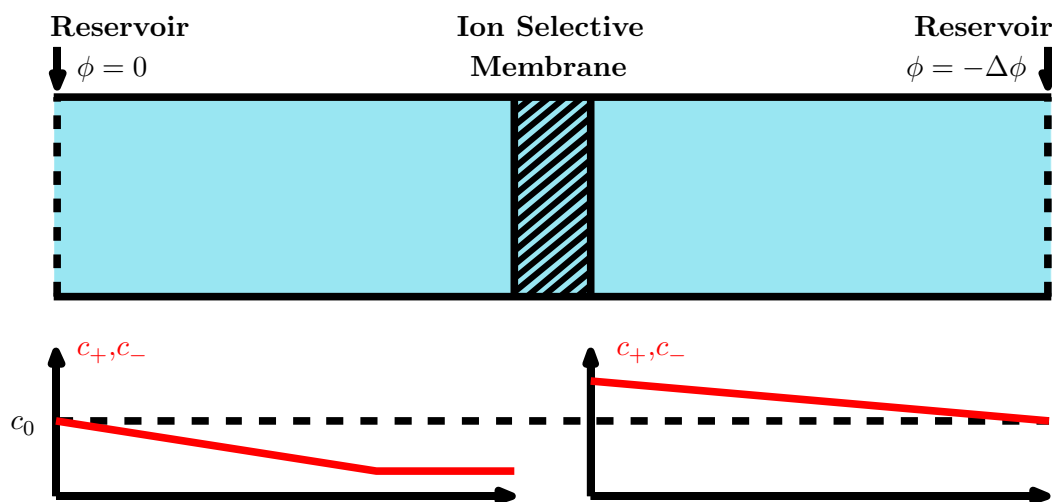


Master Thesis

Theory and finite-element modeling of electrokinetics in microchannels with permselective elements

Rasmus Dybbro Engelholm
s082613



Supervisor: Henrik Bruus

Department of Physics
Technical University of Denmark

14 October 2014

Abstract

In this thesis a numerical finite element model is developed and used to analyse the ion transport phenomena around of a non-ideal ion charge selective membrane in a microchannel. A novel design for the non-ideal ion charge selective membrane is made using a very narrow channel, with a surface charge that gives rise to a charged screening layer extending into the fluid. The advection through such an ion charge selective membrane is found to be important for the overall properties of the transport of ions, and for the distribution of ions around the membrane. Furthermore the effects of water self-ionization is included, and is seen to play an important role for the ion transport.

The numerical implementation is tested against exact and idealized analytical and numerical 1D models from the literature. This is done in the limits where they apply. The numerical model is found to give qualitatively acceptable results, with deviations that can be attributed to slightly different channel geometries.

The results of the numerical model developed can be used to directly compare to experiments, as the individual elements in the numerical model are designed to match those that are experimentally possible with state of the art clean room fabrication techniques.

Resumé

I denne afhandling er en numerisk finite element model opbygget og brugt til at analysere iontransport i og omkring en ikke ideel ionladningsselektiv membran i en mikrokanal. Et nyt design for en ikke ideel ionladningsselektiv membran er lavet ved brug af en meget tynd kanal, der grundet en overfladeladning har et ladet skærmlingslag, der rager ud i væsken på tværs af kanalen. Advektion igennem denne membran spiller en stor rolle for den overordnede transport af ioner, og for fordelingen af ioner omkring membranen. Derudover er effekten af vandsplitning inkluderet, og denne spiller en vigtig rolle for iontransporten.

Den numeriske implementering er sammenlignet med eksakte og idealiserede analytiske og numeriske 1D modeller fra litteraturen. Dette er gjort i de grænser, hvor disse er gyldige. Den numeriske model giver acceptable resultater med afvigelser, der kan tilskrives forskelle i kanalgeometrien.

Resultaterne af den udviklede numeriske model kan bruges til direkte sammenligning med eksperimenter, da de individuelle elementer i den numeriske model er designede til at matche dem, der er eksperimentelt mulige ved brug af state-of-the-art reentrums metoder.

Preface

The work done in this thesis is meant as a bridge between the theoretical work already done in the Theoretical Microfluidics Group at DTU over the past years, with experimental work. This means the goal is to develop a model that as closely as possible mimic geometry and physics in possible experiments. The focus is therefore not on making complex theories, but to test how the change of idealized elements into non-idealized elements impact the system. For this reason the assumption of a perfect reservoir is questioned, and a different approach to making an ion selective membrane is investigated. This also means that instead of working with cylindrical channels, which are difficult to make experimentally, rectangular channels are investigated. The hope is, at some point in the future, to compare the predictions by the developed model directly to experiments, in a way never done before.

Throughout the work, there has been many people providing invaluable assistance. Therefore i would like to use a couple of lines to thank them. First off, thanks to my supervisor, Henrik Bruus for making the project possible, for answering all my questions and especially for being patient during our discussions, even when I was not making any sense. I am grateful that the group members Christoffer P. Nielsen and Peter B. Muller provided feedback and helped me to understand the finer details, be it in COMSOL, the literature or the theory. Lastly I would like to thank my friends and family for support but especially Louise Floor Frellsen for invaluable feedback and sparring in writing the thesis.

signature

Rasmus Dybbro Engelsholm
Department of Physics
Technical University of Denmark
14 October 2014

Contents

List of figures	xii
List of tables	xiii
List of symbols	xv
1 Introduction	1
2 Short Introduction to the Finite Element Method	5
3 Gov. Eqns. for the Numerical Models	13
3.1 Navier-Stokes Equation	15
3.2 Continuity Equation	19
3.3 Poisson Equation	20
3.4 Ion Migration	22
3.5 Self-Ionization of Water	24
3.6 1D Boundary Conditions	26
3.7 Copy-Paste Friendly COMSOL Expressions	28
3.7.1 Without Water Splitting	28
3.7.2 With Water Splitting	33
4 Results and Comparison to Existing Work	39
4.1 Step 1	40
4.2 Step 2	41
4.3 Step 3	48
4.3.1 Models without advection - Dydek model	51
4.3.2 Models without advection - Yossifon model	55
4.3.3 Models with advection - Nielsen and Bruus model	58
4.3.4 Step 3 Summary	65
4.4 Step 4	65
4.5 Step 5	69
5 Conclusion and Outlook	73
A 1D Finite Element Code in Matlab	77

B 3D Images

79

List of Figures

1.1	Structure of investigations done throughout the thesis.	2
1.2	Structure of investigations done throughout the thesis.	4
2.1	Example of basis functions in 1D and 2D	6
2.2	A plot of the FEM example solution with different meshes	10
3.1	Graphical representation of types of boundaries in the problem with an example.	14
3.2	Arbitrary volume of fluid, Ω , considered in the derivations.	16
3.3	Graphical view of contradictory boundary conditions	27
4.1	1D model convergence and comparison to analytical expression	41
4.2	Sketch of the system with boundary conditions.	42
4.3	Figure showing mesh, velocity field and pressure field.	43
4.4	Comparison between numerical model and analytical mode, and boundary convergence test.	47
4.5	Sketch of the geometry used.	48
4.6	Mesh close to and inside nano channel.	49
4.7	Bulk mesh convergence analysis.	50
4.8	Comparison between numerical model and 1D model by Dydek.	53
4.9	Concentration profiles for numerical model and 1D model by Dydek.	54
4.10	Sketch of the Yossifon model.	55
4.11	Yossifon model comparison.	57
4.12	Comparison of the average ion current for different geometries in the 2D numerical model and the analytical model by Nielsen.	59
4.13	Velocity fields around different sized nano channels.	61
4.14	Ion selectivity for different geometries calculated by the numerical model.	63
4.15	Concentration profiles with and without advection in the numerical model.	64
4.16	Concentration profiles for numerical 2D model with water splitting but without advection and the model by Andersen.	66
4.17	Average current densities in the model with water splitting.	67
4.18	Comparison of the concentration profiles in 2D numerical model including water splitting, with and without advection.	68
4.19	Concentration and pH fields in full system.	70

4.20 Concentration and pH fields in full system.	71
B.1	80

List of Tables

List of symbols

Symbol	Description	Unit
x	Position coordinate one	m
y	Position coordinate two	m
z	Position coordinate three	m
ϕ	Electric potential	V
$\tilde{\phi}$	Normalized electric potential	
$\hat{\phi}$	Test function, electric potential	
$\tilde{\phi}_{BC}$	Normalized potential on boundary	
$\Delta\tilde{\phi}$	Potential difference, reservoirs	
c_+	Positive ion concentration	m^{-3}
c_-	negative ion concentration	m^{-3}
c_k	Ion concentration, species k	m^{-3}
\tilde{c}_k	Redefined ion concentration, species k	m^{-3}
\hat{c}_k	Test function, ion concentration, species k	m^{-3}
c_0	Normalization concentration	m^{-3}
λ_D	Debye length	m
E	Integrated relative error	
S	System matrix	
A	Overlap integral, self	
B	Overlap integral, adjacent	
N_{BC}	Neumann boundary condition	
D_{BC}	Dirichlet boundary condition	
μ_k	Chemical potential, species k	J
$\tilde{\mu}_k$	Normalized chemical potential, species k	
k_B	Boltmann constant	J K^{-1}
e	Electron charge	C
T	Temperature	K
Z_k	Oxidation number, species k	
ρ	Density of liquid	kg m^{-3}
v_i	Fluid velocity field, component i	m s^{-1}
\hat{v}_i	Test function, fluid velocity field, component i	m s^{-1}
n_i	Normal vector, component i	

Symbol	Description	Unit
σ_{ij}	Stress tensor	Pa
$\tilde{\sigma}_{ij}$	Redefined stress tensor	Pa
η	Dynamic Viscosity	Pa s
g_i	Gravitational acceleration, direction i	m s^{-2}
δ_{ij}	Delta function	
P	Pressure	Pa
\tilde{P}	Redefined Pressure	
\hat{P}	Test function, pressure	
ΔP	Pressure drop	Pa
P_{in}	Reservoir pressure	Pa
P_{out}	Reservoir pressure	Pa
ϵ	Dielectric constant for the fluid	F m^{-1}
α_ρ	Normalization constant	kg J^{-1}
α_η	Normalization constant	s
α_ϵ	Normalization constant	m^{-2}
σ_s	Surface charge	C m^{-2}
R_k	Reaction rate, species k	$\text{s}^{-1} \text{m}^{-3}$
J_{ik}	Ionic current, species k direction i	$\text{s}^{-1} \text{m}^{-2}$
\tilde{J}_{ik}	Normalized Ionic current, species k direction i	m s^{-1}
D_k	Diffusion constant, species k	$\text{s}^{-1} \text{m}^{-2}$
C_{Bk}	Reservoir bulk concentration, species k	m^{-3}
ϕ_{ext}	Externally applied electric potential	V
ϕ_{eq}	Equilibrium electric potential	V
$\tilde{\phi}_{eq}$	Normalized equilibrium electric potential	
$\hat{\phi}_{eq}$	Test function, equilibrium electric potential	
V_T	Thermal electric potential	V
K_{eq}		
K		
ρ_{el}	Electric charge density	C m^{-3}
u_{eo}	Electro-osmotic velocity field	m s^{-1}
u_P	Pressure driven velocity field	m s^{-1}
L	Size parameter(s) x direction	m
H	Size parameter(s) y direction	m
T_D	Boundary layer thickness	m
T_B	Bulk maximum mesh size	m
T_N	Nano channel maximum mesh size	m
G	Mesh growth factor	
R_N	Radius of curvature nano channel	m
R_M	Radius of curvature micro channel	m
\tilde{V}_D	Normalized electric potential difference over L_1	
Ω	Computational domain	
$\partial\Omega$	Domain boundary	
\mathbf{C}	Vector of solution coefficients	
\mathbf{R}	Vector of results coefficients	

Chapter 1

Introduction

Ionic solutions and their interaction with ion selective membranes are a part of everyday life. From ion pumps across the cell walls in our bodies, to power generation in fuel cells and large scale desalination of sea water. These applications are all based on how ion selective membranes work. However, despite the importance of these membranes, there are still effects that are not well understood.

The ion selective membrane system can be seen schematically in figure 1.1. When a potential is applied, the negatively charged ions move to the steady state configuration shown in the bottom part of the figure. The ions move until the gradient in the ion concentration fields leading to a diffusion ionic current exactly balances the ionic current from the applied electric field. The positively charged ions are free to pass the membrane, and therefore move to screen the negative charge while also carrying a current through the membrane. If we look at the concentration profiles in figure 1.1, at some point the concentration reaches zero, and cannot fall further. This creates a depletion zone close to the membrane. This should in turn lead to a zero limiting conductance, as there are no ions to carry the current. This is not what is seen experimentally, [17, 18], where there is always a so called overlimiting current (OLC). As shown in the recent review article by Ninenko et al., [13], many different explanations have been proposed over the years. From surface effects [5, 10, 11, 18], membrane discharge [1] to transport through the membrane by self ionization of water [12, 14]. All the effects depend heavily on the size of the channels in question.

Recently, through the advances made in silicon fabrication techniques, it has become possible to make very well defined micro meter sized channels, and even nano channels, [16]. This means it has become possible to fabricate a wide range of systems to experimentally test the different theoretical models, as done in [7, 18]. Most of these models measure current voltage relations or, more rarely, look at the water flow fields. A common problem with these experiments is the lack of direct measurements of the fields in the channels, for instance the concentration profiles. Instead they measure the sum of different effects. To circumvent this, one could measure the pH directly and spatially well resolved using

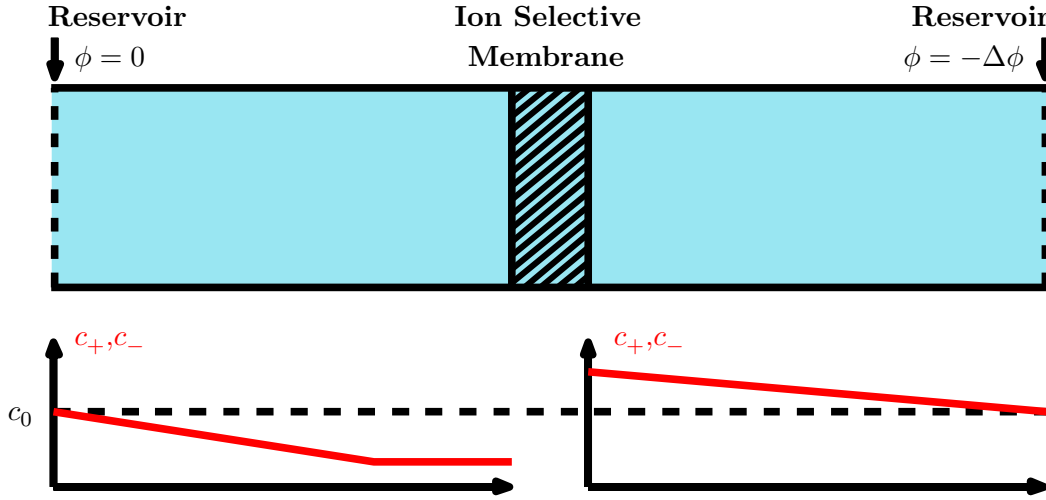


Figure 1.1: A sketch of a channel system between two reservoirs with the same ionic solution blocked by an ion selective membrane. The membrane only allows positive ions to pass. When there is a potential difference, $\Delta\phi > 0$, the positive (c_+) and negative (c_-) concentrations are redistributed as sketched in the drawn axes below the system sketch. The zone left of the membrane has a low concentration of ions and is known as the depletion zone.

the method proposed by Kneipp et al., [9]. With this method, quantitative comparison of spatial effects can be done inside the channels and can eventually be compared with the numerical models developed in this thesis.

The depletion zone is of particular interest due to the large decrease in ion concentrations. It is envisioned that it can be used for desalination. Some work has already been done in this area [8], but there has yet to be a convergence of the models and the emergence of an optimized design for desalination. Understanding the physics could help in this regard.

Returning to nano channels, it turns out that these can act as ion selective membranes, if they become small enough as seen by for instance Yossifon et al., [18]. This is due to surface reactions which give a surface charge, as demonstrated by Andersen et al., [3]. These can prevent ions of the same charge from entering the channel. This effect is cancelled if the distances involved are larger than the screening ion layer in the fluid. The characteristic length scale of the screening effects is the Debye length, λ_D , which is system dependant, but normally has values in the range 1 nm to 100 nm. This is therefore the approximate maximum size of the channels for which they can be expected to be ion selective. With the aforementioned advances in fabrication techniques, this could open a host of possibilities in engineering ion selective membranes. Currently there has, to my knowledge, not been done work with the sole purpose of investigating this.

With the above in mind, we can now formulate three overall goals for the work done in this master thesis:

1. **Membrane:** Instead of using a theoretical perfect ion selective membrane, this study will investigate a more realistic membrane system using a very narrow channel with overlapping Debye layers, which then acts as an ion selector.
2. **Advection:** It is only very recently that models including advection have been formulated, [11], and it seems to play an important role. Advection also most likely has an impact on the electrokinetics and flow through the ion selective nano channel. Both of these will be further investigated in this thesis.
3. **Reservoirs:** In a real physical system, there is nothing to prevent the concentrations and the potential to change across the reservoir. As ions start to move due to the external potential difference, there is nothing guaranteeing fixed concentrations at the entrance to the channel. If this is the case the boundary conditions imposed in general are wrong, and the possibility for experimental comparison is reduced. To fix this one could imagine flushing a solution past the opening to the system seen in figure 1.1. How this affects the channel membrane system will be investigated.

The three goals above are accomplished through a series of numerical investigations using the finite element method and the commercial solver COMSOL. The numerical model starts out very simple but is gradually extended to include more effects. During these extensions, the numerical results produced by the models are compared to known analytical models. In the end, the models will grow to a complexity that has yet to be modelled analytically, but the results can still be tested experimentally which is planned by collaborators at DTU. The stepwise investigation progression is shown graphically in figure 1.2. On the left the model is shown, while on the right the possible comparisons with literature are shown.

The five steps are:

1. 1D model to find potential and ion distribution between two charged walls. The result will be the reservoir boundary condition for the subsequent 2D models.
2. 2D model which incorporates the Navier-Stokes equation, the continuity equation and the ionic electro-diffusion-advection equations in an infinite parallel plate channel.
3. 2D model which has the same physics as in step two, but the geometry is now broken with a narrowing in the center. This nano meter sized channel acts as an ion selective membrane.
4. 2D model where the geometry and physics is the same as in step three, but now including water splitting.

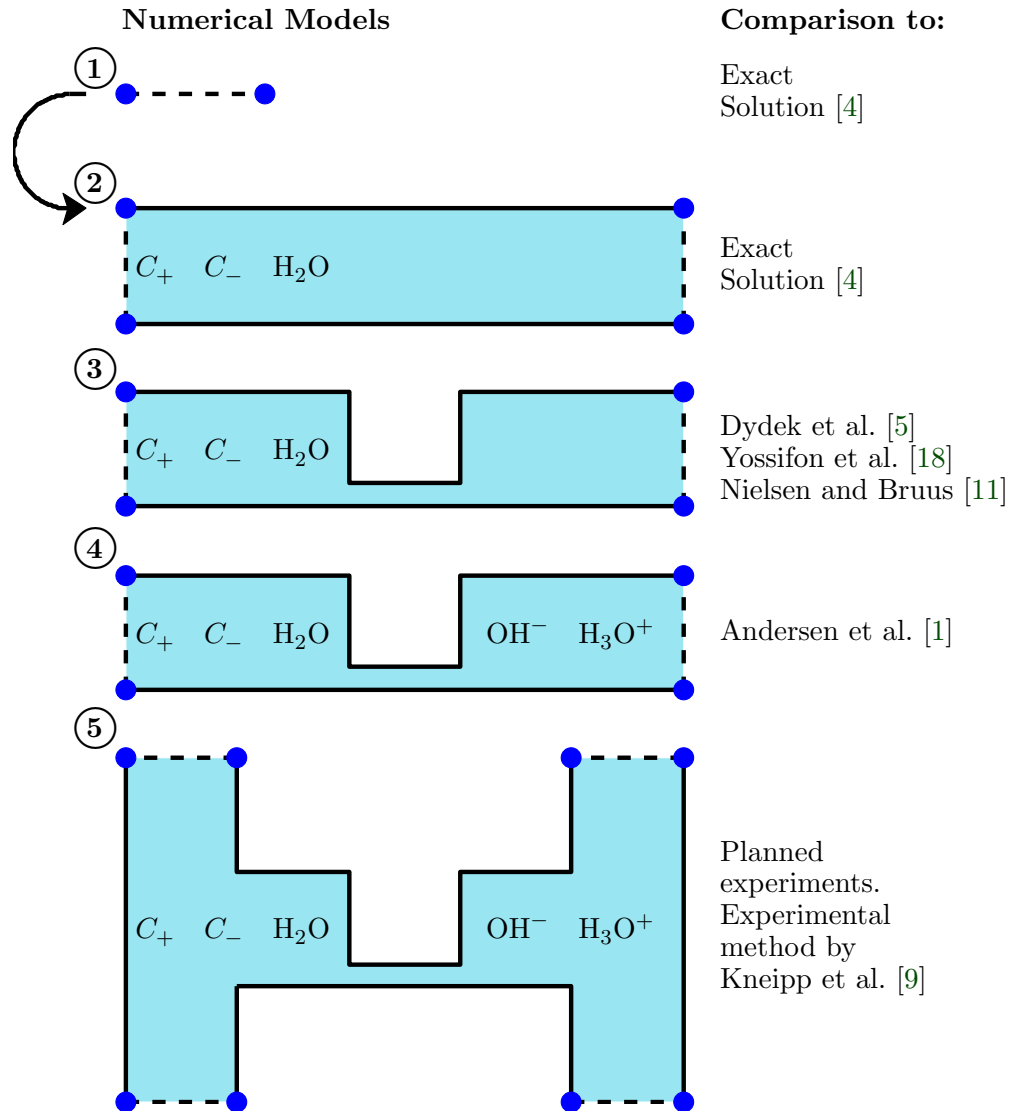


Figure 1.2: Stepwise progression for the numerical work. Each subsequent step is based on the model developed in the previous step. At each step the model is tested against known results. These are listed to the right of a given model in the figure. The narrowing in steps three to five is nano sized and thus ion selective.

- 2D model for the full system where what used to be reservoirs are now a steady stream of fresh ionic solution. This can be directly compared to experiments, which are planned to be carried out at DTU.

But before we get to testing the numerical model, we have to build it and solve it. Solving it is done using the finite element method which is introduced in chapter 2, after which the equations to solve are derived in chapter 3.

Chapter 2

Short Introduction to the Finite Element Method

In this chapter the finite element method (FEM) will be introduced through an example of a calculation in 1D. The idea is not to make a rigorous mathematical derivation, with multiple extensions such as non uniform meshing, higher order basis functions or faster solvers. For this see one of the many textbooks on the topic. Instead the focus will be on the central concept of the FEM - the local, analytically exact, integration of the test functions and the approximation that leads to this. Furthermore it is shown how to set up the matrix with boundary conditions. The purpose is to give the reader an idea of what is happening, when going from the governing equations to the numerical results, in the black box numerical solver in between. In the remaining report COMSOL version 4.4 is the numerical tool used. Experts in the finite element method can continue reading, or skip this chapter altogether at their own discretion.

The remaining text in this section will be focused on solving a simple differential equation,

$$\partial_x^2 y(x) + y(x) = 0. \quad (2.1)$$

To begin with, a Dirichlet type boundary condition is applied on one side, and a Neumann type boundary condition on the other, to show how both types are implemented. These are respectively

$$y(0) = 1 \quad \partial_x y(x)|_{x=\pi} = 0. \quad (2.2)$$

The above mentioned problem is an equation with the known analytical solution $\cos(x)$, and is thus not very interesting, but it will serve to illustrate the finite element method. However, first a short discussion of the mesh and its importance to the finite element method.

The basis functions used to solve the problem in equation (2.1) can be seen in figure 2.1. They are a set of functions, for which each individual function is centered on a different grid point (node). In general, each one should have an exact, known overlap integral with all other functions. This is the case for the chosen triangle functions. Problems

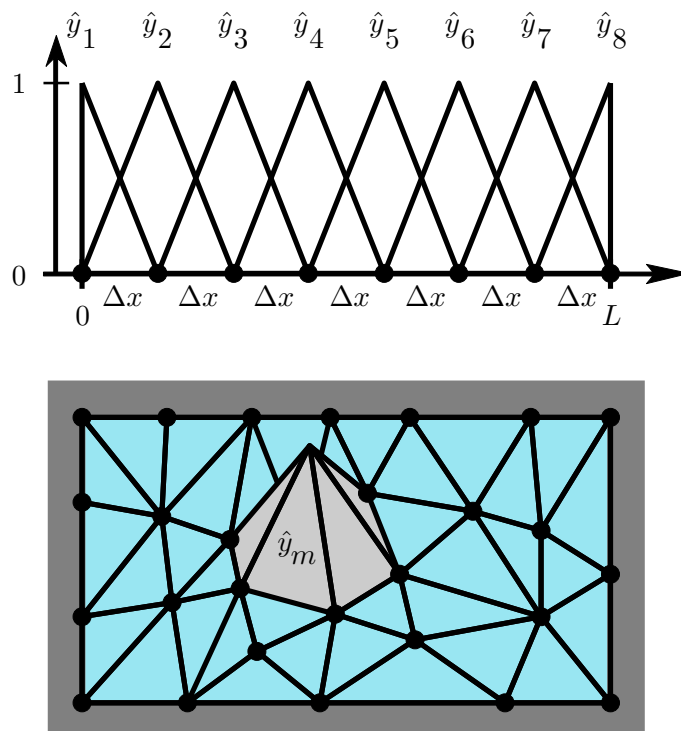


Figure 2.1: Top: The 1D mesh with all test functions visible and numbered. Each one is a triangle function with corners centred on three adjacent nodes (dark circles) and are non zero only within $\pm\Delta x$ around the center node. Bottom: The 2D mesh with only the m'th test function, \hat{y}_m , centered around the m'th node, shown for better visibility. The light blue area marks the bulk, denoted Ω , while the grey area around marks the boundary, denoted $\partial\Omega$. In both cases the functions are local, and the m'th test function is only non zero within the closest connected nodes.

involving higher order derivatives need a set of basis functions which has non zero higher order derivatives. If basis functions with insufficient higher order derivatives are used, the error in the solution might suffer tremendously depending on the problem, since part of the equation might always be zero. The example equation used throughout this section, equation (2.1), has second order derivatives. As just argued, this might be a problem since the triangle basis functions have a zero second order derivative. However, equation (2.1) can be rewritten to only include first order derivatives, and products of these. We should therefore be able to solve the problem with the mesh chosen. As we shall see when constructing the system matrix and solving it, the computational time is decreased tremendously if only basis functions which satisfy a requirement of being local are used.

After all these requirements for the basis functions, let us turn our attention to the approximation that is the basis for finite element solutions. That is, we assume any function

can be written as a linear combination of basis functions,

$$y(x) \approx \sum_{m=1}^M c_m \hat{y}_m(x). \quad (2.3)$$

To approximate $y(x)$ it is therefore necessary to find all the coefficients c_m . This is the overall goal in the finite element method. Exactly how to do this will be explained later. Immediately when reading an approximation, the following question should be asked: *Is equation (2.3) a good approximation and how can I check if it is?* In general, it is not. However, if the number of basis functions are increased, even the sum of straight line basis functions, or constant basis functions, approaches the original function,

$$\sum_{m=1}^M c_m \hat{y}_m(x) \rightarrow y(x) \quad \text{for } M \rightarrow \infty \quad (2.4)$$

The previous question was therefore not the proper question to ask. Instead the question should be: *How finely should I space my basis functions?* This question does not have a general answer, which is why it is necessary to perform a mesh convergence test for each problem. This is to ensure that the solution is always properly resolved and to get an idea of the magnitude of the implicit error. Normally a mesh convergence test means ensuring that the relative error, E of a characteristic parameter of the system is approaching zero exponentially with mesh improvements. In the example it could for instance be the error in y ,

$$E_y = \frac{\int_0^\pi \left| \sum_{m=1}^M c_m \hat{y}_m(x) - \cos(x) \right| dx}{\int_0^\pi |\cos(x)| dx}, \quad (2.5)$$

or if the derivative of y was the important parameter for the problem,

$$E_{\partial_x y} = \frac{\int_0^\pi \left| \sum_{m=1}^M c_m \partial_x \hat{y}_m(x) + \sin(x) \right| dx}{\int_0^\pi |\sin(x)| dx}. \quad (2.6)$$

As evident from the above considerations, both the spacing of the basis functions and the shape of the basis functions are two things that has to be consider in detail. Together these make up the mesh.

With the discussion of the mesh done, it is time to turn our attention towards solving the problem in equation (2.1). First we will look at what happens in the bulk (in 1D this means everything not on the boundary), and then look at how to implement Dirichlet and Neumann boundary conditions. First we multiply equation (2.1) with \hat{y}_n and then we integrate it. Thus we demand that the left hand side of equation (2.1), which might not

be zero when substituting in our basis functions, has to be orthogonal to any and all \hat{y}_n , so that the integral of the product is zero, for any n . For just a single n this would mean the error is not around the n 'th node. However since we demand it to be true for all n , it is the same as saying that the error is outside the domain described by the basis functions. For more information see the Galerkin method, [4, p.328]. The equation is then,

$$\int_0^\pi \hat{y}_n(x) \partial_x^2 y(x) + \hat{y}_n(x) y(x) dx = 0. \quad (2.7)$$

To best utilize our basis functions, and to avoid second derivatives in the equation (which will not be reflected in the basis functions since their second derivative is zero), a partial integration of the second order derivative term is carried out. The result is

$$[\hat{y}_n(x) \partial_x y(x)]_0^\pi + \int_0^\pi (-\partial_x \hat{y}_n(x)) \partial_x y(x) + \hat{y}_n(x) y(x) dx = 0. \quad (2.8)$$

where the boundary term is disregarded for now, but will be discussed later. Making the approximation in equation (2.3) and inserting it yields

$$\int_0^\pi (-\partial_x \hat{y}_n(x)) \partial_x \sum_{m=1}^M c_m \hat{y}_m(x) + \hat{y}_n(x) \sum_{m=1}^M c_m \hat{y}_m(x) dx = 0. \quad (2.9)$$

The sum can be taken outside the integral,

$$\sum_{m=1}^M c_m \left[\int_0^\pi (-\partial_x \hat{y}_n(x)) \partial_x \hat{y}_m(x) + \int_0^\pi \hat{y}_n(x) \hat{y}_m(x) \right] = 0, \quad (2.10)$$

and now it can be seen that the equation can be rewritten into a matrix equation where n corresponds to the n 'th row in the matrix,

$$\mathbf{S}\mathbf{C} = \mathbf{R}. \quad (2.11)$$

Here \mathbf{S} is the system matrix, \mathbf{C} is the vector of the coefficients c_m and \mathbf{R} is the results vector, with entries R_m . For now $\mathbf{R} = \mathbf{0}$, but in general it is not, and for this example it will change when imposing boundary conditions later. With the specific basis functions shown in figure 2.1 ($M = 8$), this matrix is an 8-by-8 sparse matrix. Sparse since, by construction, only neighbouring basis functions have a non zero overlap. Since a uniform mesh was used, the overlap integral is the same for any \hat{y}_m and \hat{y}_{m+1} and in reality only two different terms appear besides zero. These are the self interacting terms in the diagonal (A), and the terms to do with the interaction with the nearest neighbour (B). From equation (2.10),

$$A = \int_0^\pi (-\partial_x \hat{y}_m(x)) \partial_x \hat{y}_m(x) + \int_0^\pi \hat{y}_m(x) \hat{y}_m(x) = \frac{2}{3} \Delta x - \frac{2}{\Delta x}, \quad (2.12)$$

$$B = \int_0^\pi (-\partial_x \hat{y}_m(x)) \partial_x \hat{y}_{m+1}(x) + \int_0^\pi \hat{y}_m(x) \hat{y}_{m+1}(x) = \frac{1}{6} \Delta x - \frac{1}{\Delta x} dx/6 + 1/dx. \quad (2.13)$$

In the last equality the integration has been carried out for the basis functions used in the example. The full matrix is then

$$\mathbf{S} = \begin{bmatrix} \frac{1}{2}A & B & 0 & 0 & 0 & 0 & 0 & 0 \\ B & A & B & 0 & 0 & 0 & 0 & 0 \\ 0 & B & A & B & 0 & 0 & 0 & 0 \\ 0 & 0 & B & A & B & 0 & 0 & 0 \\ 0 & 0 & 0 & B & A & B & 0 & 0 \\ 0 & 0 & 0 & 0 & B & A & B & 0 \\ 0 & 0 & 0 & 0 & 0 & B & A & B \\ 0 & 0 & 0 & 0 & 0 & 0 & B & \frac{1}{2}A \end{bmatrix} \quad (2.14)$$

Now the general solution to the full bulk problem can be written as

$$\mathbf{C} = \mathbf{S}^{-1}\mathbf{R} \quad (2.15)$$

The inversion the system matrix is the central problem solved in any finite element solver, and depending on the size, it can be a difficult task. In COMSOL there are several different solvers to chose from. The common theme for all of them is that they are trying to approximate or find \mathbf{S}^{-1} while estimating the error. For more information on the different types, and how COMSOL does it, see [6]. In the remaining the MUMPS direct solver is used.

Returning to the boundary, there are two types of boundaries of interest, namely Neumann and Dirichlet.

To set the value of the solution function on the boundary, $y(x) = D_{BC}$, which is the Dirichlet type, we see that only basis functions centered on the boundary contribute. Picking the n 'th node to be the boundary we wish to set the value on, we need to force $c_n = D_{BC}$ on that particular boundary. Writing up the n 'th row in the matrix, which is the equation for that node, yields

$$S_{n,n-1}c_{n-1} + S_{n,n}c_n + S_{n,n+1}c_{n+1} = R_n. \quad (2.16)$$

From this we can see that the only solution independent of c_{n-1} and c_{n+1} is

$$S_{n,n-1} = 0 \quad S_{n,n+1}c_{n+1} = 0 \quad S_{n,n} = \frac{R_n}{D_{BC}}. \quad (2.17)$$

This is the Dirichlet type boundary condition.

To set the derivative of the solution on the boundary, $\partial_x y(x) = N_{BC}$, which is the Neumann type boundary condition, it is necessary to specify on which side of the node we want to set the derivative, as the derivative on the node is undefined. Since we want to set it on the boundary, the function is only defined on the inside of the object. From the definition of the basis functions we see that the derivative is

$$\frac{c_n - c_{n-1}}{\Delta x} = N_{BC}. \quad (2.18)$$

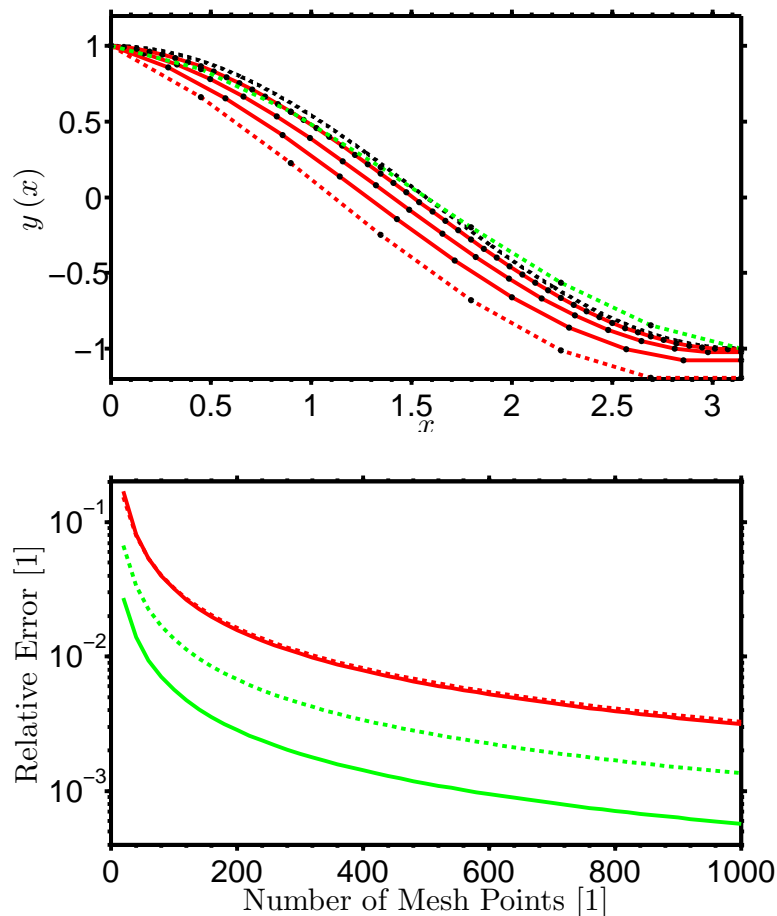


Figure 2.2: Top: Finite element solution to the problem stated in equation (2.1). The black dots mark the center of the basis function for that line. The dashed red line is for Dirichlet + Neumann boundary conditions (8 mesh points), while the dashed green is for double Dirichlet boundary conditions (8 mesh points). The red lines are the same as the dashed red, but with finer meshes (12, 20 and 50 mesh points). The black dashed line is the exact solution. Bottom: Convergence analysis for the problem in the top figure. The colors correspond to those in the top part. The full lines are calculated using equation (2.5), while the dashed lines are calculated using equation (2.6). The Matlab code which was used to solve the problem can be seen in appendix A.

This has two solutions depending on which side of the node is inside. Here both are reported as a view of the part of the matrix centered on the node on which the derivative

is set.

$$\begin{bmatrix} A & 0 & 0 \\ -A & A & 0 \\ 0 & 0 & A \end{bmatrix} \begin{bmatrix} c_{n-1} \\ c_n \\ c_{n+1} \end{bmatrix} = \begin{bmatrix} 0 \\ N_{BC}A\Delta x \\ 0 \end{bmatrix}, \quad \begin{bmatrix} A & 0 & 0 \\ 0 & -A & A \\ 0 & 0 & A \end{bmatrix} \begin{bmatrix} c_{n-1} \\ c_n \\ c_{n+1} \end{bmatrix} = \begin{bmatrix} 0 \\ N_{BC}A\Delta x \\ 0 \end{bmatrix}. \quad (2.19)$$

The full matrix equation for the case which we have treated so far, for Dirichlet at node $n = 1$, and Neumann at node $n = 8$, is then

$$\begin{bmatrix} A & 0 & 0 & 0 & 0 & 0 & 0 & 0 \\ B & A & B & 0 & 0 & 0 & 0 & 0 \\ 0 & B & A & B & 0 & 0 & 0 & 0 \\ 0 & 0 & B & A & B & 0 & 0 & 0 \\ 0 & 0 & 0 & B & A & B & 0 & 0 \\ 0 & 0 & 0 & 0 & B & A & B & 0 \\ 0 & 0 & 0 & 0 & 0 & B & A & 0 \\ 0 & 0 & 0 & 0 & 0 & 0 & -A & A \end{bmatrix} \begin{bmatrix} c_1 \\ c_2 \\ c_3 \\ c_4 \\ c_5 \\ c_6 \\ c_7 \\ c_8 \end{bmatrix} = \begin{bmatrix} AD_{BC} \\ 0 \\ 0 \\ 0 \\ 0 \\ 0 \\ 0 \\ AN_{BC}\Delta x \end{bmatrix}. \quad (2.20)$$

One could have divided with A in the first and last row, but this should not be done as, in general, it is better to keep the whole matrix in the same numerical order of magnitude, and then scale the whole thing, to get maximum numerical precision.

The solution to this system, with mixed Neumann and Dirichlet boundary conditions, and the system with Dirichlet type boundary conditions at both sides, can be seen in figure 2.2. The double Dirichlet boundary conditions for the second type were picked so that the solution would be the same as the solution to the mixed case. As is evident from the graph, the exponential approach to the correct solution is reached after about 400 mesh points. This indicates that the solution is converged in the sense that it quickly approaches the correct solution monotonically without surprises. The number of mesh points required is significantly higher than what you would estimate by eye, which would be about 50 to 100 for the mixed boundary condition case. The onset of the exponential approach does not seem to depend on the method of error calculation for either case. Also as expected using equation (2.5) for error estimation is more suited for problems involving only Dirichlet boundary conditions, while both methods seem equally good for the mixed boundary conditions.

To sum up this chapter, an example of how to go from equation to solution using the finite element method has been demonstrated in 1D. The equation and problem presented accurately describes the basic attributes of the finite element method, and it is the method which will be used for the numerical work done throughout the thesis. However the example fails to predict some of the problems encountered when the system is 2D, with multiple variable non linear equations and increasing mesh points.

Chapter 3

Governing Equations for the Numerical Models

To make a model of some system or phenomena, and explain it in an understandable way, it is necessary to have a shared foundation between reader and writer. From there, it is possible to explain all the steps in detail to prevent the reader from getting lost. Since the governing equations act as the foundation for the investigation, it is natural to spend extra pages to describe them in detail, so the reader will better grasp the concepts. Therefore there might be sections in this part that seem a little trivial for anyone experienced in the field. If so, read by skimming, and take delight in renewing old knowledge.

The goals of this section are to introduce the system of equations used, to explain the boundary conditions required, and transform both of these into the weak form used in COMSOL. To do this for the different equations, several subsections follow, one for each equation. In order to have a clear idea of where the individual boundary condition apply, four main types are necessary as seen in figure 3.1. The main distinction is between open and closed walls, as these two share the least boundary conditions. Open boundary condition allows fluid and particles to flow in and out, whereas the wall type represent physical solid walls. The type of frame in this figure, corresponds to a type of line on the boundaries in the following figures. Each set of boundary conditions is assigned one of these color codes, so it is easy to see what is applied where. Walls are solid lines, whereas dashed lines mean open boundaries. This is enough to distinguish between the needed boundary conditions for, for instance, the velocity field or the particle current on the walls. If this is the case, the color code will be black, meaning no need for further division of type. But for some phenomena, for instance wall charge or type of flow in and out of the system, a further subdividing is needed. The color represents this. An example of this color code system can be seen in figure 3.1.

Leaving the boundaries for a bit, and returning to the governing equations and their implementation in COMSOL, it should be noted that the right hand side of the equation is always assumed to be zero in COMSOL. This is the form that the equations will be in.

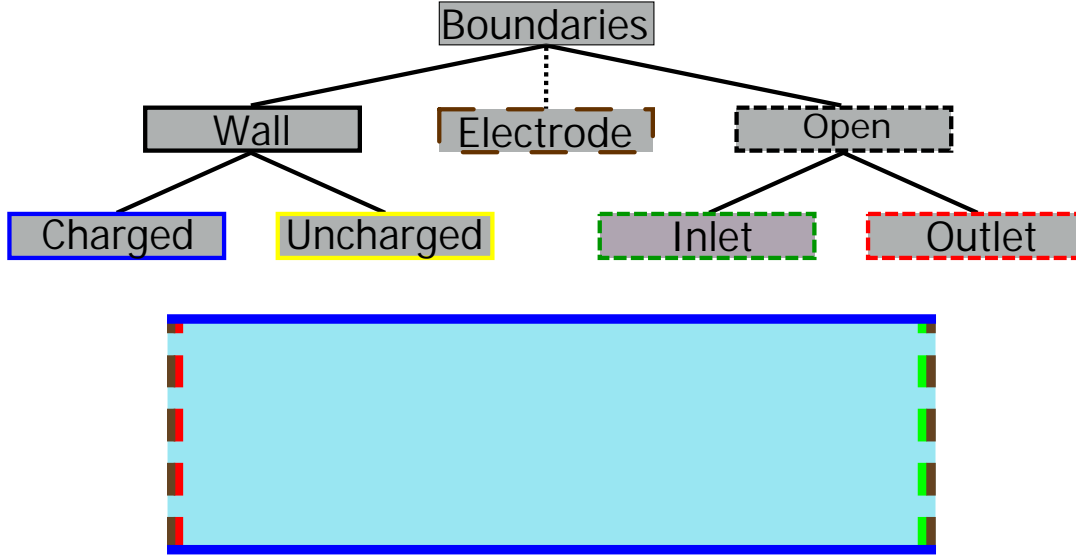


Figure 3.1: Top: Graphical representation of the different types of boundaries, and the procedural subdividing of these into four mutually exclusive basic types necessary to describe the different boundary conditions imposed on the different variables. The color and type of the frame for each box corresponds to the type of line that will be used in the structure figures to represent the boundaries used. The "Electrode" box is a joker, in the sense that it can be applied anywhere, but in most cases it overwrites or changes all other boundary conditions on that particular boundary. Bottom: Straight line channel with the color code in place. There is a higher pressure on the right side, than on the left, and both these boundaries are open. The top and bottom sides, here blue, are charged walls. Incidentally this is also the first studied test case for the numerical model.

Also, in all cases only the stationary incompressible form is considered so that all time and density derivatives are zero. The index notation indices, i and j , can run over two Cartesian coordinates (Translational invariant 2D model) or three Cartesian coordinates (Full 3D model), x , y and z . Also the differential operator with respect to these coordinates is shortened to ∂_i . Due to the expression for the chemical potential as a function of the charge concentration, it is advantageous, for the sake of quick and reliable convergence of the solution in COMSOL, to redefine the charge concentration. This is to get rid of the logarithmic dependence which has the property that a small error in the potential can give a large error in concentration (and vice versa), leading to slow convergence and possibly numerical errors. Small numerical fluctuations in the concentration could also lead to negative concentrations, and subsequent unphysical solutions. Also instead of working with orders of magnitude differences, if the concentration approaches zero in some areas, a more continuous concentration profile is obtained. All these issues are resolved through a simple transformation of variable

$$\tilde{c}_k \equiv \log \left(\frac{c_k}{c_0} \right) \Rightarrow c_k = c_0 \exp(\tilde{c}_k), \quad (3.1)$$

where c_k is the physical variable, c_0 is the scaling constant, both having the unit of m^{-3} , and \tilde{c}_k is the introduced unitless variable. In fact, the tilde will be used to mark all the transformed variables that are used, while the hat variables, like \hat{c}_k , are exclusively test functions for their respective variables. In the following all summations over k means summation over all ion species, and k subscripts refers to an ion type. For salt water, taking into account the self ionization of water, this could for instance mean that k could be Na^+ , Cl^- , H_3O^+ or OH^- .

Just as it is convenient to redefine the concentration, it is also convenient to work directly in the chemical potential. The chemical potential is defined as

$$\mu_k = k_{\text{B}}T \log\left(\frac{c_k}{c_0}\right) + Z_k e \phi = k_{\text{B}}T \tilde{c}_k + Z_k e \phi, \quad (3.2)$$

where, in the last equal sign, the expression for the dimensionless concentration variable has been inserted, and Z_k is the number of electron charges a single ion has, compared to its atomic state. For instance $Z_{\text{OH}^-} = -1$, while $Z_{\text{Ca}^{2+}} = 2$. The non dimensionalized version of this is

$$\tilde{\mu}_k = \frac{\mu_k}{k_{\text{B}}T} = \tilde{c}_k + \frac{Z_k e}{k_{\text{B}}T} \phi = \tilde{c}_k + Z_k \tilde{\phi} \Rightarrow \partial_i \tilde{\mu}_k = \partial_i \tilde{c}_k + Z_k \partial_i \tilde{\phi}, \quad (3.3)$$

where also the non dimensionalized potential, defined by

$$\tilde{\phi} = \frac{e}{k_{\text{B}}T} \phi, \quad (3.4)$$

has been used. How the chemical potential is used will be shown when working with the Navier-Stokes equation, but the aim is to redefine the pressure variable into a more natural energy density variable for the system. As it turns out, this redefined pressure has no derivative perpendicular to the walls, which makes boundary conditions easier, and furthermore it enables us to have the osmotic pressure driving term directly in the Navier-Stokes equation.

3.1 Navier-Stokes Equation

In order to get the best results in the numerical scheme, it is usually best to start with a general version of an equation, instead of derived equations. Therefore let us start by observing an arbitrary geometric shape, Ω , for instance the one seen in figure 3.2.

The change in momentum inside Ω in time must be equal to the sum of the surface integrals over the momentum passing through the surface due to convection and the stress forces acting on the surface and the volume integral over any body forces. This can be seen to give

$$\partial_t \int_{\Omega} (\rho v_i) dV = \int_{\partial\Omega} n_j [-\rho v_i v_j + \sigma_{ij}] dA + \int_{\Omega} \rho g_i - c_0 e \sum_k Z_k \exp(\tilde{c}_k) \partial_i \phi dV, \quad (3.5)$$

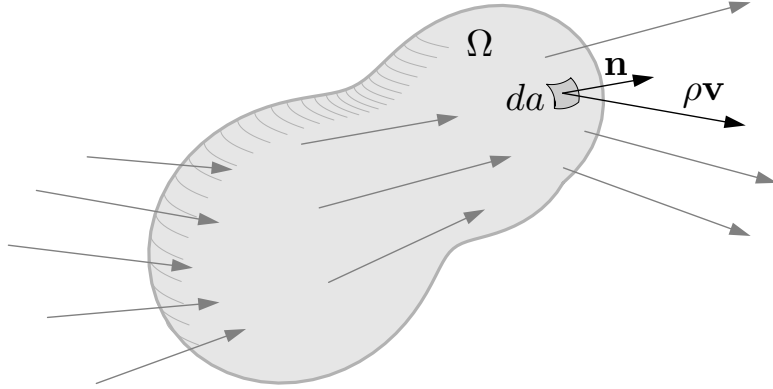


Figure 3.2: Arbitrary geometric shape, Ω , used to derive Navier-Stokes equation and the continuity equation. Depending on the field in consideration, the arrows can be representing mass flow as denoted on this figure or momentum flow, in which case $\rho \mathbf{v}$ would be substituted by $(\rho \mathbf{v}) \mathbf{v}$ (note the absence of a dot - it is not a dot product, but results in a tensor). Image from *Theoretical Microfluidics* by Henrik Bruus [4].

where σ_{ij} is the full stress tensor, including the pressure, and v is the velocity field. By considering only the case of hydrostatic equilibrium, we know that the gravity force is precisely counterbalanced by the hydrostatic pressure. Therefore the gravity force is removed from the equation and the pressure is now a pressure in zero gravity. The true pressure can always be recovered by adding a $\rho g z$ term, with z being zero at the surface, and pointing along the direction of gravitational acceleration. As mentioned we are looking for steady state solutions, so the term with the time derivative, the whole left side of the equation, can be set to zero. After applying the Gauss theorem to change the surface integral to a volume integral and combining the whole right side under one volume integral,

$$0 = \int_{\Omega} \partial_j [-\rho v_i v_j + \sigma_{ij}] - c_0 e \sum_k Z_k \exp(\tilde{c}_k) \partial_i \phi \, dV, \quad (3.6)$$

it can be argued, that since the volume is arbitrary in size and shape, the function under the integral has to be zero at all points,

$$0 = \partial_j [-\rho v_i v_j + \sigma_{ij}] - c_0 e \sum_k Z_k \exp(\tilde{c}_k) \partial_i \phi. \quad (3.7)$$

Here e is the electron charge. The main difference between this, and the usual Navier-Stokes expression lies in the advection term $(\partial_j \rho v_i v_j)$. Here the continuity equation is not used to reduce the equation, and therefore the divergence is of the whole expression. From experience, it is advantageous to write the equations in their purest form, since this often avoids weird mixed boundary conditions or terms that almost cancel each other out, both of which could lead to slow convergence.

Instead of working directly with equation (3.7), it is advantageous to recast it by transforming the potential term into the chemical potential, by adding and subtracting concentration terms

$$0 = \partial_j [-\rho v_i v_j + \sigma_{ij}] - c_0 e \sum_k Z_k \exp(\tilde{c}_k) \partial_i \phi + k_B T c_0 \sum_k \exp(\tilde{c}_k) \partial_i \tilde{c}_k - k_B T c_0 \sum_k \exp(\tilde{c}_k) \partial_i \tilde{c}_k, \quad (3.8a)$$

$$0 = \partial_j [-\rho v_i v_j + \sigma_{ij}] - \sum_k k_B T c_0 \exp(\tilde{c}_k) \left[Z_k \partial_i \tilde{\phi} + \partial_i \tilde{c}_k \right] + k_B T \sum_k c_0 \exp(\tilde{c}_k) \partial_i \tilde{c}_k, \quad (3.8b)$$

$$0 = \partial_j [-\rho v_i v_j + \sigma_{ij}] - \sum_k k_B T c_0 \exp(\tilde{c}_k) \partial_i \tilde{\mu}_k + k_B T \sum_k c_0 \exp(\tilde{c}_k) \partial_i \tilde{c}_k, \quad (3.8c)$$

where equation (3.3) has been used to get from equation (3.8b) to equation (3.8c). Finally the new pressure and equation can be achieved by dividing with the thermal energy density $k_B T c_0$, and pulling the added terms with derivatives of c_k into the pressure in the stress tensor, since it can be rewritten into gradient form, $\exp(\tilde{c}_k) \partial_i \tilde{c}_k = \partial_i \exp(\tilde{c}_k)$. This leaves a few terms

$$0 = \partial_j \left[-\frac{\rho}{k_B T c_0} v_i v_j + \frac{\tilde{\sigma}_{ij}}{k_B T c_0} \right] - \sum_k \exp(\tilde{c}_k) \partial_i \tilde{\mu}_k, \quad (3.9)$$

where $\tilde{\sigma}_{ij}$ is given by

$$\frac{\tilde{\sigma}_{ij}}{k_B T c_0} = -\frac{\delta_{ij} P}{k_B T c_0} + \frac{\eta}{k_B T c_0} (\partial_i v_j + \partial_j v_i) + \delta_{ij} \sum_k \exp(\tilde{c}_k), \quad (3.10)$$

and η and ρ are respectively the viscosity and density of the fluid. With everything inserted, this leads to the following equation, where two new constants, α_ρ and α_η , are introduced, along with the new energy density (redefined pressure), \tilde{P} .

$$0 = \partial_j \left[-\alpha_\rho v_i v_j - \delta_{ij} \tilde{P} + \alpha_\eta (\partial_i v_j + \partial_j v_i) \right] - \sum_k \exp(\tilde{c}_k) \partial_i \tilde{\mu}_k, \quad (3.11a)$$

$$\alpha_\rho = \frac{\rho}{k_B T c_0} \quad [\alpha_\rho] = \text{kg J}^{-1}, \quad (3.11b)$$

$$\alpha_\eta = \frac{\eta}{k_B T c_0} \quad [\alpha_\eta] = \text{s}, \quad (3.11c)$$

$$\tilde{P} = \frac{P}{k_B T c_0} - \sum_k \exp(\tilde{c}_k). \quad (3.11d)$$

It might seem like it was a lot of work to make this change of variable, but now it can be argued why it is beneficial to do. The osmotic pressure force arising from the gradient in the concentrations, which is especially strong close to the charged walls due to the

formation of the Debye layer, is now directly included in the Navier-Stokes equation. The overall effect is to reduce the complexity of the matrix equation that is solved. This also means that the problem is better decoupled in the two directions parallel and perpendicular to the wall, which makes analytical modelling and calculations much easier.

From here the equation can be cast into weak form by multiplying with the velocity field test function, \hat{v}_i , and integrating,

$$0 = \int_{\Omega} \hat{v}_i \partial_j \left(-\alpha_{\rho} v_i v_j - \delta_{ij} \tilde{P} + \alpha_{\eta} (\partial_i v_j + \partial_j v_i) \right) dV - \int_{\Omega} \hat{v}_i \sum_k \exp(\tilde{c}_k) \partial_i \tilde{\mu}_k dV, \quad (3.12a)$$

$$0 = \left[n_j \hat{v}_i \left(-\alpha_{\rho} v_i v_j - \delta_{ij} \tilde{P} + \alpha_{\eta} (\partial_i v_j + \partial_j v_i) \right) \right]_{\partial\Omega} + \int_{\Omega} (-\partial_j \hat{v}_i) \left(-\alpha_{\rho} v_i v_j - \delta_{ij} \tilde{P} + \alpha_{\eta} (\partial_i v_j + \partial_j v_i) \right) dV - \int_{\Omega} \hat{v}_i \sum_k \exp(\tilde{c}_k) \partial_i \tilde{\mu}_k dV, \quad (3.12b)$$

where integration by parts has been used to decrease the order of the derivative of the velocity field by one, by transferring it to the test function for the velocity field. This is done to minimize errors. It is expected that the test function and the function itself has the same order of magnitude errors when the solution is converged, $\hat{v}_i \approx v_i$, so distributing the derivatives should yield the best results.

To implement this in COMSOL, the equation is split in two parts. One is the weak form volume integrals, and one is what happens on the boundary. The volume integrals are the easiest, as COMSOL accepts the input in weak form directly. A copy paste friendly version for 2D can be found in section 3.7.

In order to get the implementation right however, the boundary terms are just as important. As explained in the beginning of this chapter, there are several different boundaries. Each of them will be explained in several bulletpoint lists, one for each governing equation. The first (which is in this subsection) is for the Navier-Stokes equation and the velocity field. The final derived 2D equations, without explanations, can be seen in COMSOL-ready, copy-paste friendly equation blocks in section 3.7 for both bulk and boundaries.

Wall BC - Solid Lines From equation (3.12b) it is clear that the volume integral is not enough on the boundaries. There is a boundary specific term, and the sum of this and the volume term is what has to be zero on the boundary. Therefore a weak contribution is added on all boundaries. This term is:

$$\left[n_j \hat{v}_i \left(-\alpha_{\rho} v_i v_j - \tilde{P} + \alpha_{\eta} (\partial_i v_j + \partial_j v_i) \right) \right]_{\partial\Omega} \quad (3.13)$$

However, as it is a direct extension of the bulk physics, it is overwritten by what we know is the actual physics of the boundary. Therefore it has to work in conjunction with the next bulletpoint (which is a single boundary condition), and be overwritten by the third and last bulletpoint (which consists of two simultaneous boundary conditions), so that there is always a total of two boundary conditions.

Wall BC - Solid Lines The constraint on the solid walls are the usual no slip condition, deriving from the idea of the outmost layers of atoms not moving. So all velocity field components are zero at the walls:

$$v_i = 0. \quad (3.14)$$

Open BC - Dashed Lines At the inlet and outlet, a perfectly laminar flow is assumed. This means that the components along the boundary is zero, and that the derivative perpendicular to the boundary is zero. The easiest way to think about it, is as the open boundaries connecting to a Poiseuille type flow channel. Mathematically this gives the following constraints (parenthesis as a reading aid):

$$0 = (n_j \partial_j) (v_i n_i), \quad (3.15a)$$

$$0 = -n_y v_x + n_x v_y. \quad (3.15b)$$

To properly implement this, Lagrange multipliers are used on the boundary in question. In COMSOL this is done through the addition of an auxillary equations subnode. This method could also be used to collect the previous boundary conditions into one combined, but this is not done here.

3.2 Continuity Equation

As opposed to the very long section on the Navier-Stokes equation, this will be very short. For incompressible fluids in steady state, the same volume of fluid must enter and leave an arbitrary shape, Ω , as the one seen on figure 3.2. This means the surface integral of the flow must be zero,

$$0 = \int_{\partial\Omega} n_i v_i \, dA, \quad (3.16)$$

where n_i is the components of the surface normal vector. Again, by using Gauss theorem, and removing the integral since the volume was arbitrarily chosen, the usual continuity equation is derived,

$$0 = \partial_i v_i, \quad (3.17)$$

To get into weak form, the test function for the pressure, \tilde{P} , is multiplied, and the whole thing integrated,

$$0 = \int_{\Omega} \hat{P} \partial_i v_i \, dV, \quad (3.18)$$

which is directly applicable to COMSOL, with same accuracy as in the Navier-Stokes equation, as the pressure and the derivative of the velocity field are in both expressions.

The boundary terms needed to solve the problem are very easy to get. From equation (3.18) it can be seen that the pressure test function works as a Lagrange multiplier, and therefore is a slave variable to the velocity field. Therefore no direct boundary terms are necessary. But in most experiments there are two ways to ensure a controlled flow into the

system. It can be done with either a flow controller, where the velocity profile is known, or by applying a pressure. The latter option requires boundary terms on the pressure as follows

Inlet BC - Dashed Green Lines On the inlet boundary, it is assumed that the fluid flow is laminar and since the channel, in the physical system, is the same on both sides of the boundary, the flow should be the same if the boundary was moved a bit. This corresponds to a Poiseuille flow, and as such we know that there is an unknown pressure gradient and that the flow profile should be unchanged as argued in the Navier-Stokes boundary conditions. But we do control the pressure and can set it to some known value, P_{in} , by using a constraint.

$$0 = P - P_{in} \quad (3.19)$$

Outlet BC - Dashed Red Lines The argument used for the inlet can be used again, this time it is just a different pressure, used to drive the fluid.

$$0 = P - P_{out} \quad (3.20)$$

3.3 Poisson Equation

Since the fluid has freely moving ions, it is natural to make sure that the model is not constrained to the case without spatial charge concentrations. This is done by including the Poisson equation which feeds back into the chemical potential and the electric body force, through the potential, ϕ . The equation,

$$0 = \partial_i \partial_i \phi + \frac{e}{\epsilon} \sum_k Z_k c_0 \exp(\tilde{c}_k) = \frac{k_B T}{e} \partial_i \partial_i \tilde{\phi} + \frac{e}{\epsilon} \sum_k Z_k c_0 \exp(\tilde{c}_k), \quad (3.21)$$

is composed of the Laplace operator on the potential, and the free charge concentration, here expressed in the normalized concentration variables \tilde{c}_k and after the last equality, also in the normalized potential, $\tilde{\phi}$, defined in equation (3.4). ϵ is the dielectric constant for the fluid, which in most cases will be water, for which $\epsilon = 7.1 \cdot 10^{-10} \text{ CV}^{-1} \text{ m}^{-1}$ at room temperature (25 °C).

Going from this into weak form, using the test functions $\hat{\phi}$, yields

$$0 = \int_{\Omega} \hat{\phi} \left(\partial_i \partial_i \tilde{\phi} + \alpha_{\epsilon} \sum_k Z_k \exp(\tilde{c}_k) \right) dV, \quad (3.22)$$

where a new variable, α_{ϵ} , has been introduced, which is defined by

$$\alpha_{\epsilon} = \frac{e^2 c_0}{\epsilon k_B T}, \quad [\alpha_{\epsilon}] = \text{m}^{-2}. \quad (3.23)$$

This variable is related to the Debye length, λ_D , as this is given by

$$\lambda_D = \sqrt{\frac{\epsilon k_B T}{2Z^2 e^2 c_0}} \quad (3.24)$$

where c_0 refers to the concentration in the bulk, and it is assumed that the two ion species in the fluid have the same valence. Returning to equation 3.22, the double derivative can be changed to a single derivative by moving terms to the boundary (integration by parts),

$$0 = \left[\hat{\phi} n_i \partial_i \tilde{\phi} \right]_{\partial\Omega} + \int_{\Omega} \left(-\partial_i \hat{\phi} \right) \partial_i \tilde{\phi} + \hat{\phi} \alpha_{\epsilon} \sum_k Z_k \exp(\tilde{c}_k) dV. \quad (3.25)$$

Leaving the volume equations, and going to the boundary, we can see from equation (3.25) that there is a contribution that only exists on the boundary. On top of this, we would like to add a surface charge, as there are chemical reactions between the fluid and the wall material. As a last constraint a potential drop across the channel has to be forced, since this is what is done when electrodes and a voltage supply is used on the physical system. In total this gives the following list of different boundaries:

All Uncharged Boundaries - Dashed Lines and Solid Yellow Lines In principle, part of the equation is moved to the boundary by integration by parts. This is a weak contribution given by

$$\left[\hat{\phi} n_i \partial_i \tilde{\phi} \right]_{\partial\Omega} \quad (3.26)$$

but as we know from classical electrodynamics, the derivative perpendicular to the wall must be zero, if there is zero wall charge,

$$n_i \partial_i \tilde{\phi} = 0 \Rightarrow \hat{\phi} n_i \partial_i \tilde{\phi} = 0. \quad (3.27)$$

To impose this, zero is substituted in where the derivative is. This gives the zero flux condition, which is the default boundary condition in COMSOL. Another way to do it is by being thorough and setting the weak contribution

$$\hat{\phi} \cdot 0 \quad (3.28)$$

on all uncharged boundaries. This is why the headline is not "All Boundaries" but rather something which is understood as "All Boundaries Except Charged Walls".

Charged Wall BC - Solid Blue On some or all of the walls, it is necessary to add a surface charge, as this is what is experimentally observed. For silica glass, which is the favoured experimental material and is thus the material considered throughout this thesis, the dangling Si bonds have created covalent bonds with OH^- groups. This structure can take part in an equilibrium reaction with water, where the H^+ ion is transferred to a water molecule, much like what is happening in the self-ionization of water,



There are other possible reactions (a rather long list), but the effect is the same, to create some surface charge or none. The impact of each of these reactions on the total surface charge, depends on the local pH. It is however a reasonable approximation, for pH about neutral, that only the stated reaction occurs and that the surface charge is the same everywhere. As we shall see in the analysis, a fixed pH is not always the case, and more work could be done to include this effect. This will not be further investigated here, but could be implemented in the numerical model as a surface equation or set of surface equations. For more information and references see Andersen [2, p.18] or [3, sec. 2.4]. In order to model the surface reactions in a simple way, a constant surface charge, σ_s , is introduced. To include it, just as in the case of zero surface charge, the derivative of the potential at the surface has to be set to a specific value. To prove the exact expression a Gauss pillbox can be made, and the closed integral carried out. However this is done in most textbooks on the subject of electromagnetism, and therefore only the result is stated and used. Choosing the normal vector in the same way as it is defined in COMSOL, positive out of the system, away from the water, it can be shown that

$$n_i \partial_i \phi = \frac{\sigma_s}{\epsilon} \Rightarrow n_i \partial_i \tilde{\phi} = \frac{\sigma_s e}{\epsilon k_B T}. \quad (3.30)$$

This expression for the derivative can now be substituted into the boundary contribution from equation (3.25), to force a specific value for the derivative. This gives

$$\left[\hat{\phi} n_i \partial_i \tilde{\phi} \right]_{\partial\Omega} = \left[\frac{\sigma_s e}{k_B T \epsilon} \hat{\phi} \right]_{\partial\Omega}, \quad (3.31)$$

which is the weak contribution necessary on all the charged boundaries.

Potential BC - Anything Brown On some or all of the reservoirs connected to the open boundaries, or at points and boundaries inside the system, electrodes with different potentials could be applied. In the latter case one would have to include chemical reaction terms to avoid an unphysical ion build up around the electrodes. For the open boundaries however, this problem is not relevant as the concentration is set, and the system is free to flow in and out of the system. In the model the potential on the electrode is a constraint (Dirichlet boundary condition) of the type

$$0 = \tilde{\phi} - \tilde{\phi}_{BC} \quad (3.32)$$

working to force a potential. However $\tilde{\phi}_{BC}$ could, and would most likely, be different on the different boundaries or points, depending on the purpose of the setup, and in some cases contradictory boundary conditions could give problems. This will be discussed in more detail in section 3.6.

3.4 Ion Migration

The procedure used to derive the continuity equation and the Navier-Stokes equation can be reused for ion migration. Once again see figure 3.2. We are observing some volume of

arbitrary shape Ω , and we are only looking at the ions of a specific type, k , inside this volume. The change in time of type k inside this volume can only come from either an ion current through the surface of the volume, or from chemical reactions at some point inside the volume, $R_k(x, y)$. Writing this mathematically gives

$$\partial_t \int_{\Omega} c_k \, dV = - \int_{\partial\Omega} n_i J_{ik} \, dA + \int_{\Omega} R_k \, dV \quad (3.33)$$

where the ion current, J_{ik} of species k in direction i is given by advection and a gradient in the chemical potential,

$$\begin{aligned} J_{ik} &= c_k v_i - \frac{D_k}{k_B T} c_k \partial_i \mu_k \\ &= c_k v_i - D_k \partial_i c_k - \frac{Z_k e D_k}{k_B T} c_k \partial_i \phi, \end{aligned} \quad (3.34a)$$

which by introducing the normalized ion current,

$$\tilde{J}_{ik} = \frac{J_{ik}}{c_0}, \quad (3.35)$$

can be rewritten entirely in the new set of variables as

$$\begin{aligned} \tilde{J}_{ik} &= \exp(\tilde{c}_k) v_i - D_k \exp(\tilde{c}_k) \partial_i \tilde{\mu}_k \\ &= \exp(\tilde{c}_k) v_i - D_k \exp(\tilde{c}_k) \partial_i \tilde{c}_k - Z_k D_k \exp(\tilde{c}_k) \partial_i \tilde{\phi}. \end{aligned} \quad (3.36a)$$

This expression is only valid for low concentrations, < 100 mM, as the conductance is not a constant for larger concentrations. This concentration limitation should always be checked in the numerical model. If the concentration is above 100 mM anywhere in the computational domain, the results cannot be quantitatively trusted, and depending on the specific concentration, also not qualitatively trusted.

Now returning to the ion conservation equation, equation (3.33), the time derivative disappears, as we are in steady state, and as before the Gauss theorem can be used to convert the surface integral to a volume integral,

$$0 = - \int_{\Omega} \partial_i J_{ik} \, dV + \int_{\Omega} R_k \, dV. \quad (3.37)$$

Since the volume was arbitrarily chosen, the equation must still hold true if the integrals are removed. Therefore we now have

$$0 = -\partial_i J_{ik} + R_k, \quad (3.38)$$

which is the equivalent of the incompressibility condition for the fluid with the addition of a source/drain term, R_k . This expression is generally applicable for ionic species in steady state. In the case of self ionization of water, and generally in any equilibrium reactions, the creation and annihilation of ions cannot be neglected. This however is a

special case and will be investigated in section 3.5. In most cases for salt, there will not be any chemical reactions happening in steady state, as the salt is completely dissolved. This corresponds to $R_k = 0$ everywhere, and we can see from the equation, that the ion current is divergence free. To transform the equation into the non dimensionalized weak form, it is multiplied with the test function, divided by c_0 and integrated,

$$0 = - \int_{\Omega} \hat{c}_k \partial_i \tilde{J}_{ik} dV. \quad (3.39)$$

Thereafter the divergence is moved to the boundary by integration by parts,

$$0 = - \left[\hat{c}_k n_i \tilde{J}_{ik} \right]_{\partial\Omega} + \int_{\Omega} (\partial_i \hat{c}_k) \tilde{J}_{ik} dV, \quad (3.40)$$

and we are left with the final equation. It should be noted that there should not be a summation over the index of k , as it here represents one of the k equations for the k ion species. Leaving the bulk equation and redirecting attention to the boundaries there are three types of boundary conditions:

Wall BC - Solid Lines It is a requirement that we have no ion current into or out of any walls. Mathematically this means

$$n_i \tilde{J}_{ik} = 0. \quad (3.41)$$

Inserting this in the boundary term from equation (3.40), we see that there should be a zero weak boundary contribution, or a no flux boundary condition,

$$- \left[\hat{c}_k n_i \tilde{J}_{ik} \right]_{\partial\Omega} \Rightarrow - [\hat{c}_k \cdot 0]_{\partial\Omega} \quad (3.42)$$

Inlet BC - Dashed Green At the inlet fluid flows into the system from some reservoir with concentration $c_k = c_{Bk}$, where c_{Bk} is the bulk concentration of a particular reservoir. Therefore the concentration must match that of the reservoir, which means a constraint of the type

$$\log \left(\frac{c_{Bk}}{c_0} \right) = \tilde{c}_k \quad (3.43)$$

But as for the potential, there might be contradictory boundary conditions, as the concentrations depend on the potential. But this will be addressed in section 3.6.

Outlet BC - Dashed Red At the outlet, the exact same situation as for the inlet is happening, with the exception that there might be different concentrations in the reservoir leading to different values of c_{Bk} .

3.5 Self-Ionization of Water

To add to the complexity of the model, also the self ionization of water is included, as water is constantly reacting with itself to form the hydronium and oxonium ions, as seen in



Here the brackets refer to the concentration, while K_{eq} is the equilibrium constant. If we restrict ourselves to low concentration of solutes, which is the case for almost all biological systems, and thereby most systems of interest, we can take the concentration of water to be constant, $[\text{H}_2\text{O}] = 55.5 \text{ M}$. With this, and again using the variable change from equation 3.1, we can rewrite the equation to

$$\begin{aligned} \exp(\tilde{c}_{\text{H}_3\text{O}^+}) \exp(\tilde{c}_{\text{OH}^-}) &= K_{\text{eq}} \frac{c_{\text{H}_2\text{O}}^2}{c_0^2} = K \\ \Leftrightarrow K \exp(-\tilde{c}_{\text{H}_3\text{O}^+}) &= \exp(\tilde{c}_{\text{OH}^-}) \end{aligned} \quad (3.45)$$

with the new unitless variable, $K = 10^{-8}$, for $c_0 = 1 \text{ mM} = 6.022 \times 10^{23} \text{ m}^{-3}$, being a system constant for a uniform constant temperature, $T = 25^\circ \text{ C}$. The reaction rate, is assumed to be fast enough, that the characteristic time is much lower than any other characteristic time scales of the system, so the water self-ionization process is always at equilibrium. The two new species are also ions, and thus they can be quantified by the same method that led to equation (3.38). Starting from this equation we instantly see that the reaction rate, R , is non-zero, as the ions are continually formed and annihilated in pairs wherever there is water present. From equation 3.44 it is evident that pairs are made with a ratio of one, so $R_{\text{H}_3\text{O}^+} = R_{\text{OH}^-}$. This gives the equations

$$\begin{aligned} \partial_i \left[-D_{\text{H}_3\text{O}^+} \partial_i (c_0 \exp(\tilde{c}_{\text{H}_3\text{O}^+})) + v_i c_0 \exp(\tilde{c}_{\text{H}_3\text{O}^+}) \right. \\ \left. -D_{\text{H}_3\text{O}^+} c_0 \exp(\hat{c}_{\text{H}_3\text{O}^+}) \partial_i \tilde{\phi} \right] - R_{\text{H}_3\text{O}^+} = 0 \end{aligned} \quad (3.46)$$

$$\begin{aligned} \partial_i \left[-D_{\text{OH}^-} \partial_i (c_0 \exp(\tilde{c}_{\text{OH}^-})) + v_i c_0 \exp(\tilde{c}_{\text{OH}^-}) \right. \\ \left. +D_{\text{OH}^-} c_0 \exp(\tilde{c}_{\text{OH}^-}) \partial_i \tilde{\phi} \right] - R_{\text{OH}^-} = 0 \end{aligned} \quad (3.47)$$

Where Z , the oxidation state, has been inserted for the different ions. All these equations can now be combined to form a single equation for the self ionization of water. By taking the difference between the two equations (3.46) and (3.47), and eliminating c_{OH^-} by use of equation (3.45) we arrive at

$$\partial_i \left[\tilde{J}_{i,\text{H}_3\text{O}^+} - \tilde{J}_{i,\text{OH}^-} \right] = 0 \quad (3.48)$$

$$\begin{aligned} \Rightarrow \partial_i \left[-D_{\text{H}_3\text{O}^+} \exp(\tilde{c}_{\text{H}_3\text{O}^+}) \partial_i \tilde{c}_{\text{H}_3\text{O}^+} + v_i \exp(\tilde{c}_{\text{H}_3\text{O}^+}) \right. \\ \left. -D_{\text{H}_3\text{O}^+} \exp(\hat{c}_{\text{H}_3\text{O}^+}) \partial_i \tilde{\phi} \right. \\ \left. -D_{\text{OH}^-} K \exp(-\tilde{c}_{\text{H}_3\text{O}^+}) \partial_i \tilde{c}_{\text{H}_3\text{O}^+} - v_i K \exp(-\tilde{c}_{\text{H}_3\text{O}^+}) \right. \\ \left. -D_{\text{OH}^-} K \exp(-\tilde{c}_{\text{H}_3\text{O}^+}) \partial_i \tilde{\phi} \right] = 0 \end{aligned} \quad (3.49)$$

which we can then rewrite into weak form, using the same methods of multiplying with the test function and integrating, as used in previous sections,

$$\left[\hat{c}_{\text{H}_3\text{O}^+} n_i \left(\tilde{J}_{i,\text{H}_3\text{O}^+} - \tilde{J}_{i,\text{OH}^-} \right) \right]_{\partial\Omega} - \int_{\Omega} \partial_i \hat{c}_{\text{H}_3\text{O}^+} \left(\tilde{J}_{i,\text{H}_3\text{O}^+} - \tilde{J}_{i,\text{OH}^-} \right) dV = 0 \quad (3.50)$$

It should be noted that it is assumed that any reactions in the area of interest does not impact the temperature. Again for very dilute ionic solvents, this is a valid approximation. For a more general description of pH with multiple solvents that can react, see Persat et al. [15]. This will not be further investigated here. The boundary conditions are then:

Open - Dashed Lines In the reservoirs pure water is stored, which means there is an equal number of H_3O^+ and OH^- . From this it is straightforward to calculate the redefined concentration at the boundaries by

$$\exp(\tilde{c}_{\text{H}_3\text{O}^+}) = \sqrt{K} \Rightarrow \tilde{c}_{\text{H}_3\text{O}^+} = \frac{1}{2} \log(K) \quad (3.51)$$

Wall BC - Solid Lines As argued previously, ions cannot migrate into the walls. Therefore the ion current perpendicular to a wall must be zero. This is the no flux condition for a single ion species, which means

$$n_i J_{i,\text{H}_3\text{O}^+} = 0 \quad n_i J_{i,\text{OH}^-} = 0, \quad (3.52)$$

which, when inserted in equation (3.49) means that the whole boundary term is zero, and therefore the full equation has to satisfy a no flux boundary condition.

3.6 1D Debye Layer and Conflicting Boundary Conditions

As hinted earlier, there might be boundary conditions that are contradictory. In particular, we would like to have surface charge on all walls in the model, but this could lead to problems. For instance if the surface charge boundary condition was imposed on the layers leading up to the open boundary conditions with a potential assigned to them (experimentally via electrodes), the two boundary conditions would be mutually exclusive, as seen in figure 3.3. The surface charge would force a non zero gradient of the potential, while the electrode boundary condition would force a constant potential. Therefore, to extent the surface charge layers all the way to the boundaries with electrodes, it is necessary to solve the potential in a 1D model, and use that as the constraint to define a 1D equilibrium potential to be used on the boundary for the 2D system. Unfortunately it is not as easy as that, as this would change the previously stated boundary conditions for the concentrations, \tilde{c}_k and the potential, ϕ . In principle it would also change the pressure, P , but luckily we redefined the pressure into \tilde{P} , which is designed to exactly avoid gradients perpendicular to the walls. The solution of this apparent dilemma is the focus of this section.

In order to find both the concentration and potential, we know that there is no advection along the boundary. With the assumption that the bulk has true reservoir conditions and that the problematic area is only near the walls, we can solve the Electro-Diffusion equation in 1D to find the Poisson-Boltzmann equation. With the zero point in the reservoir, the bulk far away from the walls, we can write the concentration as

$$c_k = c_B \exp\left(-\frac{Z_k e}{k_B T} \phi\right) = c_0 \exp(\tilde{c}_k) \quad (3.53)$$

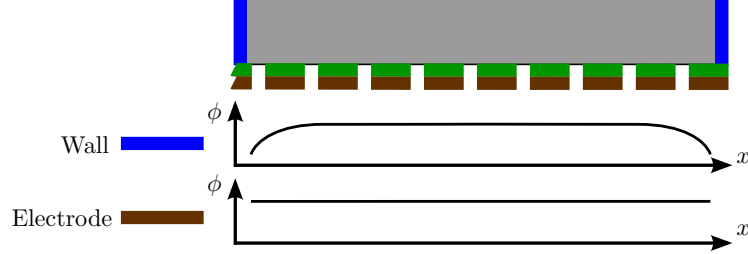


Figure 3.3: View of a vertical channel, with the top continuing to the rest of the structure and the bottom being an open boundary. Forcing a constant potential across the open boundary via the electrode (brown) would result in the derivative perpendicular to the charged wall to be zero. This violates the boundary condition for the charged wall (blue) that demands a non zero perpendicular derivative. Qualitative view of the two different potentials for the two boundary conditions can be seen below the channel for a cut lying on the open (dashed) boundary. Clearly these two demands are mutually exclusive, and something has to be done to circumvent the problem.

where c_{Bk} is the bulk concentration on the boundary of species k , and the only change in energy is from the electrical potential. Inserting this into the Poisson equation, and using the redefined potential, this yields the governing equation for the system,

$$\partial_x^2 \tilde{\phi}_{\text{eq}} = -\alpha_\epsilon \sum_k Z_k \frac{c_{Bk}}{c_0} \exp\left(-Z_k \tilde{\phi}_{\text{eq}}\right). \quad (3.54)$$

where ϕ_{eq} is the equilibrium potential. This equation is valid for any number of ionic species, including oxonium and hydronium, in case the pH of the system is under consideration. Before solving this equation, it should be noted that we can find the concentrations when the system is in equilibrium, by using equation (3.53). This expression can, in the redefined variables, be reduced to

$$\tilde{c}_k = \log\left(\frac{c_{Bk}}{c_0}\right) - Z_k \tilde{\phi}_{\text{eq}}, \quad (3.55)$$

which could be relevant for reservoirs containing multiple ion solutions or different pH values. A method using the chemical potential can be seen in [4, p.145-147]. Equation (3.54) can be transformed to the COMSOL version by multiplying with the test function, integrating and using integration by parts

$$0 = \left[\hat{\phi}_{\text{eq}} n_x \partial_x \tilde{\phi}_{\text{eq}} \right]_{\partial\Omega} - \int_{\Omega} \left(\partial_x \hat{\phi}_{\text{eq}} \partial_x \tilde{\phi}_{\text{eq}} - \hat{\phi}_{\text{eq}} \alpha_\epsilon \sum_k Z_k \frac{c_{Bk}}{c_0} \exp\left(-Z_k \tilde{\phi}_{\text{eq}}\right) \right) dV. \quad (3.56)$$

However, due to the surface charge on the boundary, the boundary term has to be substituted, as argued for the full Poisson equation, in section 3.3, with

$$\left[\hat{\phi}_{\text{eq}} n_x \partial_x \tilde{\phi}_{\text{eq}} \right]_{\partial\Omega} \Rightarrow \left[\hat{\phi}_{\text{eq}} \frac{\sigma_s e}{\epsilon k_B T} \right]_{\partial\Omega}. \quad (3.57)$$

As can be seen, this gives the same gradient as in equation (3.31), which means we now have physical boundaries without contradictory terms, given the Poisson-Boltzman equation is valid.

3.7 Copy-Paste Friendly COMSOL Model Expressions

This section is divided into two subsections, that each contain a complete set of equations and boundary conditions that can be used to directly create a self-contained COMSOL model. These expressions are based on the equations and boundary conditions derived throughout the previous sections in this chapter. The main idea is to create an easy way to access and use the equations in COMSOL. It should be noted that there is a slight change of variables, due to COMSOL not accepting special symbols. In each of the two subsections are tables for the 1D model, explanation of the variables used and finally the table containing the actual weak form expressions and boundary conditions. These models only handle a two species ionic solution, and assumes that both species have the concentration c_0 in the reservoirs. This could be changed by changing the 1D model and the way the boundary conditions for the reservoir in the 2D model is handled, see equations (3.54) and (3.55). An example can be seen in the tables in the water splitting section, as the oxonium ions does not have the reservoir concentration c_0 .

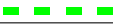
The linear extrusions `comp2.linext1(comp2.phieq)` are necessary to couple between the 1D model and the 2D model in order to use the solution of the 1D model in the 2D model. In this example only two were used, but in case of more than two reservoirs, more linear extrusions should be introduced and used, one for each reservoir.

3.7.1 Copy-Paste Friendly COMSOL Expressions Without Water Splitting

Node	Variable	Explanation or Value
Navier-Stokes	u	Variable for x component of velocity field
Navier-Stokes	v	Variable for y component of velocity field
Navier-Stokes	LM_Inlet_1	Auxillary boundary variable - Lagrange Multiplier
Navier-Stokes	LM_Inlet_2	Auxillary boundary variable - Lagrange Multiplier
Navier-Stokes	LM_Outlet_1	Auxillary boundary variable - Lagrange Multiplier
Navier-Stokes	LM_Outlet_2	Auxillary boundary variable - Lagrange Multiplier
Continuity	P	Variable for the pressure field
EMD Species 1	Lc1	Variable for the normalized concentration field of species 1
EMD Species 2	Lc2	Variable for the normalized concentration field of species 2
Poisson	phi	Variable for the electric potential field
1D Poisson	comp2.phieq	Variable for the electric potential field (phieq) in the 1D model (comp2)
Any Boundary	nx	x component of the normal vector to the boundary
Any boundary	ny	y component of the normal vector to the boundary
Global Definition	PInlet	Variable used to set pressure at inlet
Global Definition	POutlet	Variable used to set pressure at outlet
Global Definition	VInlet	Variable used to set electric potential at inlet
Global Definition	VOutlet	Variable used to set electric potential at outlet
Global Definition	alpha_rho	Renormalized variable, see equation (3.11b)
Global Definition	alpha_eta	Renormalized variable, see equation (3.11c)
Global Definition	alpha_eps	Renormalized variable, see equation (3.23)
Global Definition	Z1	Variable used to set charge of species 1
Global Definition	Z2	Variable used to set charge of species 2
Global Definition	D1	Variable used to set diffusivity of species 1
Global Definition	D2	Variable used to set diffusivity of species 2
Global Definition	sigma_surf	Variable used to set surface charge density
Global Definition	e	Electron charge
Global Definition	kb	Boltzmann constant
Global Definition	T	Absolute Temperature
Global Definition	eps_w	Dielectric constant of the fluid (water)

Where	COMSOL Type	Equation Name	COMSOL Expression
Bulk	Weak PDE	1D Poisson	$-\text{test}(\text{phieqx}) * \text{phieqx}$ $+\text{test}(\text{phieq}) * \alpha_eps * (Z1 * \exp(-Z1 * \text{phieq}) + Z2 * \exp(-Z2 * \text{phieq}))$
All	Weak Contribution	1D Poisson	$\text{test}(\text{phieq}) * \sigma_surf * e / \epsilon_w / kb / T$

Where	COMSOL Type	Equation Name	COMSOL Expression
Bulk	Weak PDE	Navier-Stokes - x	$-\text{test}(ux)*P+\alpha_{\text{eta}}*(2*\text{test}(ux)*ux+\text{test}(uy)*(vx+uy))$ $+\text{test}(u)*(exp(Lc1)*(Lc1x+Z1*phix)+exp(Lc2)*(Lc2x+Z2*phix))$ $+\alpha_{\text{rho}}*(u*ux+v*uy)$
Bulk	Weak PDE	Navier-Stokes - y	$-\text{test}(vy)*P+\alpha_{\text{eta}}*(2*\text{test}(vy)*vy+\text{test}(vx)*(uy+vx))$ $+\text{test}(v)*(exp(Lc1)*(Lc1y+Z1*phiy)+exp(Lc2)*(Lc2y+Z2*phiy))$ $+\alpha_{\text{rho}}*(u*vx+v*vy)$
————	Weak Contribution	Navier-Stokes	$nx*\text{test}(u)*(-\alpha_{\text{rho}}*u*u+(-P+2*\alpha_{\text{eta}}*ux))$ $+ny*\text{test}(u)*(-\alpha_{\text{rho}}*u*v+\alpha_{\text{eta}}*(uy+vx))$ $+nx*\text{test}(v)*(-\alpha_{\text{rho}}*v*u+\alpha_{\text{eta}}*(uy+vx))$ $+ny*\text{test}(v)*(-\alpha_{\text{rho}}*v*v+(-P+2*\alpha_{\text{eta}}*vy))$
————	Constraint	Navier-Stokes	u
————	Constraint	Navier-Stokes	v
■ ■ ■ ■	Constraint	Navier-Stokes	$\text{test}(u)*(LM_Inlet_1)+\text{test}(v)*(LM_Inlet_2)$ $+\text{test}(LM_Inlet_1)*(nx*(nx*ux+ny*vx)+ny*(nx*uy+ny*vy))$ $+\text{test}(LM_Inlet_2)*(nx*v-ny*u)$
■ ■ ■ ■	Auxillary Variable	Navier-Stokes	LM_Inlet_1
■ ■ ■ ■	Auxillary Variable	Navier-Stokes	LM_Inlet_2
■ ■ ■ ■	Constraint	Navier-Stokes	$\text{test}(u)*(LM_Outlet_1)+\text{test}(v)*(LM_Outlet_2)$ $+\text{test}(LM_Outlet_1)*(nx*(nx*ux+ny*vx)$ $+ny*(nx*uy+ny*vy))+\text{test}(LM_Outlet_2)*(nx*v-ny*u)$
■ ■ ■ ■	Auxillary Variable	Navier-Stokes	LM_Outlet_1
■ ■ ■ ■	Auxillary Variable	Navier-Stokes	LM_Outlet_2
Bulk	Weak PDE	Continuity	$\text{test}(P)*(ux+vy)$
■ ■ ■ ■	Constraint	Continuity	P-PInlet
■ ■ ■ ■	Constraint	Continuity	P-POutlet

Where	COMSOL Type	Equation Name	COMSOL Expression
Bulk	Weak PDE	EMD Species 1	$\text{test}(Lc1x) * (\exp(Lc1) * u - D1 * \exp(Lc1) * (Lc1x + Z1 * \text{phix}))$ $+ \text{test}(Lc1y) * (\exp(Lc1) * v - D1 * \exp(Lc1) * (Lc1y + Z1 * \text{phiy}))$
	Weak Contribution	EMD Species 1	$\text{test}(Lc1) * (nx * (\exp(Lc1) * u - D1 * \exp(Lc1) * (Lc1x + Z1 * \text{phix}))$ $+ ny * (\exp(Lc1) * v - D1 * \exp(Lc1) * (Lc1y + Z1 * \text{phiy})))$
	Weak Contribution	EMD Species 1	$\text{test}(Lc1) * 0$
	Constraint	EMD Species 1	$Lc1 + Z1 * \text{comp2.linext1}(\text{comp2.phieq})$
	Constraint	EMD Species 1	$Lc1 + Z1 * \text{comp2.linext2}(\text{comp2.phieq})$
Bulk	Weak PDE	EMD Species 2	$\text{test}(Lc2x) * (\exp(Lc2) * u - D2 * \exp(Lc2) * (Lc2x + Z2 * \text{phix}))$ $+ \text{test}(Lc2y) * (\exp(Lc2) * v - D2 * \exp(Lc2) * (Lc2y + Z2 * \text{phiy}))$
	Weak Contribution	EMD Species 2	$\text{test}(Lc2) * (nx * (\exp(Lc2) * u - D2 * \exp(Lc2) * (Lc2x + Z2 * \text{phix}))$ $+ ny * (\exp(Lc2) * v - D2 * \exp(Lc2) * (Lc2y + Z2 * \text{phiy})))$
	Weak Contribution	EMD Species 2	$\text{test}(Lc2) * 0$
	Constraint	EMD Species 2	$Lc2 + Z2 * \text{comp2.linext1}(\text{comp2.phieq})$
	Constraint	EMD Species 2	$Lc2 + Z2 * \text{comp2.linext2}(\text{comp2.phieq})$
Bulk	Weak PDE	Poisson	$\alpha_eps * \text{test}(\text{phi}) * (Z1 * \exp(Lc1) + Z2 * \exp(Lc2))$ $- \text{test}(\text{phix}) * \text{phix} - \text{test}(\text{phiy}) * \text{phiy}$
	Weak Contribution	Poisson	$\sigma_surf / \epsilon_w * e / kb / T * \text{test}(\text{phi})$
	Weak Contribution	Poisson	$\text{test}(\text{phi}) * 0$
Along 	Constraint	Poisson	$\text{phi} - V_{\text{Inlet}} - \text{comp2.linext1}(\text{comp2.phieq})$
Along 	Constraint	Poisson	$\text{phi} - V_{\text{Outlet}} - \text{comp2.linext2}(\text{comp2.phieq})$

3.7.2 Copy-Paste Friendly COMSOL Expressions With Water Splitting

Node	Variable	Explanation or Value
Navier-Stokes	u	Variable for x component of velocity field
Navier-Stokes	v	Variable for y component of velocity field
Navier-Stokes	LM_Inlet_1	Auxillary boundary variable - Lagrange Multiplier
Navier-Stokes	LM_Inlet_2	Auxillary boundary variable - Lagrange Multiplier
Navier-Stokes	LM_Outlet_1	Auxillary boundary variable - Lagrange Multiplier
Navier-Stokes	LM_Outlet_2	Auxillary boundary variable - Lagrange Multiplier
Continuity	P	Variable for the pressure field
EMD Species 1	Lc1	Variable for the normalized concentration field of species 1
EMD Species 2	Lc2	Variable for the normalized concentration field of species 2
EMD Water	LcH	Variable for the normalized concentration field for hydronium
Poisson	phi	Variable for the electric potential field
1D Poisson	comp2.phieq	Variable for the electric potential field (phieq) in the 1D model (comp2)
Any Boundary	nx	x component of the normal vector to the boundary
Any boundary	ny	y component of the normal vector to the boundary
Global Definition	PInlet	Variable used to set pressure at inlet
Global Definition	POutlet	Variable used to set pressure at outlet
Global Definition	VInlet	Variable used to set electric potential at inlet
Global Definition	VOutlet	Variable used to set electric potential at outlet
Global Definition	alpha_rho	Renormalized variable, see equation (3.11b)
Global Definition	alpha_eta	Renormalized variable, see equation (3.11c)
Global Definition	alpha_eps	Renormalized variable, see equation (3.23)

Node	Variable	Explanation or Value
Global Definition	Z1	Variable used to set charge of species 1
Global Definition	Z2	Variable used to set charge of species 2
Global Definition	D1	Variable used to set diffusivity of species 1
Global Definition	D2	Variable used to set diffusivity of species 2
Global Definition	D_OH	Variable used to set diffusivity of OH ⁻
Global Definition	D_H	Variable used to set diffusivity of H ₃ O ⁺
Global Definition	sigma_surf	Variable used to set surface charge density
Global Definition	e	Electron charge
Global Definition	kb	Boltzmann constant
Global Definition	T	Absolute Temperature
Global Definition	eps_w	Dielectric constant of the fluid (water)
Global Definition	K	Chemical equilibrium constant for self-ionization of water
Global Definition	cH_Bulk	Bulk reservoir H ₃ O ⁺ concentration

Where	COMSOL Type	Equation Name	COMSOL Expression
Bulk	Weak PDE	1D Poisson	-test(phieqx)*phieqx +test(phieq)*alpha_eps*(Z1*exp(-Z1*phieq)+Z2*exp(-Z2*phieq)) +cH_Bulk/c0*exp(-phieq)-K^2/cH_Bulk*c0*exp(phieq)
All	Weak Contribution	1D Poisson	test(phieq)*sigma_surf*e/eps_w/kb/T

Where	COMSOL Type	Equation Name	COMSOL Expression
Bulk	Weak PDE	Navier-Stokes - x	$-\text{test}(u_x) * P + \alpha_{\text{eta}} * (2 * \text{test}(u_x) * u_x + \text{test}(u_y) * (v_x + u_y))$ $+\text{test}(u) * (\exp(Lc1) * (Lc1x + Z1 * \text{phi}_x) + \exp(Lc2) * (Lc2x + Z2 * \text{phi}_x))$ $+\exp(LcHp) * (LcHp_x + \text{phi}_x) + K * \exp(-LcHp) * (-LcHp_x - \text{phi}_x)$ $+\alpha_{\text{rho}} * (u * u_x + v * u_y)$
Bulk	Weak PDE	Navier-Stokes - y	$-\text{test}(v_y) * P + \alpha_{\text{eta}} * (2 * \text{test}(v_y) * v_y + \text{test}(v_x) * (u_y + v_x))$ $+\text{test}(v) * (\exp(Lc1) * (Lc1y + Z1 * \text{phi}_y) + \exp(Lc2) * (Lc2y + Z2 * \text{phi}_y))$ $+\exp(LcHp) * (LcHp_y + \text{phi}_y) + K * \exp(-LcHp) * (-LcHp_y - \text{phi}_y)$ $+\alpha_{\text{rho}} * (u * v_x + v * v_y)$
————	Weak Contribution	Navier-Stokes	$n_x * \text{test}(u) * (-\alpha_{\text{rho}} * u * u + (-P + 2 * \alpha_{\text{eta}} * u_x))$ $+n_y * \text{test}(u) * (-\alpha_{\text{rho}} * u * v + \alpha_{\text{eta}} * (u_y + v_x))$ $+n_x * \text{test}(v) * (-\alpha_{\text{rho}} * v * u + \alpha_{\text{eta}} * (u_y + v_x))$ $+n_y * \text{test}(v) * (-\alpha_{\text{rho}} * v * v + (-P + 2 * \alpha_{\text{eta}} * v_y))$
————	Constraint	Navier-Stokes	u
————	Constraint	Navier-Stokes	v
■ ■ ■ ■	Constraint	Navier-Stokes	$\text{test}(u) * (LM_Inlet_1) + \text{test}(v) * (LM_Inlet_2)$ $+\text{test}(LM_Inlet_1) * (n_x * (n_x * u_x + n_y * v_x) + n_y * (n_x * u_y + n_y * v_y))$ $+\text{test}(LM_Inlet_2) * (n_x * v - n_y * u)$
■ ■ ■ ■	Auxillary Variable	Navier-Stokes	LM_Inlet_1
■ ■ ■ ■	Auxillary Variable	Navier-Stokes	LM_Inlet_2
■ ■ ■ ■	Constraint	Navier-Stokes	$\text{test}(u) * (LM_Outlet_1) + \text{test}(v) * (LM_Outlet_2)$ $+\text{test}(LM_Outlet_1) * (n_x * (n_x * u_x + n_y * v_x)$ $+n_y * (n_x * u_y + n_y * v_y)) + \text{test}(LM_Outlet_2) * (n_x * v - n_y * u)$
■ ■ ■ ■	Auxillary Variable	Navier-Stokes	LM_Outlet_1
■ ■ ■ ■	Auxillary Variable	Navier-Stokes	LM_Outlet_2
Bulk	Weak PDE	Continuity	$\text{test}(P) * (u_x + v_y)$
■ ■ ■ ■	Constraint	Continuity	P-PInlet
■ ■ ■ ■	Constraint	Continuity	P-POutlet

Where	COMSOL Type	Equation Name	COMSOL Expression
Bulk	Weak PDE	EMD Species 1	$\text{test}(Lc1x) * (\exp(Lc1) * u - D1 * \exp(Lc1) * (Lc1x + Z1 * \text{phix}))$ $+ \text{test}(Lc1y) * (\exp(Lc1) * v - D1 * \exp(Lc1) * (Lc1y + Z1 * \text{phiy}))$
■ ■ ■ ■	Weak Contribution	EMD Species 1	$\text{test}(Lc1) * (nx * (\exp(Lc1) * u - D1 * \exp(Lc1) * (Lc1x + Z1 * \text{phix}))$ $+ ny * (\exp(Lc1) * v - D1 * \exp(Lc1) * (Lc1y + Z1 * \text{phiy})))$
————	Weak Contribution	EMD Species 1	$\text{test}(Lc1) * 0$
■ ■ ■ ■	Constraint	EMD Species 1	$Lc1 + Z1 * \text{comp2.linext1}(\text{comp2.phieq})$
■ ■ ■ ■	Constraint	EMD Species 1	$Lc1 + Z1 * \text{comp2.linext2}(\text{comp2.phieq})$
Bulk	Weak PDE	EMD Species 2	$\text{test}(Lc2x) * (\exp(Lc2) * u - D2 * \exp(Lc2) * (Lc2x + Z2 * \text{phix}))$ $+ \text{test}(Lc2y) * (\exp(Lc2) * v - D2 * \exp(Lc2) * (Lc2y + Z2 * \text{phiy}))$
■ ■ ■ ■	Weak Contribution	EMD Species 2	$\text{test}(Lc2) * (nx * (\exp(Lc2) * u - D2 * \exp(Lc2) * (Lc2x + Z2 * \text{phix}))$ $+ ny * (\exp(Lc2) * v - D2 * \exp(Lc2) * (Lc2y + Z2 * \text{phiy})))$
————	Weak Contribution	EMD Species 2	$\text{test}(Lc2) * 0$
■ ■ ■ ■	Constraint	EMD Species 2	$Lc2 + Z2 * \text{comp2.linext1}(\text{comp2.phieq})$
■ ■ ■ ■	Constraint	EMD Species 2	$Lc2 + Z2 * \text{comp2.linext2}(\text{comp2.phieq})$

Where	COMSOL Type	Equation Name	COMSOL Expression
Bulk	Weak PDE	Poisson	$\alpha_{\text{eps}} \cdot \text{test}(\phi) \cdot (Z_1 \cdot \exp(Lc_1) + Z_2 \cdot \exp(Lc_2) + \exp(Lc_{\text{Hp}}) - K \cdot \exp(-Lc_{\text{Hp}})) - \text{test}(\phi_{\text{ix}}) \cdot \phi_{\text{ix}} - \text{test}(\phi_{\text{iy}}) \cdot \phi_{\text{iy}}$
	Weak Contribution	Poisson	$\sigma_{\text{surf}} / \epsilon_{\text{ps_w}} \cdot e / k_{\text{b}} / T \cdot \text{test}(\phi)$
	Weak Contribution	Poisson	$\text{test}(\phi) \cdot 0$
 Along	Constraint	Poisson	$\phi - V_{\text{Inlet-comp2.linext1}}(\text{comp2.phieq})$
 Along	Constraint	Poisson	$\phi - V_{\text{Outlet-comp2.linext2}}(\text{comp2.phieq})$
Bulk	Weak PDE	EMD Water	$-\text{test}(Lc_{\text{Hpx}}) \cdot (u \cdot \exp(Lc_{\text{Hp}}) - D_{\text{Hp}} \cdot \exp(Lc_{\text{Hp}}) \cdot (Lc_{\text{Hpx}} + \phi_{\text{ix}}) - u \cdot K \cdot \exp(-Lc_{\text{Hp}}) - D_{\text{OH}} \cdot K \cdot \exp(-Lc_{\text{Hp}}) \cdot (Lc_{\text{Hpx}} + \phi_{\text{ix}})) - \text{test}(Lc_{\text{Hpy}}) \cdot (v \cdot \exp(Lc_{\text{Hp}}) - D_{\text{Hp}} \cdot \exp(Lc_{\text{Hp}}) \cdot (Lc_{\text{Hpy}} + \phi_{\text{iy}}) - v \cdot K \cdot \exp(-Lc_{\text{Hp}}) - D_{\text{OH}} \cdot K \cdot \exp(-Lc_{\text{Hp}}) \cdot (Lc_{\text{Hpy}} + \phi_{\text{iy}}))$
	Weak Contribution	EMD Water	$\text{test}(Lc_{\text{Hp}}) \cdot 0$
	Constraint	EMD Water	$Lc_{\text{Hp}} + \text{comp2.linext1}(\text{comp2.phieq}) - \log(c_{\text{H_Bulk}}/c_0)$
	Constraint	EMD Water	$Lc_{\text{Hp}} + \text{comp2.linext2}(\text{comp2.phieq}) - \log(c_{\text{H_Bulk}}/c_0)$

Chapter 4

Numerical Results and Comparison to Existing Work

The purpose of this chapter, is to convince the reader, that the numerical implementation and subsequent calculations are done correctly but also to illuminate which physics are important, and their effects, by slowly extending the numerical model and turning effects on and off. The first part is done through mesh convergence tests and by comparing the numerical results to analytically solvable cases and previous work done in the field. The second part by analysis of the results. This analysis also reveals important properties of the ion selective nano channel. The mesh analysis will be used to pick appropriate mesh parameters for the full numerical model. This is to ensure an optimal mesh for the full model, which might otherwise have too many degrees of freedom to be fully solved in a timely manner with the computational resources at hand.

The structure of this chapter follows the outline shown in the introduction in figure 1.1. Each subsequent model is based on the previous models in different ways. To elaborate, the 1D model for the potential in step 1 is used to impose correct reservoir boundary conditions on concentrations and the potential in all the 2D models.

The first 2D model in step 2 is used as a test case to ensure that the numerics are correctly implemented, as there are (semi) analytical solutions to compare with. Also the needed mesh parameters to properly resolve the Debye screening layer are found through a mesh convergence test.

In step 3 only the geometry and mesh are different to step 2. But the different geometry somewhat matches the models developed by Dydek et al., [5], Yossifon et al., [18], and Nielsen and Bruus, [11]. These models are with and without advection for the ideal ion selective membrane case. Therefore the model starts out without fluid flow for optimal comparison, while the narrow part of the geometry is varied, from wide to thin, as to mimic an ideal ion selective membrane. After this the advection is turned on, and the effects of advection are studied and compared to the model by Nielsen and Bruus, [11].

In step 4 the geometry is unchanged from step 3, but water splitting is added. The paper by Andersen et al. [1] deals with a 1D model which takes into account water splitting but ignores advection, and can be used for comparison. Therefore both a model with and without advection are investigated numerically.

In the first three steps, the equations and variables described in section 3.7.1 are used. For step 4 and onwards the equations in section 3.7.2 are used. With all these steps, the reader should be convinced that the built model is capable of handling the full experimentally feasible system which was one of the main goals of the thesis.

4.1 Step 1: 1D Poisson-Boltzmann model for Debye Layers

The first numerical implementation to be investigated is the 1D system, the Poisson-Boltzmann equation with appropriate boundary conditions. The analytical expression to compare to is the Gouy-Chapman expression derived for an infinite half space next to a charged boundary. This is strictly speaking not the case we are in, but for a wall to wall distance of $5 \mu\text{m}$ the walls are far enough apart, compared to the Debye length, that it is a good approximation. The expression is

$$\tilde{\phi} = 4 \operatorname{atanh} \left[\tanh \left(\frac{\zeta}{4} \right) \exp \left(-\frac{x}{\lambda_D} \right) \right] \quad (4.1)$$

$$\zeta = -2 \operatorname{asinh} \left(-\frac{\sigma_s}{4\epsilon c_0 \lambda_D} \right) \quad (4.2)$$

where ζ is the wall potential. The numerical solution and comparison to the analytical expression can be seen in figure 4.1, close to the wall. As expected they perfectly match. In the same figure, the convergence plot for the mesh can be seen. The mesh was constructed with two parameters, the size of the first layer at the boundary which was 0.1 nm and the exponential growth factor in the distance between subsequent points, G . For values smaller than $G = 1.8$ it is well converged. But the error for $G = 2$ is low enough that this value is used in the remaining thesis.

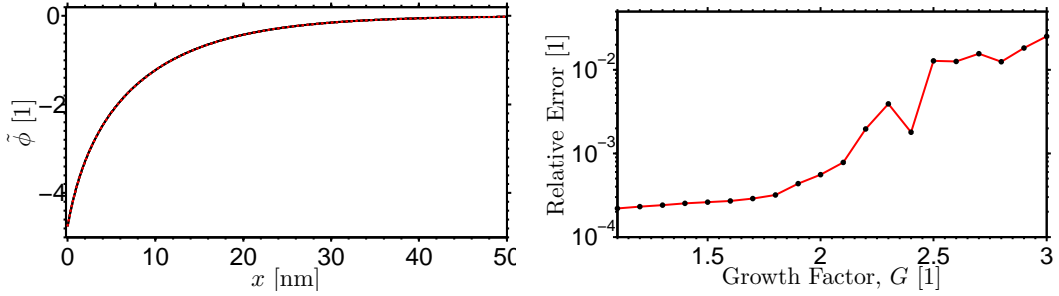


Figure 4.1: The left side shows the comparison between the potential, $\tilde{\phi}$ close to the wall. Black is the approximate analytical Gouy-Chapman expression while the dashed red is the numerical solution. On the right is seen the convergence analysis of the growth factor, where the black dots represent the data points. The first layer was always 0.1 nm thick for the different growth factors.

4.2 Step 2: Two Species Ion Solution in Infinite Parallel Plate Channel

Following the outline presented in the beginning of the chapter, it is now time to leave the analysis of the 1D model, and only use the results as the reservoir boundary condition for the 2D model presented in this section.

The system investigated in this section is the system seen in figure 4.2, the infinite parallel plate problem. The reason for analysing this specific problem is twofold. First we wish to make sure that our numerical model, developed in chapter 3 and described in section 3.7.1, is correctly implemented. This can be tested as the infinite parallel plate problem has analytical solutions with the precise physics we are implementing numerically. See for instance [4, p.157-165]. Secondly, we want to know how finely we need to resolve the Debye layers in the numerical model. Since the Debye layer physics does not change for different geometries, but only for the fluid properties, the resolution found in the analysis done in this chapter can be used directly in the subsequent steps.

Returning to figure 4.2, we see that there are surface reactions on the walls (solid blue lines), that give rise to a surface charge, as described in section 3.3. Also visible is a potential and pressure drop from one end of the parallel plate channel (dashed green/brown line) to the other end (dashed red/brown line). Now we wish to solve this analytically. With and without an applied potential drop, the system finds an equilibrium in the transverse direction as described in the previous section by moving charges to and from the wall in order to screen it. The wall charges imposes a boundary condition on the potential, resulting in a fixed derivative normal to the wall. This, along with the translational symmetry of the channel, gives us the idea to divide the potential into a transverse equilibrium

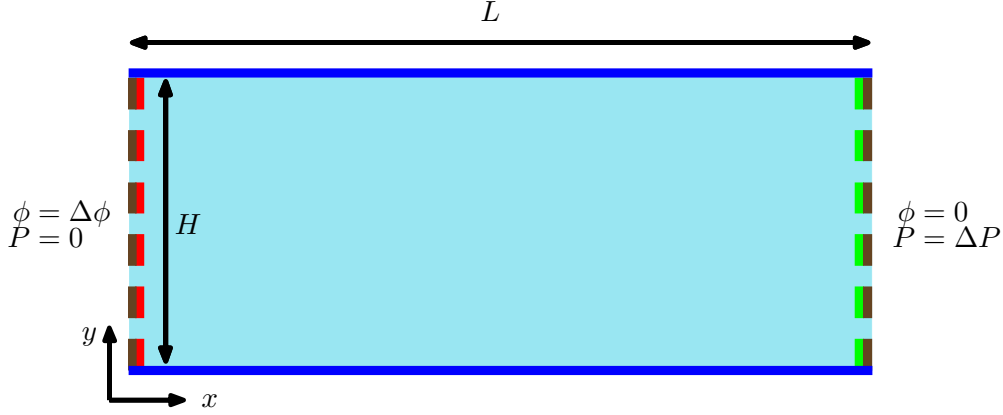


Figure 4.2: Sketch of the 2D infinite parallel plate channel with color coded imposed boundary conditions. Full blue lines are walls with a surface charge, $\sigma_s = -0.02 \text{ Cm}^{-2}$ (water on glass), while the dashed lines are open boundaries. There is a pressure drop (ΔP) from right to left, giving a flow from green to red. Furthermore there is a potential drop ($\Delta\phi$) from left to right, giving an flow from left to right.

potential and a parallel potential along the channel,

$$\phi(x, y) = \phi_{eq}(y) + \phi_{ext}(x) \quad (4.3)$$

The transverse equilibrium part has to satisfy the same boundary conditions as in the previous section (same surface charge), and therefore gives the same solution. This applies to both the transverse potential and by extension also the charge concentration ρ_{el} . Using the symmetry of the channel we can write up the Navier-Stokes equation for the system in steady state,

$$0 = -\partial_x P + \eta \partial_y^2 u - \rho_{el} \partial_x \phi_{ext} \quad (4.4)$$

With the no slip boundary condition for the velocity field and $\phi_{eq} = \zeta$ applied on the walls the solution to this equation is obtained, as a linear combination of a pressure driven (Poiseuille) flow and an electrically driven electro-osmotic flow. The solution is

$$u_{eo}(y) + u_P(y) = (\phi_{eq}(y) - \zeta) \frac{\epsilon}{\eta} \frac{\Delta\phi}{L} - \left(\frac{H^2}{2^2} - y^2 \right) \frac{1}{2\eta} \frac{\Delta P}{L} \quad (4.5)$$

where ζ is the potential on the wall. If we were in the Debye-Hückel limit, where the potential on the walls, ζ , is much smaller than the thermal voltage, $V_T = \frac{k_B T}{e}$, we could find an analytical solution. Instead we have to either use the Gouy-Chapman solution by approximating walls to be infinitely far apart, or to solve the equilibrium potential numerically. Since we already did just that, for the 1D case, and we can see that we are not in the Debye-Hückel limit ($\zeta \approx 4.8V_T$), it is convenient to use the 1D numerical solution for ϕ_{eq} directly and compare the semi analytical velocity field to the one obtained with the full 2D model. This comparison is done in figure 4.4. However, before going into a quantitative comparison between 2D numerical model and the analytical expression, let

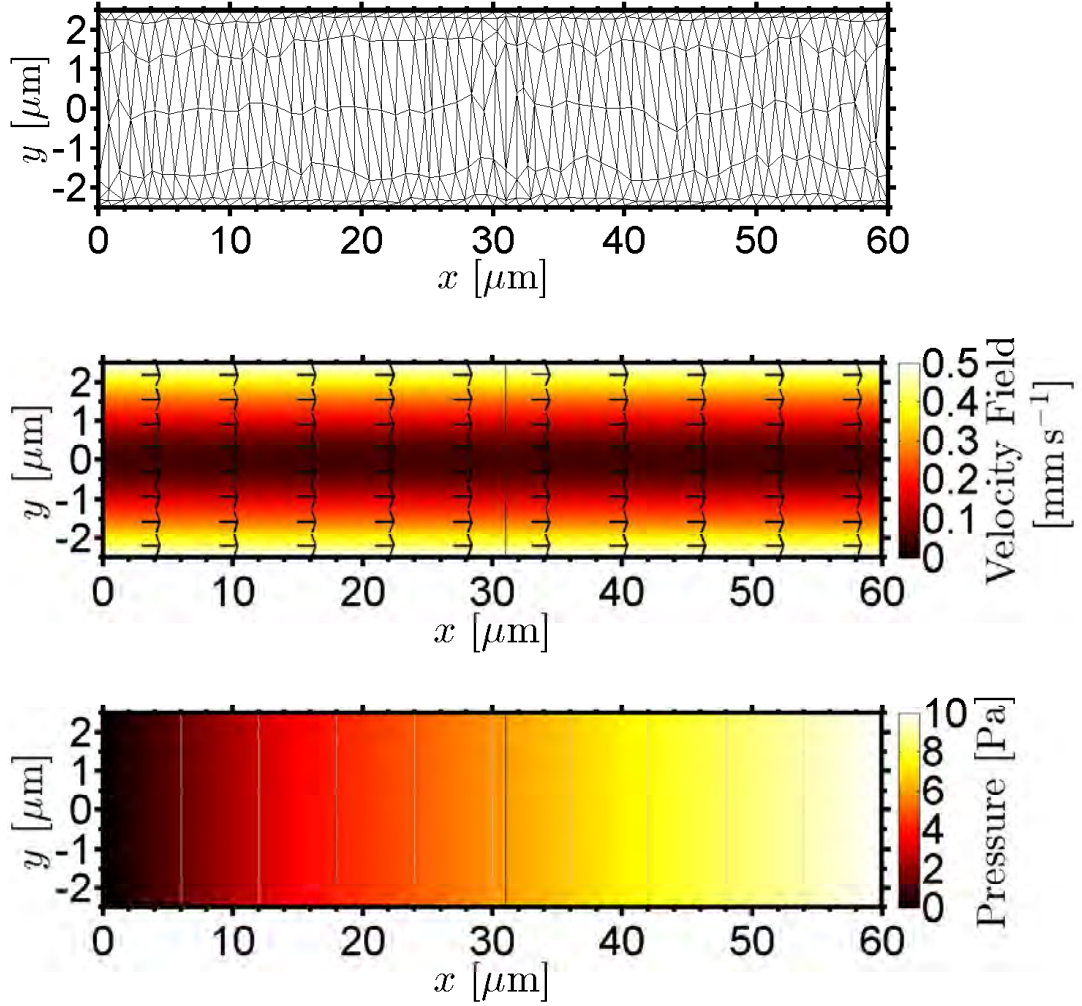


Figure 4.3: Figures showing different variables for a 2D model using equations from the tables in section 3.7.1 and boundary conditions as seen in figure 3.1. The parameters used were: $\Delta P = 10 \text{ Pa}$, $\Delta\phi = 15V_T$, $L = 60 \mu\text{m}$, $H = 5 \mu\text{m}$. Top: Model mesh with 10 boundary layers and a total boundary layer thickness of 50 nm. Middle: Velocity field at $\Delta\tilde{\phi} = 15$. Mesh as seen in top figure. The arrows indicate the direction. Bottom: Pressure in channel corresponding to the velocity profile. The grey vertical lines are the contour lines for each 1 Pa change in pressure. As expected they are near perfectly parallel to the y-axis.

us take a qualitative look at the results from the 2D numerical model.

In figure 4.3 the mesh used and the resulting velocity field and pressure are shown. If we take a look at the mesh first, we see that it consists of a triangular bulk part and, barely visible here, a rectangular boundary part close to the walls (top and bottom sides). The

bulk mesh has a maximum size parameter of $1 \mu\text{m}$ for the triangle sides and it is growing in size out from the walls (here top and bottom). This is due to connecting with the smaller boundary layer mesh, which is necessary to resolve the electrical Debye layer close to the walls. Since it is the net charge in the Debye layer that generates the electrically driven part of the fluid velocity field, it is necessary to resolve it finely. The mesh convergence analysis of the boundary layer is postponed to the end of this section. In principle a mesh convergence test should be performed on the bulk mesh, but since our only interest in this problem is for comparison to the semi analytical solutions, and the fluid flow is expected to be translationally invariant in the x -direction, there is not much point in wasting space showing it. Instead this mesh analysis is postponed to the next section where there is a more interesting and challenging fluid velocity field. Also we shall see that the errors from the bulk mesh are small compared to those from the Debye layer.

Leaving the mesh for now, we go to the fluid velocity field and the matching pressure field in figure 4.3. We see from the fluid velocity field the expected qualitative velocity profile with a large electrically driven flow close to the walls, and a pressure driven decrease close to the center. Also the translational symmetry is apparent along the channel. For the pressure we see a monotonous decrease through the channel. From the contour lines we see that there is no pressure changes across the channel. The contour lines are straight lines. This is to be expected, since we changed the pressure to include the gradient of the concentration to get the osmotic pressure explicitly written in Navier-Stokes equation. Also there are no artificial artefacts from the mesh, which would result in jagged lines.

In the top part of figure 4.4 the results from the numerical model are compared to the analytical expression in equation (4.5). This is done for the x -component of the velocity field along a line parallel to the y axis, at $x = 30 \mu\text{m}$ (the center of the channel). Each blue line is from the expression, while the corresponding red is the numerical model. The different pairs are for an increasing external potential difference. For the case with zero external potential difference, the flow in the channel is solely driven by a pressure difference, and the flow is the known Poiseuille flow with a parabolic flow profile across the channel. With the external potential difference increasing, the drag force experienced by the fluid in the boundary layers increase and starts to drag the fluid in the opposite direction than the pressure drop. Still there is a perfect correspondence between the analytical expression and the numerical model. As a side note, it should be mentioned, that if the Debye-Hückel approximation was used to obtain a purely analytical expression for ϕ_{eq} , and this was plotted ontop of the current graph, there would be no discernible difference. The only minute difference is the exact position of the local maximum of the x -component of the velocity field and the value in this point. The overall profile is the same. This observation could be important in developing an analytical model. The conclusion is that the numerical implementation of the physics is done correctly for the the velocity field, the pressure, the concentrations and the potential.

To end this section, lets look at the Debye layer mesh analysis. This is shown in the bottom

part of figure 4.4. In the inset, the mesh is seen again, but this time zoomed in on the lower left corner, to show the boundary layers. The parameters, in COMSOL, to control the boundary layer mesh is the number of layers, the growth from one layer to another and the thickness of the first layer. Since the characteristic length scale for the exponentially decaying physics at the boundary is the Debye length, a more practical set of parameters is the number of boundary layers, the growth factor and the total thickness. Going from one set of parameters to the other is a short algebraic exercise, which is omitted here. The growth factor has been discussed in the previous section. The total thickness T_D is something that should be many times larger than the characteristic length, but due to the exponential decay, after a certain point the error in truncating is negligible. This leaves the number of boundary layers as a characteristic parameter for improving the mesh. In this way the mesh improvement is spread evenly in an area with thickness T_D away from the boundaries which are walls.

The relative error is here calculated as the difference in velocity parallel to the channel between some mesh and the best mesh, integrated and divided by the integrated best mesh velocity. This is all done along the $x = 30 \mu\text{m}$ line, as the difference between this method and the full 2D integral is only a scaling factor due to the translational symmetry.

The red lines seen in the bottom part of figure 4.4 is a baseline test, where the external potential difference is zero. This means that we are only improving the mesh for the Poiseuille flow. Since the mesh improvements are very local around points without fluid movements (no slip condition at the walls), we do not expect to see big improvements, if any at all. The error here should also be considered our error floor, or noise level, for errors from the electrokinetically driven fluid flow, since it is unchanged throughout the investigation. As expected the red lines are below the other lines, so the errors in the electrokinetically driven flow are dominating when the boundary layer is only a few layers thick. Furthermore, the line for a total thickness of 100 nm has a slight slope compared to the line for a total thickness of 50 nm, which is explained by the improvements in the mesh reaching further out into the bulk where the pressure driven flow is larger, and mesh improvements therefore have a larger effect.

When there is an electrokinetically driven flow with the pressure driven flow, the relative errors are decreasing almost perfectly exponentially (straight line in the semi logarithmic plot) with number of boundary layers. This means the solution is converged, and the number of boundary layers is just a question of the wanted precision. For instance four layers could be used, if a relative error of 0.1 % can be tolerated. The slope is independent of the total thickness, but as expected the full lines all lie below the dashed lines since the same number of boundary layers are used to describe a smaller area, which gives improvements in the resolution. This also goes to show that the error in truncating the exponentially decaying concentration field is negligible compared to resolving it correctly close to the wall. At more than six layers, the total error level is down to the noise level generated by the pure Poiseuille flow. In the following the mesh parameters used for

the boundary layers are: A total thickness of $T_D = 50$ nm with seven boundary layers and a growth factor of $G = 2$. The first layer of the triangular mesh is connected to the boundary mesh, and therefore has approximately the same size parameter. However it quickly grows to the maximum value specified earlier, $1 \mu\text{m}$, in the bulk. So far the resolution perpendicular to the wall has been discussed, but there is also the resolution along the wall. This is solely determined by the mesh size in the bulk, and the discussion is therefore more suited for the section where the bulk mesh is investigated. Also it would not make sense to discuss it here, as there is translational symmetry.

To sum up the section, it has been shown that the numerical model seen in section 3.7.1, is correctly implemented. Furthermore the mesh parameters for the boundary layers are: A total thickness five times larger than the Debye length ($T_D = 50$ nm) with a total number of layers of 7 and growth factor $G = 2$. This gives a relative error below 10^{-4} .

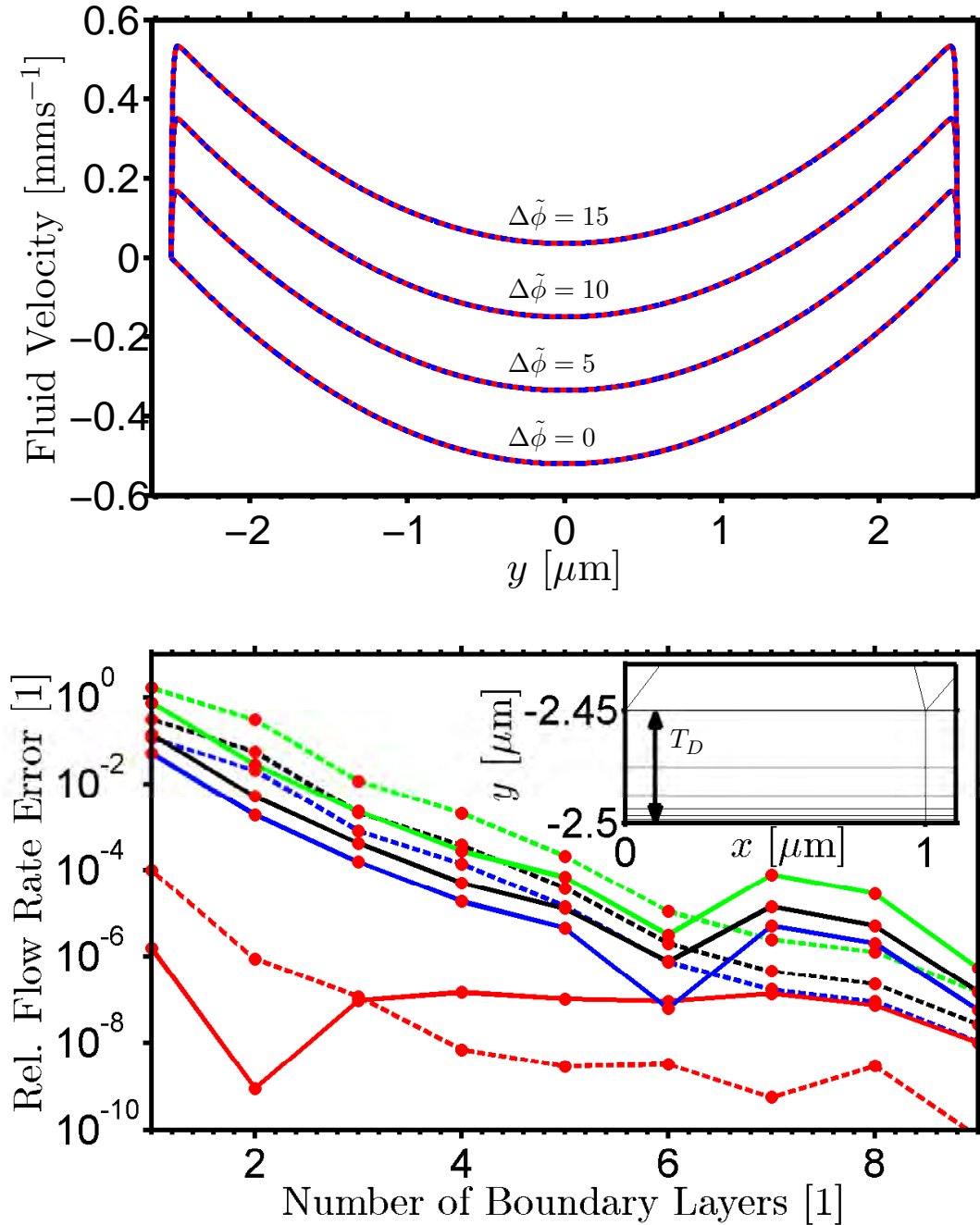


Figure 4.4: Top: Velocity in the x direction along a vertical cut through the center of the channel. Blue is the theoretical value produced from the potential, while red is the COMSOL model solution. Driving potential across the channel is from the bottom going up: 0, 5, 10, 15 thermal voltages. Bottom: Mesh convergence for number of boundary layers with a constant total thickness of $T_D = 50$ nm for the full lines and $T_D = 100$ nm for the dashed lines. Each subsequent layer is twice as thick as the preceding one. Colors correspond to different driving potentials across the channel as follows: Red - 0, Blue - 5, Green - 10, Black - 15.

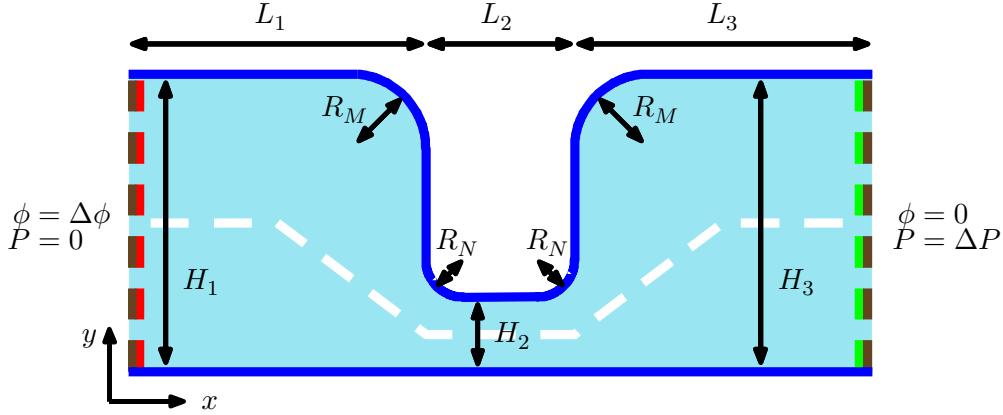


Figure 4.5: Sketch of the 2D channel with a narrow region with boundary conditions marked with the introduced color code. Full blue lines are walls with a surface charge, $\sigma_s = -0.02 \text{ C m}^{-2}$, while the colored dashed lines are open boundaries. The dashed white line is where the line cut is made for explicit comparisons. The angle of the sloping part is always 45 deg and the parts parallel to the x axis are always in the center of the channel. There could be a pressure drop (ΔP), but in the remaining of the section it is zero. Furthermore there is a variable potential drop ($\Delta\phi$) across the narrow part.

4.3 Step 3: Two Species Ion Solution in Infinite Parallel Plate Channel with Narrowing

In this section the same numerical model tested in the previous section is used again. This is the model described in section 3.7.1. The difference to the previous section lies in the shape of the geometry. Instead of a straight line channel we now wish to introduce a narrow part, comparable in height to the Debye length. The structure with important dimensions and applied boundary conditions can be seen in figure 4.5.

The rounded corners are introduced to mimic real world properties. Also they serve to avoid sharp corners, where the resolution needed might be prohibitive timewise for the calculation. Both the rounded corners and the narrow channel have to be meshed properly. The larger corners, $R_M = 0.5 \mu\text{m}$, can be handled the same way as other walls due to their relatively large curvature. The smaller corners, $R_N = 100 \text{ nm}$, are different. These and a part of the narrow channel mesh can be seen in figure 4.6. As the numerically solved equations are unchanged compared to those used when the boundary layer mesh convergence was performed, the results of that test must carry over. This means that a mesh which has the same or better resolution is converged. Inside the narrow part, the height might not always be enough to leave space for a total thickness of $T_D = 50 \text{ nm}$ boundary layers on both sides. This could result in weird meshes. In order to control the mesh, the number of boundary layers has to be reduced to make room for a bulk mesh. Therefore instead of seven layers, only four boundary layers are used. This means the

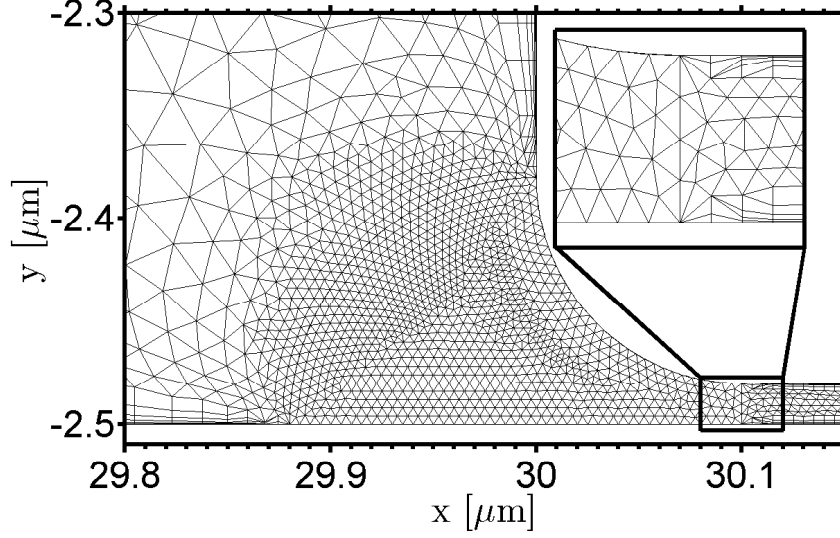


Figure 4.6: Figure of the mesh used close to and in the nano channel. The inset shows a close up of the nano channel. The mesh inside has a maximum size of $T_N = 5$ nm. Only 4 boundary layers are used inside the nano channel.

last layer is approximately 5 nm thick, and therefore this is the size parameter chosen for the bulk mesh in the narrow channel, $T_N = 5$ nm. The mesh is thus always finer than what was found to be converged in the boundary mesh analysis. This also means that the resolution along the channel is very fine. If the narrow part is long or gets large, this fine mesh might be prohibitive for the calculational time. In this case another mesh analysis could be carried out to optimize or alternatively one could revert back to using more layers and a coarser narrow channel bulk mesh. In order to avoid badly scaled elements on the R_M corners, and to connect the different boundary meshes, the bulk mesh of the nano channel is extended out to include the minimum quarter circle that includes all of the R_M curvature and has its center on the opposite wall.

As previously hinted, it is now time to perform the bulk mesh convergence analysis. The relative error of different parameters can be seen in figure 4.7 for different maximum bulk mesh sizes, T_B . The relative error is calculated with respect to a reference, which here is taken to be $T_B = 300$ nm. The relative error, E , is calculated by

$$E(T_B) = \frac{\int_{\Omega} |f(x, y, T_B) - f(x, y, T_B = 300 \text{ nm})| \, dA}{\int_{\Omega} |f(x, y, T_B = 300 \text{ nm})| \, dA} \quad (4.6)$$

where $f(x, y, T_B)$ can be any variable, or combination of variables that are determining for the system. A determining variable could be the concentration fields or the potential

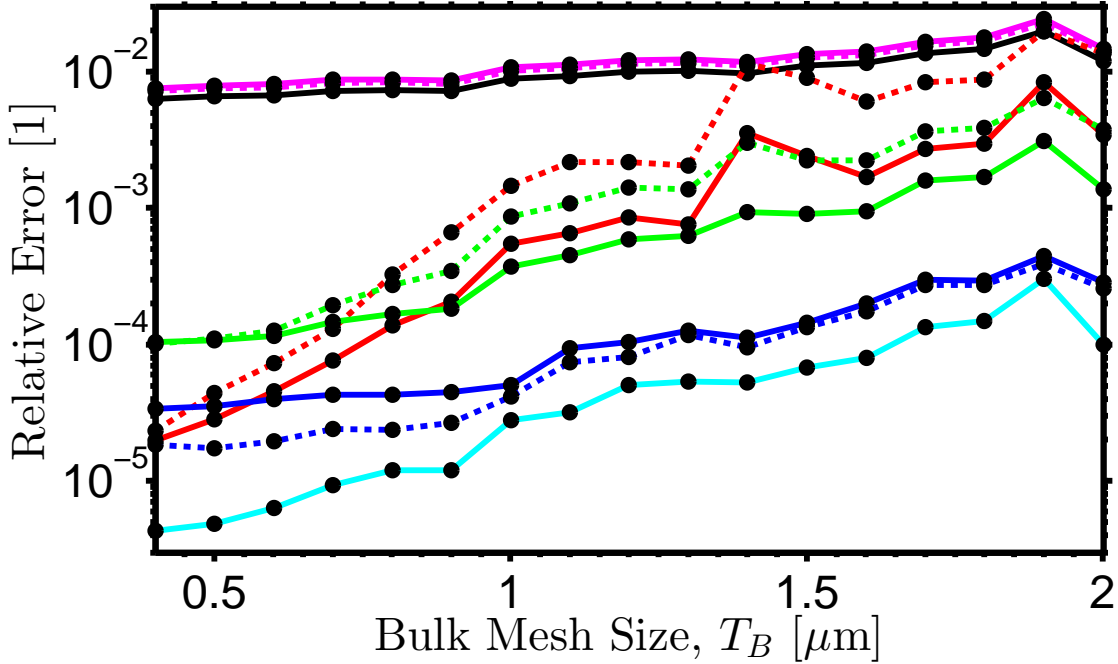


Figure 4.7: Graph of the integrated relative error of different variables for variable bulk mesh parameter, T_B . The black dots mark the data points. The color code is red for the velocity, x and y components being the full and dashed lines respectively. The blue full and dashed lines are the concentrations $\exp(\tilde{c}_1)$ and $\exp(\tilde{c}_2)$ (not to be mistaken with the redefined concentrations). The green full and dashed lines are the ion flow of the two species in the x direction, \tilde{J}_{1x} and \tilde{J}_{2x} . The cyan line is the potential, $\tilde{\phi}$. The magenta lines are the derivatives of the redefined concentration variables \tilde{c}_1 and \tilde{c}_2 in the x direction. The black line is the derivative of the potential in the x direction, $\partial_x \tilde{\phi}$. The error in the pressure is not shown here, because it is orders of magnitude below all the lines shown and does not change with mesh improvements. Geometric parameters used were $H_1 = H_3 = 5 \mu\text{m}$, $H_2 = 20 \text{ nm}$, $L_1 = L_3 = 30 \mu\text{m}$, $L_2 = 1 \mu\text{m}$. External parameters were $\Delta\tilde{\phi} = 20$ and $\Delta\tilde{P} = 0$. All mesh parameters as previously stated and $D_1 = D_2 = 2 \cdot 10^{-9} \text{ m}^2 \text{ s}^{-1}$.

which are included directly in the constituting equations or the ionic current, $\tilde{J}_i k$ which influences indirectly through the ionic species conservation equations.

Taking a closer look at figure 4.7, there is a clear overall exponential convergence taking place for all the variables shown. However, the relative error levels for the derivatives, $\partial_x \tilde{\phi}$, $\partial_x \tilde{c}_1$ and $\partial_x \tilde{c}_2$ (black and two magenta lines), converges much slower than those for the calculated variables, u , v , $\exp(\tilde{c}_1)$, $\exp(\tilde{c}_2)$ and $\tilde{\phi}$ (red full/dashed lines, blue full/dashed lines and cyan full line). This could be due to the mixed boundary conditions, or the mesh being optimized for the variables themselves. In any case, the most important thing is that there are no unforeseen jumps that could indicate a wrong mesh. Also, the most

important mixed convergence parameters, the ionic flows, \tilde{J}_{1x} and \tilde{J}_{2x} , marked with the green full and dashed lines respectively, show an exponential convergence. The conclusion is that the mesh is converged. For a mesh finer than about $T_B = 1 \mu\text{m}$ there is a shift in the positive ion concentration (blue solid line), where it becomes almost flat. This could be the point where the error in the boundary mesh becomes significant compared to the bulk. This would also explain why the relative error in the two concentrations diverge, as they are roughly the same in the bulk, but once the errors in the boundary dominates, the larger positive concentration there means a larger error, while the overall integrated concentrations are roughly equal for the two species. The relative errors for a mesh parameter, $T_B = 1 \mu\text{m}$ are below 10^{-3} and are acceptable. The value $T_B = 1 \mu\text{m}$ is therefore used in the remaining report.

One more thing has to be mentioned about the mesh. Since the extension of the charge layer close to the wall depends on the concentration in the bulk, our mesh analysis might be flawed. This is true, but only to a small degree, as there is a square root dependence. Furthermore, the increase in concentration on one side as compared to the depletion on the other side of the ion selective nano channel is small. The side with the decrease will actually see an improvement in mesh as the layer extends further into the bulk. On the side where the concentration increases, there could be a relative decrease of the Debye length by a factor of two. Relatively speaking, this would be the same as doubling the total thickness of the boundary region for the case with unchanged bulk concentration. However, as we saw in the analysis of the boundary mesh, this did not lead to exploding numerical errors. The convergence analysis showed that the only effect of a larger boundary region was a larger overall error.

This concludes the mesh discussion for the remaining report. The final values chosen for the bulk mesh, the boundary mesh, and the mesh inside the nanochannel are $T_B = 1 \mu\text{m}$, $T_D = 50 \text{ nm}$ and $T_N = 5 \text{ nm}$ respectively, with seven boundary layers outside the nano channel and four inside, both with a growth factor of two.

4.3.1 Models without advection - Dydek model

The first model to compare with is the model developed by Dydek et al. [5]. This model is limited to what happens in a channel leading to a perfect ion selective membrane. This would correspond to the area in figure 4.5 described by L_1 and H_1 , where the narrow part described by L_2 and H_2 is replaced with a perfect ion selective membrane. It is an effective 1D model where the positive and negative ions in the water are treated as being smeared all over the channel, with no field variations across the channel. It is also assumed that advection can be neglected. The ion current in the system is therefore described by the Nernst-Planck equation for each species. The negative ion current is zero due to the ion selective membrane,

$$J_1 = -D_1 \partial_x c_1 - Z_1 D_1 c_1 \partial_x \tilde{\phi} \quad (4.7)$$

$$J_2 = -D_2 \partial_x c_2 + Z_2 D_2 c_2 \partial_x \tilde{\phi} = 0 \quad (4.8)$$

With the assumption that the charges on the walls due to surface reactions are balanced by a net charge in the bulk so that the system is electrically neutral,

$$c_2 = c_1 + \frac{2\sigma_s}{H_1}. \quad (4.9)$$

describes the system. With the boundary conditions,

$$\tilde{\phi}(0) = 0, \quad \tilde{\phi}(L_1) = -\tilde{V}_D, \quad c_1(0) = c_0, \quad (4.10)$$

the equations can be directly solved to give the solution,

$$\tilde{J}_1 = \frac{2D_1}{L} \left(1 + \frac{2\sigma_s}{eH_1c_0} \right) \left(1 - \exp(-\tilde{V}_D) \right) - \frac{D_1}{L_1} \frac{2\sigma_s}{eH_1c_0}, \quad (4.11)$$

where it has been assumed $Z_1 = Z_2 = 1$. The term $\frac{2\sigma_s}{eH_1c_0}$ is not in the original expression in [5], but arises from a lack of charge neutrality in the bulk at the reservoir. In most cases this is much smaller than one, and can be disregarded. It does not change the limiting conductance for large potential differences. As shown by Nielsen and Bruus equation (44), [11], equation (4.11) is only valid if the Debye-Huckel approximation, $\tilde{\zeta} \ll 1$ is valid in the depletion layer. In the case where there is a large charge depletion close to the ion selective membrane (in the case of the numerical model this is a channel), they have shown that the solution approximately approaches a conductance twice as large. Both these model lines are shown in figure 4.8 as the black full and dotted lines. The colored lines represent the full 2D numerical model for different values of H_2 .

Before going into details comparing the analytical and numerical models, the question of the potential difference should be addressed. In the 1D analytical model, the potential is set at $x = 0$ and $= L_1$. In the 2D numerical model we control the potential at $x = 0$ and $x = L_1 + L_2 + L_3$. These two does not match. We could find the potential in the 2D numerical model at $y = 0$, $x = L_1$ but then we would be using the potential on the wall, and far away from the nano channel, which is clearly not the right potential for the 1D analytical model. This is why the white dashed line was introduced in figure 4.5. A cut of the potential along this line is used so we approach the nano channel, which is the ion selective membrane in our 2D numerical system. But using this potential, at $x = L_1$ would still be wrong, as we would effectively already be inside the nano channel at this point, where the potential is very low due to being close to the walls. The best point to use is therefore the potential where the positive ion concentration is lowest, as this is just outside the charged layer in the nano channel. This is the points marked with the black arrows in figure 4.9. The potential drop to this point is denoted \tilde{V}_D , and should in the best possible way correspond to the potential drop used in the 1D analytical model.

Returning to figure 4.8, as H_2 becomes smaller, the more ion selective that whole area becomes, as the average charge concentration becomes larger. This can be seen in the

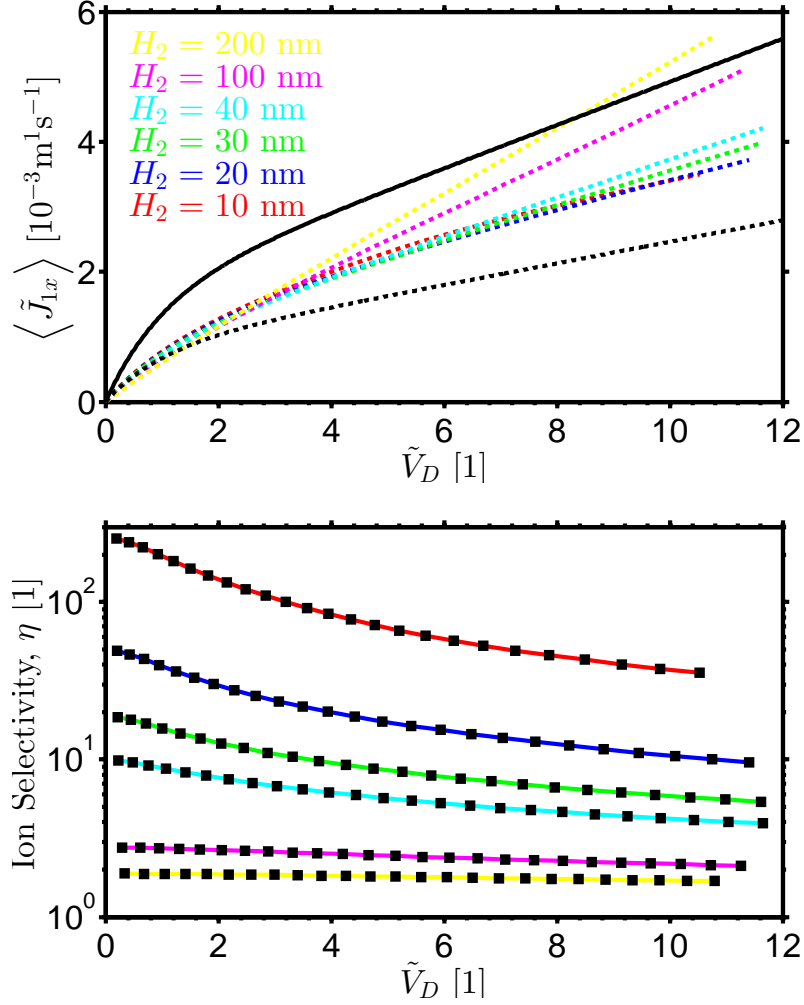


Figure 4.8: Top: The graph shows the positive average ion current for the Dydek model (equation 4.11) which is the dotted black line, the model with the factor two correction, which is the black line, and the full 2D numerical results as the coloured lines. The parameters used were $H_1 = H_3 = 1 \mu\text{m}$, $L_1 = L_3 = 5 \mu\text{m}$, $L_2 = 1 \mu\text{m}$, $R_M = 0.5 \mu\text{m}$, $R_N = 100 \text{nm}$, $\Delta\tilde{P} = 0$, $D_1 = D_2 = 2 \cdot 10^{-9} \text{m}^2 \text{s}^{-1}$, $\sigma_s = -0.02 \text{Cm}^{-2}$, $Z_1 = Z_2 = 1$ and 1 mM concentrations at the openings to the reservoirs. The average x component of the current in the numerical model was found parallel to the y axis down the center of the region defined by L_1 and H_1 . Bottom: Graph of the ion selectivity as a function of potential. The color code is the same as for the top graph. Each subsequent black point corresponds to an increase in $\Delta\tilde{\phi}$ of one, up to a maximum of $\Delta\tilde{\phi} = 25$.

bottom part of figure 4.8. Here η is defined as

$$\eta = \left| \frac{\langle \tilde{J}_{1x} \rangle}{\langle \tilde{J}_{2x} \rangle} \right|, \quad (4.12)$$

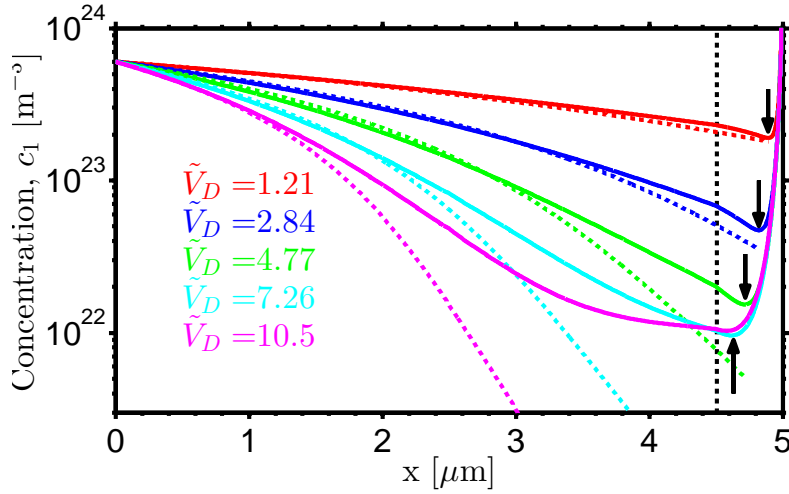


Figure 4.9: Graph of the concentration along the white dashed line sketched in figure 4.5. The full lines are the 2D numerical model, while the dashed lines represent the 1D analytical model for different potential differences, for a channel height of $H_2 = 10$ nm. Other values are as described in figure 4.8. The vertical dashed black line is the point where the cut line (dashed white line) leaves the center of the channel and starts to directly close in on the nano channel. The black arrows mark the minimum concentration point. The potential drop, $-\tilde{\phi}$, at this point is the potential drop used for the analytical model, \tilde{V}_D .

where the average in general can be taken orthogonally across the channel at any point, but in this case is taken at $x = \frac{1}{2}L_1$. The very high values of η justifies that the 1D analytical model and 2D numerical model can be directly compared. Also, this shows that the narrow channel does in fact work as an ion selective membrane when H_2 is sufficiently small. This is also seen in how the average ionic current approaches a specific function as H_2 decreases. Even though it is not a perfect ion selective membrane, it can be pretty close. Note how the selectivity decreases with increasing potential difference. This is not the effect of de-protonation in the nano channel (which will be discussed later), as this is not included in the model yet, but instead seems to be some intrinsic effect, most likely due to charge vacation from the potential barriers being lowered or stronger diffusion out of or into the nano channel. This should be investigated further.

There are a couple of explanations as to why the 1D model and the system does not match perfectly. The most likely is that the 1D model neglects the difference between the bulk current and the current close to the surface. As shown by Nielsen and Bruus, [11], equation (46) in the paper, this causes the model to break down at higher potential differences, due to the creation of the charge depletion layer. This means the Dydek model should be good for small potential differences, which is also what is seen, and then become progressively worse as the potential increases, before finally, in the limit of a large depletion (large potential difference) approaching twice the conductance. The break down of the Dydek

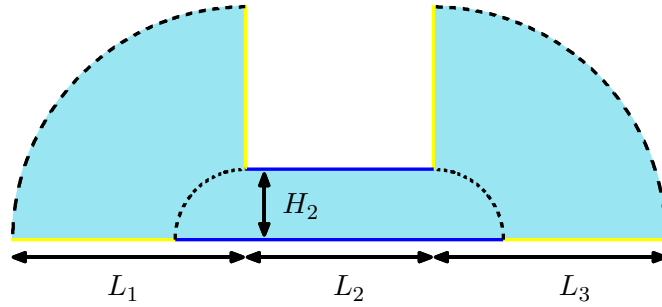


Figure 4.10: Sketch of the system used to derive the Yossifon model.

model is actually what is seen, but it is perhaps much more illuminating to see it from the concentration side, in figure 4.9. For large potentials, the relative error at $x = L_1$ is huge (magenta/cyan lines), while it is small for low potentials (red/blue lines).

To sum up, there is not a quantitative match between the 2D numerical model and the 1D models, but there is a qualitative match. This strongly suggests that the 2D physics in the numerical model are implemented correctly. The differences between the models might be explained by faulty assumptions in the 1D models, or effects outside of the area defined by L_1 and H_1 in the 2D model. Therefore the next section deals with an analytical model that tries to include the narrow part as well as the connecting channels.

4.3.2 Models without advection - Yossifon model

In this section the numerical 2D model will be compared to the model developed by Yossifon et. al., [18]. The model is based on the sketch shown in figure 4.10. Much like the model by Dydek et al., it averages the charges in order to reduce the problem to one dimension. However, as seen in the figure, area one and three are treated in cylindrical coordinates, and the average is done along the quarter circle, so only the radial component is left. This means the equations to solve are

$$0 = \left(\frac{1}{x - L_1} + \partial_x \right) \left(\partial_x c_i + Z_i \partial_x \tilde{\phi} \right) \quad 0 < x < L_1 - H_2 \quad (4.13a)$$

$$0 = \partial_x \left(\partial_x c_i + Z_i \partial_x \tilde{\phi} \right) \quad L_1 - H_2 < x < L_1 + L_2 + H_2 \quad (4.13b)$$

$$0 = \left(\frac{1}{x - L_1 - L_2} + \partial_x \right) \left(\partial_x c_i + Z_i \partial_x \tilde{\phi} \right) \quad L_1 + L_2 + H_2 < x < L_1 + L_2 + L_3 \quad (4.13c)$$

$$\left(\frac{1}{x - L_1} + \partial_x \right) \partial_x \tilde{\phi} = -\frac{e^2}{\epsilon k_B T} (Z_1 c_1 + Z_2 c_2) \quad 0 < x < L_1 - H_2 \quad (4.13d)$$

$$\partial_x \partial_x \tilde{\phi} = -\frac{e^2}{\epsilon k_B T} (Z_1 c_1 + Z_2 c_2) \quad L_1 - H_2 < x < L_1 + L_2 + H_2 \quad (4.13e)$$

$$\left(\frac{1}{x - L_1 - L_2} + \partial_x \right) \partial_x \tilde{\phi} = -\frac{e^2}{\epsilon k_B T} (Z_1 c_1 + Z_2 c_2) \quad L_1 + L_2 + H_2 < x < L_1 + L_2 + L_3 \quad (4.13f)$$

in steady state, where the Z_i contains the sign, along with boundary conditions

$$c_1(0) = c_2(0) = c_0, \quad (4.14a)$$

$$c_1(L_1 + L_2 + L_3) = c_2(L_1 + L_2 + L_3) = c_0, \quad (4.14b)$$

$$\tilde{\phi}(0) = 0, \quad (4.14c)$$

$$\tilde{\phi}(L_1 + L_2 + L_3) = -\Delta\tilde{\phi}. \quad (4.14d)$$

Also the fields have to be continuous and the derivative has to be continuous between region one and two, and region two and three in order to ensure no artificial point charges and a continuous ionic current at these boundaries.

The above model has been implemented in weak form in COMSOL, and the solution is compared to the full 2D model (with advection turned off) in figure 4.11. From the figure it is clear that the model is quantitatively wrong. The ionic currents are off by a factor of four, and the concentration fields that should match best, the averaged 2D model and the Yossifon model, do not even qualitatively match for all cases. Only the concentration along the white dashed line has a qualitative resemblance, but the Yossifon model vastly underestimates the size and the depletion of the depletion layer in front of the nano channel.

The only somewhat redeeming factor for the Yossifon model, is that it predicts a falling ion selectivity with increasing $\Delta\tilde{\phi}$, which means the addition of area two in the model works as a non-perfect ion selective membrane. Furthermore, the geometry does not perfectly match, but this is not enough to warrant the large difference between the models. The

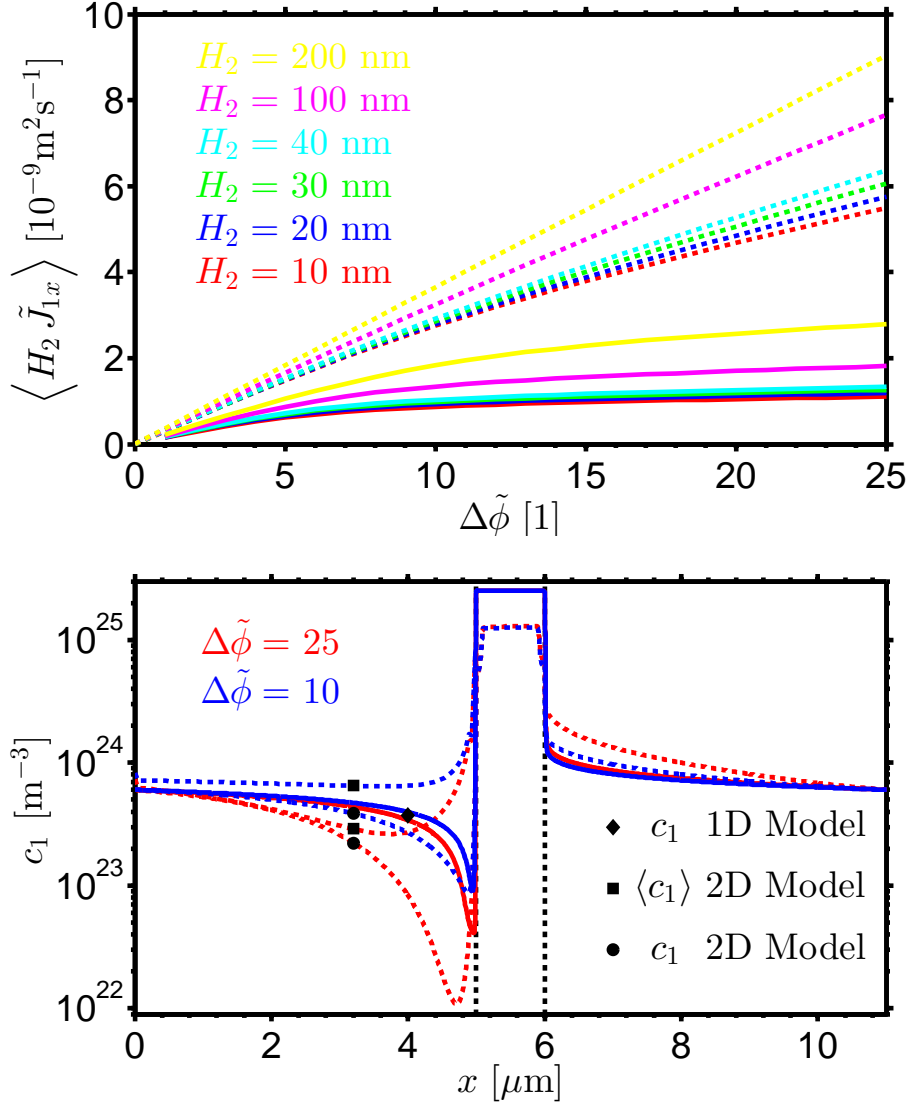


Figure 4.11: Comparisons between the Yossifon model, and the 2D model without advection. The cuts for the 2D model are along the dashed white line in figure 4.5. The parameters used are the same as those used in figure 4.8, except for $H_1 = H_3 = 20 \mu\text{m}$, to get as close to the case of a radial geometry in those regions. Top: Plot of the integrated ionic current on a line down the center of area two for different heights of the nano channel. The dashed lines are the 2D numerical model, while the full lines are the Yossifon model. Bottom: Comparison of the concentration fields for two different potential differences for $H_2 = 10 \text{ nm}$. This is done for field along the dashed white line and for the quarter circle average both in the 2D numerical model together with 1D Yossifon model.

Yossifon model is missing some important physics by averaging the concentrations. This is the same problem the Dydek model had.

4.3.3 Models with advection - Nielsen and Bruus model

In this chapter the effects of enabling advection in the model are studied. One analytical model that includes advection is the model developed by Nielsen and Bruus, [11]. Like the Dydek model it only incorporates the area in the 2D model described by H_1 and L_1 and assumes a perfect ion selective membrane. It is based on the assumption that it is possible to split the problem into a transverse part that deals mainly with the surface effects, and a bulk part that only evolves along the channel. Therefore it also ignores flow fields across the channel close to the membrane. I will not go further into detail with the derivation, since it is lengthy, but simply refer to the paper. For comparison to the 2D numerical model developed here, the full analytical solution, described from equation (47) to equation (51) in the paper is used. The final equation for the average positive ion current density, equation (51b) in the paper can be rewritten into the parallel plate geometry and the variable convention used in this thesis as

$$\begin{aligned}
\langle \tilde{J}_{1x} \rangle = & \frac{2D_1}{L_1} \left[\left(1 + 16 \frac{k_B T \epsilon}{H_1 e \sigma_s} \right) \left(1 - \exp \left(-\tilde{V}_D \right) \right) - \frac{2\sigma_s}{e c_0 H_1} \left(1 + 2 \frac{\epsilon k_B^2 T^2}{\eta D_1 e^2} \right) \tilde{V}_D \right. \\
& - 8 \sqrt{\frac{2k_B T \epsilon}{e^2 c_0 H_1^2}} \left(1 + 2 \frac{\epsilon k_B^2 T^2}{\eta D_1 e^2} \right) \left(1 - \exp \left(-\frac{\tilde{V}_D}{2} \right) \right) \\
& - 16 \sqrt{\frac{2k_B T \epsilon}{e^2 c_0 H_1^2}} \frac{\epsilon k_B^2 T^2}{\eta D_1 e^2} \left[1 + \log \left(\sigma_s \sqrt{\frac{2}{c_0 k_B T \epsilon}} \right) \left(1 - \exp \left(-\frac{\tilde{V}_D}{2} \right) \right) \right. \\
& \left. \left. - \frac{1}{2} \tilde{V}_D \exp \left(-\frac{\tilde{V}_D}{2} \right) \right] \right]. \tag{4.15}
\end{aligned}$$

The full above expression is used in the following comparison between 2D numerical model and the analytical model. However in the following numerical investigations we are either in the limit where it could be well approximated by only keeping the first two groupings, as also noted by Nielsen in deriving equation (52b), or in the limit where the expression is not valid at all.

In deriving equation (4.15), multiple assumptions were made. There are perhaps three assumptions which are more important for us, in order to compare our numerical 2D results to the analytical model.

The first is the assumption of a perfect ion selective membrane, which we can approximate in our 2D numerical model by decreasing the size of H_2 . In all the graphs in figure 4.12 the 2D numerical model is observed to converge towards some limiting function as H_2 is decreased. The characteristic size is seen to be about 50 nm in (a) and a bit less in (d), while it is much lower in (b) and much larger in (c). This indicates that the physics inside the nano channel is somewhat affected by the surrounding channels. One can therefore not just assume any two identical nano channels will work the same way when connected to different connecting channel.

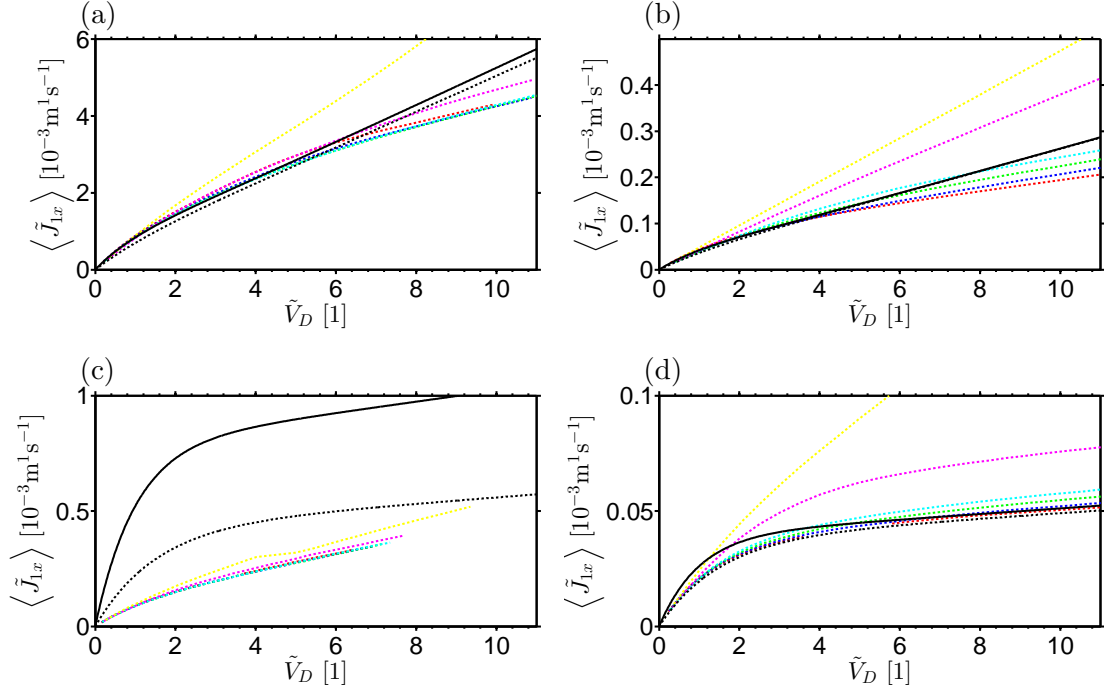


Figure 4.12: Figures showing the evolution of the average positive ion current density, in the 2D numerical model. The same definition for \tilde{V}_D as explained in figure 4.9 is used. The color code is the same as used in the Dydek and Yossifon models: Red: $H_2 = 10$ nm, Blue: $H_2 = 20$ nm, Green: $H_2 = 30$ nm, Cyan: $H_2 = 40$ nm, Magenta: $H_2 = 100$ nm, Yellow: $H_2 = 200$ nm. The black lines originate from equation (4.15), which is the model by Nielsen. The dimensions of the system are (a) $H_1 = H_3 = 1 \mu\text{m}$ and $L_1 = L_3 = 5 \mu\text{m}$. (b) $H_1 = H_3 = 1 \mu\text{m}$ and $L_1 = L_3 = 100 \mu\text{m}$. (c) $H_1 = H_3 = 20 \mu\text{m}$ and $L_1 = L_3 = 5 \mu\text{m}$. (d) $H_1 = H_3 = 20 \mu\text{m}$ and $L_1 = L_3 = 100 \mu\text{m}$. In other words going horizontally increases the length by a factor 20 while going down vertically increases the height by a factor 20.

The second assumption is that the channel is much longer than the height, $H_1 \ll L_1$. This is clearly not the case for figure 4.12(c). Not surprisingly, this figure also shows the largest differences between the analytical and numerical models.

The third assumption is not obvious, and for most channel designs it would hold true, but in figure 4.12 (a) and (b) parameters have been chosen that lands the analytical model in a problematic situation. First off, the analytical model assumes that the Debye length is much smaller than the channel width, and that the Gouy-Chapman solution is therefore valid. Normally this would be true, but as the potential difference is increased, a depletion layer is formed in front of the nano channel. As the bulk concentration is decreased, the depletion layer grows. When the bulk concentration has been lowered by a factor 100, the Debye length grows with a factor 10. For a channel of height $H_1 = 1 \mu\text{m}$ and an original Debye length of $\lambda_D \approx 10$ nm the surface effects can suddenly take up half the channel!

That means the assumption of charge neutrality in the bulk, the Gouy-Chapman expression, and the split up into surface and bulk effects in the model is no longer valid, and the model breaks apart. This can be seen in figure 4.12 (a) and (b) where the analytical and numerical models agree for a low potential drop, \tilde{V}_D , which means little depletion. When the potential difference is increased the analytical model stops working, and the limiting conductance predicted by it is wrong. For the case of a 20 times wider channel, in (c), the models quantitatively agree in the limit of large potential differences, as expected, even for a very depleted (factor 100) depletion zone. However for small potential differences there are some differences between analytical model and numerical model. The numerical models do not converge perfectly towards the analytical model for H_2 going to zero. The main reason for this is most likely to be found in the fact that the ion selective nano channel is not an evenly distributed ion selective membrane as assumed in the analytical model.

If we introduce a geometrical factor of $\frac{2}{3}$ in all the exponential terms, so for instance the first one reads $\exp\left(-\frac{2}{3}\tilde{V}_D\right)$ instead of $\exp\left(-\tilde{V}_D\right)$, and use the length of the dashed white line in figure 4.5 instead of L_1 as the total length, then the dashed black line in figure 4.12 (d) is obtained. This modified model has the attributes the original was missing and has a much better match.

To justify the change in the exponentials, we need to remember that they arise from the depletion zones in the bulk. This means the depletion zone is forming at two thirds of the usual rate due to the geometry. This could be due to flow roll mixing of surface and bulk concentrations near the ion selective membrane, as seen in figure 4.13. Technically this figure is for a different, smaller geometry, but the behaviour of decreasing rolls for increasing H_2 is qualitatively the same. The flow rolls close to the membrane are not part of the analytical model, which only assumes that the backflow in the bulk is equal to the forward flow at the surface. For $H_2 = 200$ nm the flow rolls are reduced in strength, which is reflected in the yellow line in figure 4.12 (d) reaching the limiting conductance much earlier than the red line.

Looking at why the length should be changed it can be observed that both the surface and bulk paths are increased. The change in the length for the surface term is from an average between the two paths for the surface currents on the two surfaces, which is $\frac{H_1-H_2}{2}$. Likewise it is $(\sqrt{2}-1)\frac{H_1-H_2}{2}$ for the bulk terms, as the velocity field follows the white dashed line. For consistency the bulk length increase is used in both cases. The difference is minute, but notable. The difference in the average current density in the analytical model is -1% for not increasing the length, and $+1\%$ for using the average surface increased length, as opposed to using the bulk increased length.

Even without these geometric effects, the model by Nielsen and Bruus catches the importance of advection, and it shows that the numerical 2D model described throughout chapter 3 is correctly implemented.

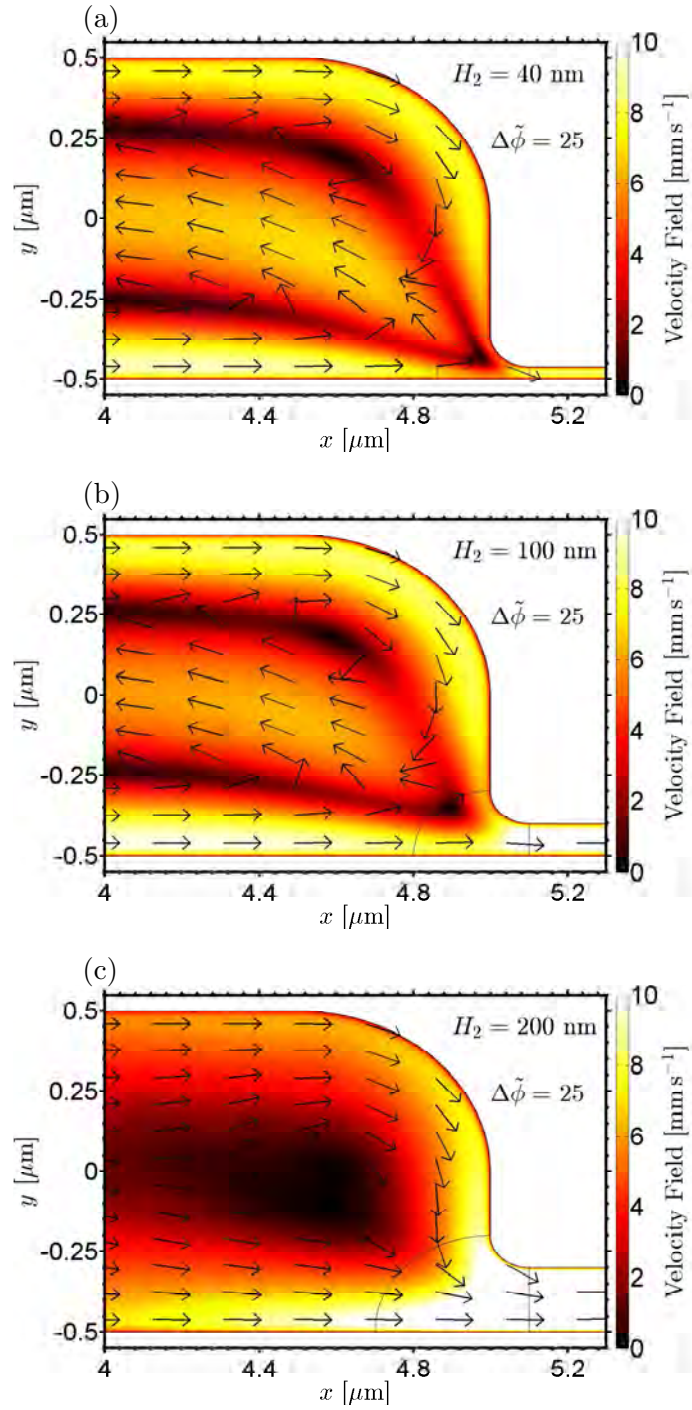


Figure 4.13: Velocity fields close to the nano channel for different heights, H_2 of the nano channel. These are all for the geometry used in figure 4.12 (a), $H_1 = H_3 = 1 \mu\text{m}$ and $L_1 = L_3 = 5 \mu\text{m}$.

There are two open questions left, which were treated in the previous sections for the case of no advection. How does the ion selectivity, η change when advection is included, and what effect does advection have on the concentration fields, in particular the depletion zone. The ion selectivity is shown in figure 4.14. In (a) (b) and (c), the ion selectivity shows the same behavior. The nano channel gets progressively more ion selective when H_2 is decreased, as expected. As in the models without advection, when the potential difference, \tilde{V}_D is increased, the nano channel starts to lose its ion selectivity. However, for nano channels larger than some limit, the ion selectivity starts to increase, as seen for the yellow lines. For the rather large channel in (d), the ion selectivity seems to approach a limiting value as the potential is increased. This is most likely due to ion transportation by advection through the nano channel, which can be quite large due to the very large ion concentrations in this area. The flow leading into the channel can be seen in figure 4.13, which corresponds to figure 4.14 (a) for specific potential differences. As can be seen the pressure driven backflow disappears entirely for $H_2 = 200$ nm. The important thing to remember is that the maximum velocity for a Poiseuille flow scales with the height squared. With a factor 10 change in size, this means a factor 100 change in the effect of advection. Of course the pressure build up at the entrance to the nano channel is decreased when H_2 is increased, but the scaling law goes to show how important the size is. In figure 4.14 (b), which shows the ion selectivity of a very long and narrow side channel, the behaviour for a large nano channel is peculiar. It shows a much greater ion selectivity than the small nano channels, even at low driving potential. This could be a pressure effect of a long channel, where even a small driving potential difference can give a large pressure build up, along with a lower ion current as the electric field for a given potential difference is smaller. This is an important effect to consider in for instance a desalination device and for devices in general.

An analytical model for the behaviour exhibited by the nano channel could be really important for future device engineering and optimization. More work should be applied to develop this. One method could be to use the Debye-Hückel solution for the transverse concentration fields instead of the Gouy-Chapman solution and using the same split up in transverse and parallel fields as done by Nielsen and Bruus in their model. The solution would be wrong as the potential on the walls is much larger than the thermal voltage. However, it is only the overall shape that is changed to be more out in the fluid, and not the total charge in the boundary layer. Therefore the boundary layer conduction without advection will remain largely unchanged. As mentioned in section 4.2, the velocity field is almost the same in the full numerical model and the analytical Debye-Huckel solution, so the advection term might be sufficiently well described that the model is accurate, even for the nano channel where the Debye layers overlap. Another way would be to use the Nielsen and Bruus model for the side channels, and then use an average concentration in the nano channel based on the surface charge.

With the positive effect in ion selectivity of making larger nano channels, one would think this is the way forward in order to increase the depletion layer. But if we look at the concentration profiles, again along the dashed white line, we can see that this is not the

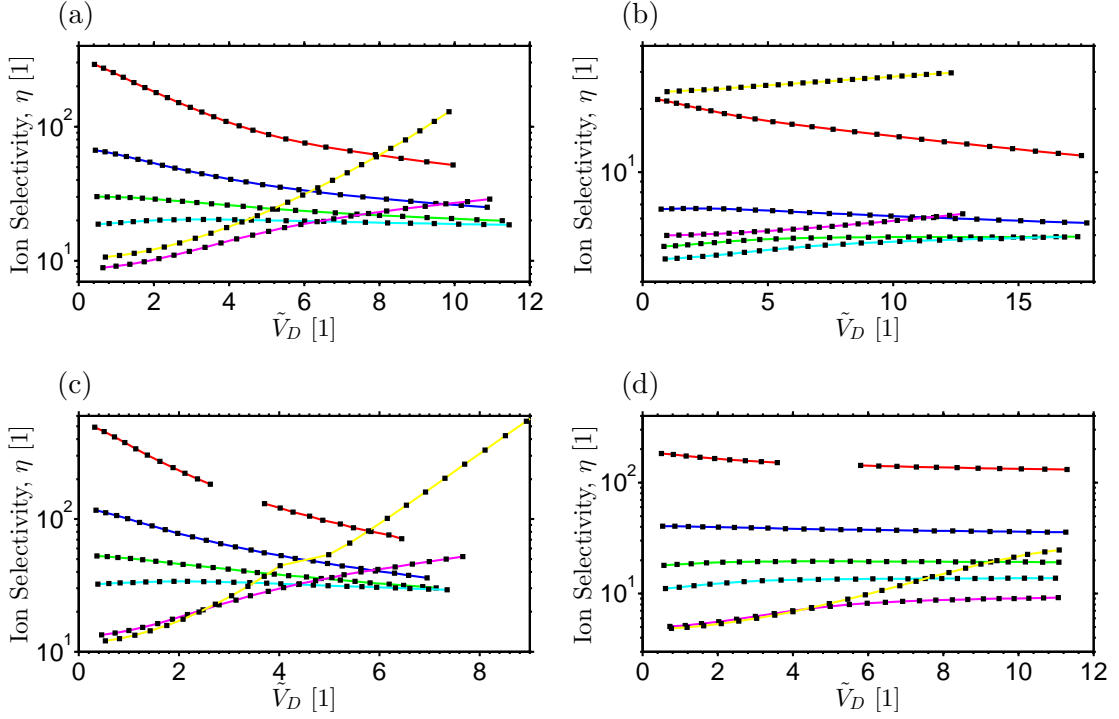


Figure 4.14: Graphs of the ion selectivity (defined in equation (4.12)) for the geometries in figure 4.12. Color code and parameters as in figure 4.12.

case. These profiles can be seen in figure 4.15 for the positive ionic species.

On the left side of the nano channel, the side where the bulk water flow is away from the nano channel and the water near the surface runs into the nano channel, the depletion layer is increased. See figure 4.13. The depletion layer is extended as the ionic currents get an extra contribution away from the nano channel from the fluid flowing away from the nano channel. The only problem with this explanation is the fact that we also see an increase in the size of the depletion layer for $H_2 = 200$ nm. We have to remember that the dashed lines also represent different ion selectivities and not just flow fields. For the case of a small nano channel, the ion selectivity with and without advection is the same (see figure 4.8 and 4.14), but for a large channel it is not so. For the large nano channel in the case without advection, which is the dashed line in figure 4.15, there is an ion selectivity of almost one, and there is naturally no depletion zone. In the case with advection, the advection might not contribute to the depletion zone directly, but by increasing the ion selectivity to at least above 10, the depletion zone turns up, even though it is still small. This means the advection is indirectly creating the depletion zone.

On the right side of the nano channel the story is almost the same, but reversed. For small nano channels there is a flow in the bulk towards the nano channel, and away from

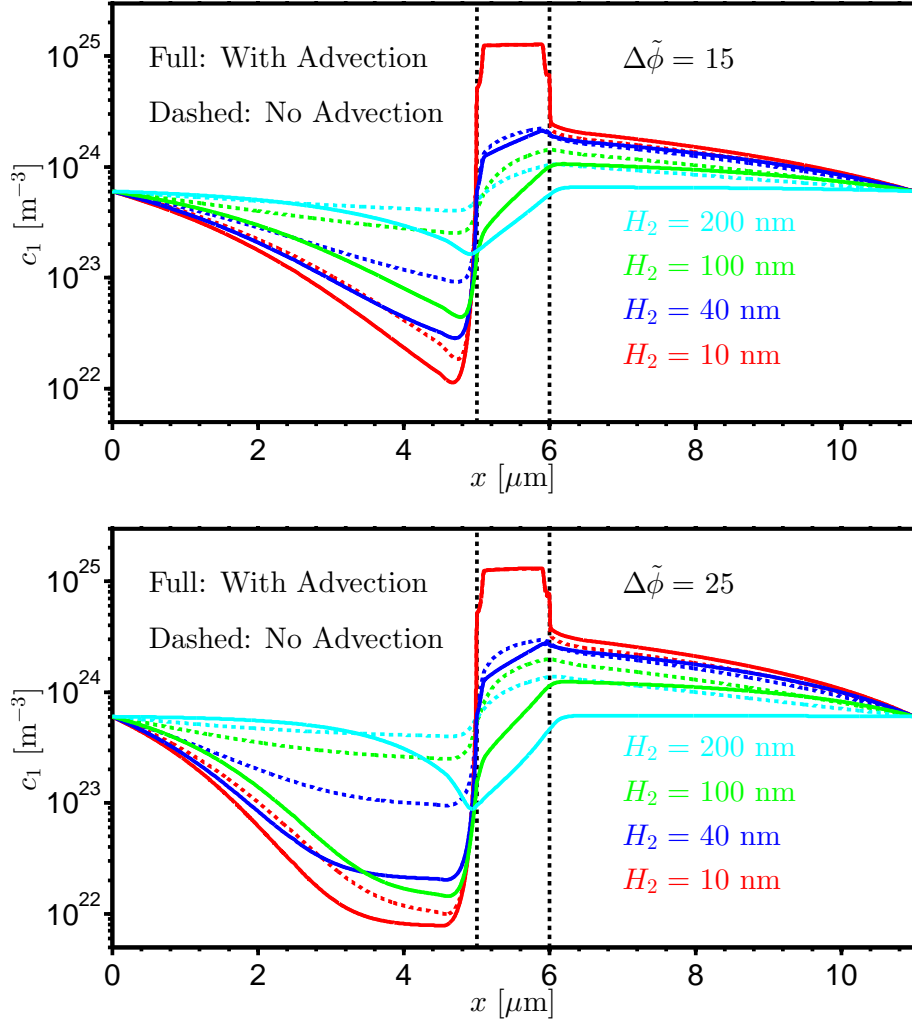


Figure 4.15: Figures showing the concentration profile along the white dashed line shown in figure 4.5 for the geometry and parameters used in figure 4.12 (a) and figure 4.8, $H_1 = H_3 = 1 \mu\text{m}$ and $L_1 = L_3 = 5 \mu\text{m}$. The full lines depict the results of the model with advection, while the dashed lines are the model with advection turned off. The two figures show the same, but for different potential differences. Top: $\Delta\tilde{\phi} = 15$. Bottom: $\Delta\tilde{\phi} = 25$. The vertical dashed black lines represent the two ends of the nano channel.

it in the surface areas. When the nano channel size is increased the fluid flow changes to be outwards from the channel both close to the surface and in the bulk. In the bulk this is a direction change compared to lower values of H_2 . The nano channel delivers enough fluid flow to sustain the flow in the Debye layers, so it does not have to drain the missing fluid from the bulk. For $H_2 = 200 \text{ nm}$ the flow is strong enough that the negative ionic current in the center of the nano channel changes sign at the outflow. Since there is then almost no negative current going towards the membrane on the right side, there is no need

for a concentration gradient to make sure the ion current is conserved. This qualitatively explains the disappearing of the layer of increased concentration on the right side of the ion selective nano channel.

Advection changes the concentration just outside the nano channel, but what about inside the nano channel? Since the water flow into the nano channel is primarily from the surface regime and it goes primarily into the center of the nano channel where the concentrations are lower, there might be extra positive charge in the nano channel. However as it turns out, the integrated positive ionic concentration across the nano channel close to the entrance is increased by less than 0.5% when increasing the height from 100 nm to 200 nm, and the change is even smaller for smaller channels. These numbers are so small that the added net charge from the surface current has no effect on the ion selectivity of the nano channel.

On a closing note, the missing data points for $H_2 = 10$ nm are due to an error in the configuration of the solver. It did not use the previous solution as an initial guess, and therefore had a small chance to fail to converge. If it did not converge the data point is blank, and not included in the final data. In other words it does not affect the results.

4.3.4 Step 3 Summary

The analytical models without advection predicted results that were qualitatively consistent with the 2D numerical model. When advection was turned on in the numerical model, there was a very good fit to the analytical model by Nielsen and Bruus in the case where their model applies. This strongly suggests that the numerical implementation up until this point is correct.

One of the main goals in this thesis was to figure out if it is theoretically possible to microfabricate a channel that acts like an ion selective membranes and then approximate the size requirements. From the analysis in this chapter we have found that this should be possible and that the critical wall to wall size is about 40 nm for realistic system parameters. Beyond this, it was found that the selectivity is naturally inclined to drop in response to a potential difference, if just diffusion and electric effects were introduced. But advection actually plays a large role and has to be taken into account, in which case the selectivity stabilizes, or even increases. Ion selectivities of more than $\eta = 100$ were found to be possible, even for values of $H_2 = 100$ nm and above. But the price to pay for high ion selectivities for these values of H_2 , was a reduction of the depletion zones.

4.4 Step 4: Two Species Ion Solution in Infinite Parallel Plate Channel with Narrowing and Water Splitting

Now we leave the models without water splitting, and the discussion of the nano channel and its ion selective properties, and instead turn our attention to the models with water

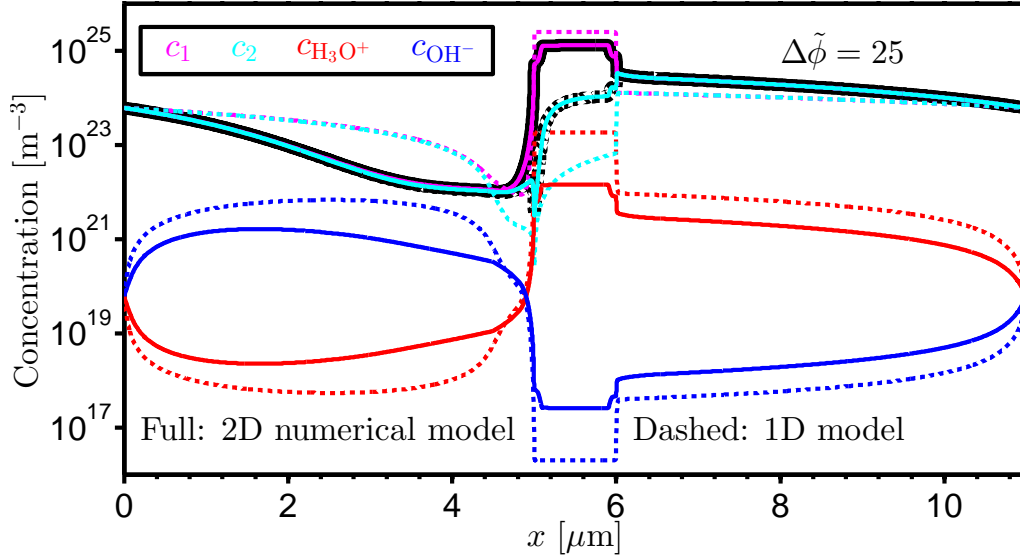


Figure 4.16: Comparison between various concentration profiles along the dashed white line in figure 4.5 in the full 2D numerical model (dashed color lines) and the 1D model by Andersen (full color lines). The black lines are the positive and negative ion concentrations for the model without advection or water splitting. In all cases $H_2 = 10$ nm. Parameters: $H_1 = H_3 = 1 \mu\text{m}$, $L_1 = L_3 = 5 \mu\text{m}$, $L_2 = 1 \mu\text{m}$, $R_M = 0.5 \mu\text{m}$, $R_N = 100$ nm, $\Delta\tilde{P} = 0$, $D_1 = 1.3 \cdot 10^{-9} \text{ m}^2\text{s}^{-1}$, $D_2 = 2 \cdot 10^{-9} \text{ m}^2\text{s}^{-1}$, $D_H = 9.3 \cdot 10^{-9} \text{ m}^2\text{s}^{-1}$, $D_{OH} = 5.3 \cdot 10^{-9} \text{ m}^2\text{s}^{-1}$, $\sigma_s = -0.02 \text{ Cm}^{-2}$, $Z_1 = Z_2 = 1$ and finally 1 mM ion concentration and pH = 7 at the reservoirs. The driving potential in this case is $\Delta\tilde{\phi} = 25$.

splitting. The equations solved in this section are those found in section 3.7.2. The geometry investigated remains the same, that is, the one seen in figure 4.5. There has been some work trying to model the effects of water splitting by for instance Andersen et al., [1], and Nielsen and Bruus [12]. Here the 1D averaged model by Andersen will be used as a test to see if the numerical implementation is done correctly, and then the results of the two models will be compared.

The model by Andersen is, geometrically, a mix of the Yossifon model and the Dydek model, with an added set of Nernst-Planck equations for oxonium and hydronium ions, corresponding to those derived in section 3.5. As in the Yossifon model, the nano channel is modelled by an averaged net charge equal to that on the walls, while there is charge neutrality in the two channels leading to the nano channel. There is an extra layer in the Andersen model, which is the model for deprotonation of the membrane. This model is based on pH changes, and how this affects the surface reactions and thus the net charge of the nano channel. Since surface reactions are not included in the 2D numerical model, this part of the model by Andersen is ignored by having a constant average charge inside the nano channel, independent of pH changes.

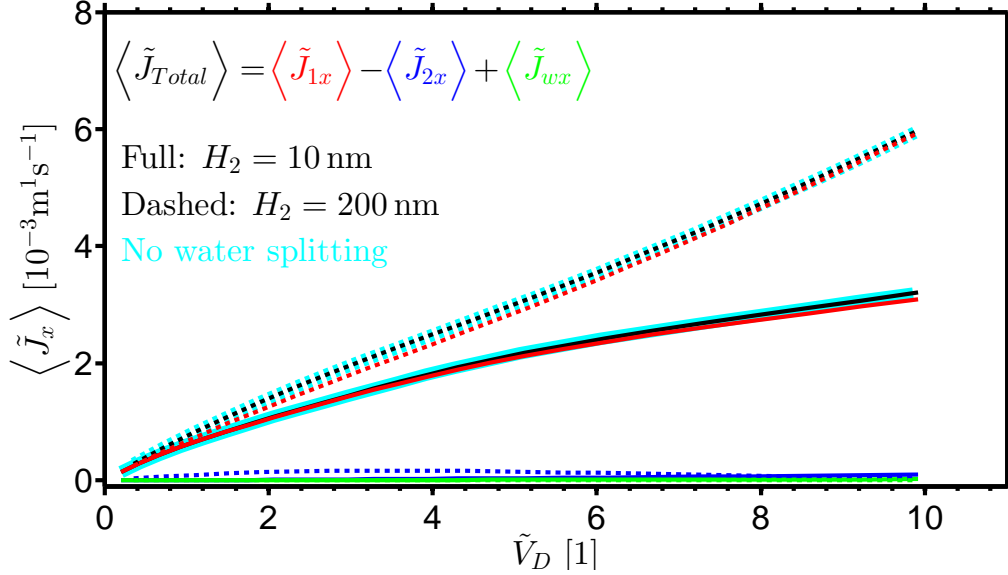


Figure 4.17: Average ionic current densities through the system for the 2D numerical model with and without water splitting for two different sizes of the nano channel. The black line represent the total averaged current in the system and is the sum of the positive ions (red), negative ions (blue) and water ions (green), while the cyan lines are the 2D numerical model without water splitting. Advection is turned on for all cases. Parameters were the same as those used in figure 4.16.

The equations for the 1D model were solved using COMSOL on a 10 nm mesh, and the result can be seen in figure 4.16. In this figure the corresponding concentrations for the 2D numerical model are also shown for the cut along the white dashed line in figure 4.5. These are for the models without advection, both with and without water splitting. Qualitatively the blue and red full curves match their dashed counterparts, and show the same behaviour as reported in the article by Andersen et. al., [1]. This is a clear sign that the numerical implementation is done correctly. There is a quantitative match very close to the membrane, in the region where the cut line slopes from the nano channel to the center of the larger connecting channels. This indicates that the reason for the quantitative disagreement in the other regions could be due to geometric effects. This should be investigated further by for instance distributing many nano channels along the y axis to form a more coherent membrane. Due to time constraints this is not done here.

The ion concentrations, the magenta and cyan curves, do not match. As in the Yossifon and Dydek models, the size of the depletion layers are underestimated. The underlying reason is most likely the same, that the 1D model is not really a good model. Instead one have to consider both bulk and surface effects as done in the model by Nielsen and Bruus. It does however predict the small amount of positive charge in the depletion layer, which

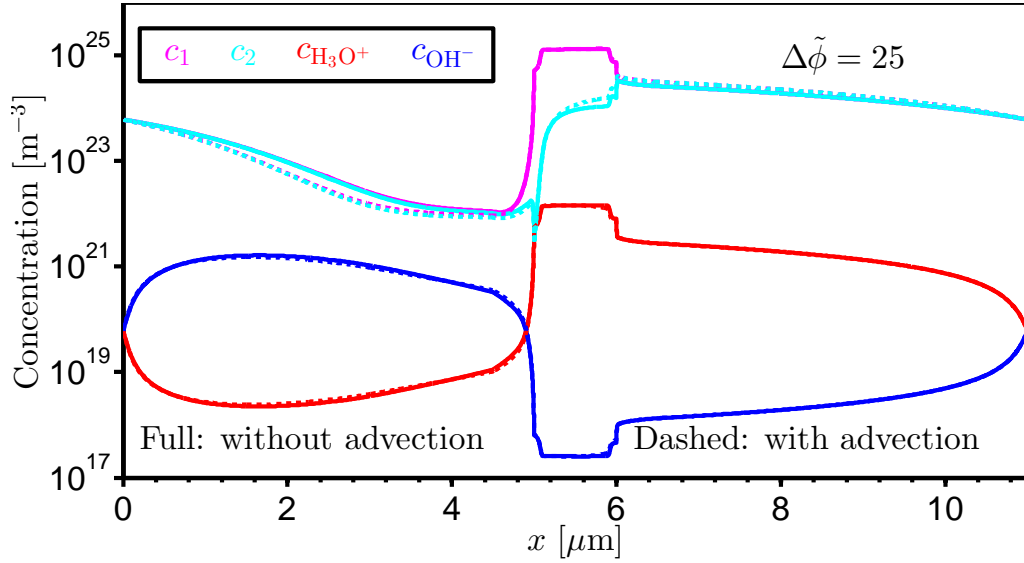


Figure 4.18: Comparison of the concentration profiles in the 2D numerical model with and without advection. Same parameters as in figure 4.16. The driving potential is $\Delta\tilde{\phi} = 25$ in both cases.

is an improvement.

Comparing the full cyan and magenta lines to the black lines, the difference of adding water splitting can be seen. The water splitting does not influence the concentration profiles of the ions.

If we look at the changes in the ion current by adding the effect of self-ionization of water shown in figure 4.17, we see that water splitting ions have no effect on the behaviour of the other ions. The cyan lines, representing the numerical model without water splitting and the black lines that represent the numerical models with water splitting are overlapping. This is not surprising considering the orders of magnitude difference in the concentrations of the normal ions, c_1 and c_2 compared to the hydronium and oxonium ion concentrations. However water splitting might be very relevant for other system parameters, if suddenly the concentrations of hydronium and oxonium ions are comparable to those of other ionic species. This could for instance be if an acid solution is used in the reservoirs, or if a weaker ion concentration in the reservoirs is used. Indirectly water splitting can also play an important role as it is a vital part of the chemical equilibrium on the surfaces, and thus a reason for the surface charge, which is the basis for most of the effects in the system. This is something to look into in the future.

4.5 Step 5: Reservoir imitation by continuously flushed boundaries - The H model

In this last step the geometry is again changed, by adding two additional channels that flush the previous system at the reservoir boundaries (see the figure in the introduction, figure 1.2, or appendix B). The investigations can be seen for different field variables in figure 4.19 and 4.20. If the flushing is too low, the pH change observed in the previous section will start to creep into the flushing channels. This is best seen in the pH plots - when the pressure across the flushing channels is increased, the pH is the same throughout the channel. If there is not enough flushing, there is a huge drop in pH very close to the open boundaries. This is an artefact in the numerical model due to constrained values on the boundaries. This is also an illustration of the problems associated with forcing boundary conditions, and goes to show why it is necessary to introduce the 'weak' boundary constraints on the side channels in the form of the flushing channels.

The pH creep effect is much stronger than the creep of the ion concentrations, which is best seen in the concentration plot. The concentration profile is not changed a lot with increased flushing. However, If flushing is too high, the flow rolls created by the fluid passing the side channel opening, dominates the channel, and might even run into the depletion zone thereby diminishing it. Therefore it is necessary to be in the right regime without too much flushing, but with enough so that the boundary conditions are satisfied. By making the side channels longer, the relative effect of the flow rolls to change the channel length is diminished. The creep out into the flushing channels should likewise be diminished as the generator of all the effects, the nano channel, is further away. Other than this there seems to be no effects that can make experiments with well defined 'reservoirs' difficult to conduct.

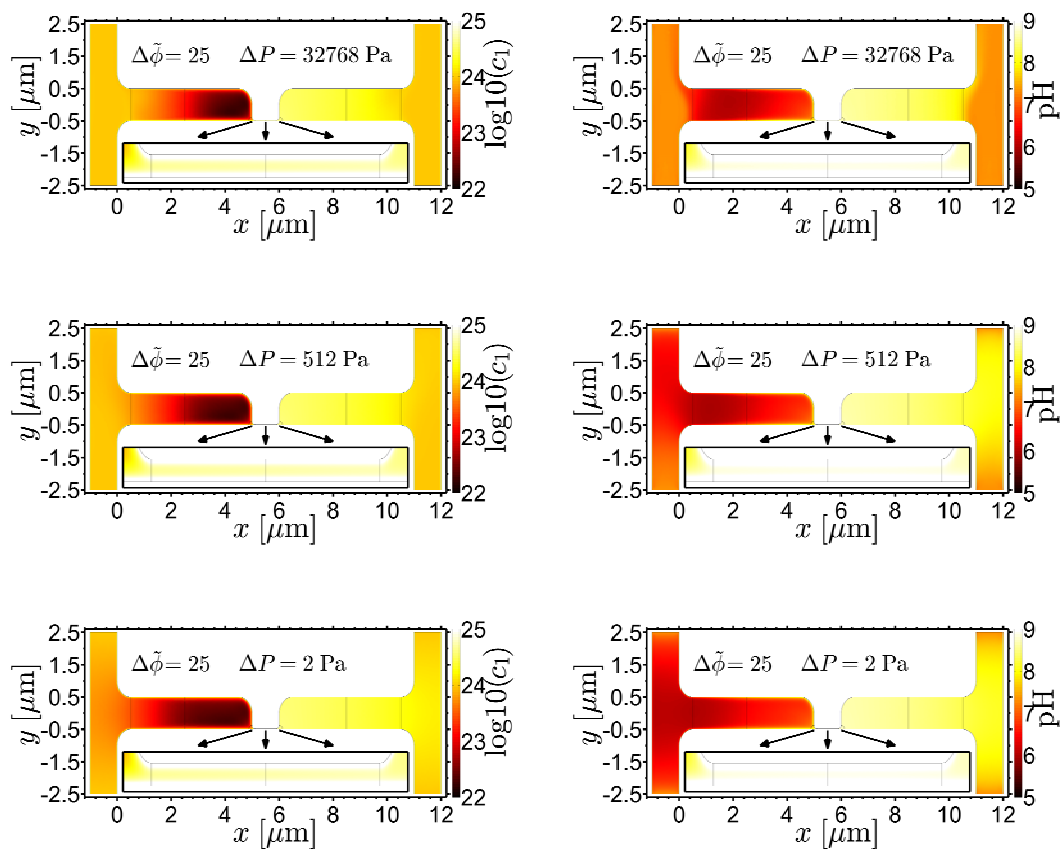


Figure 4.19: Plot of the the concentration (left column), and the pH (right column), for the full 2D system. Parameters as discussed in the end of previous chapter, matching a NaCl water solution.

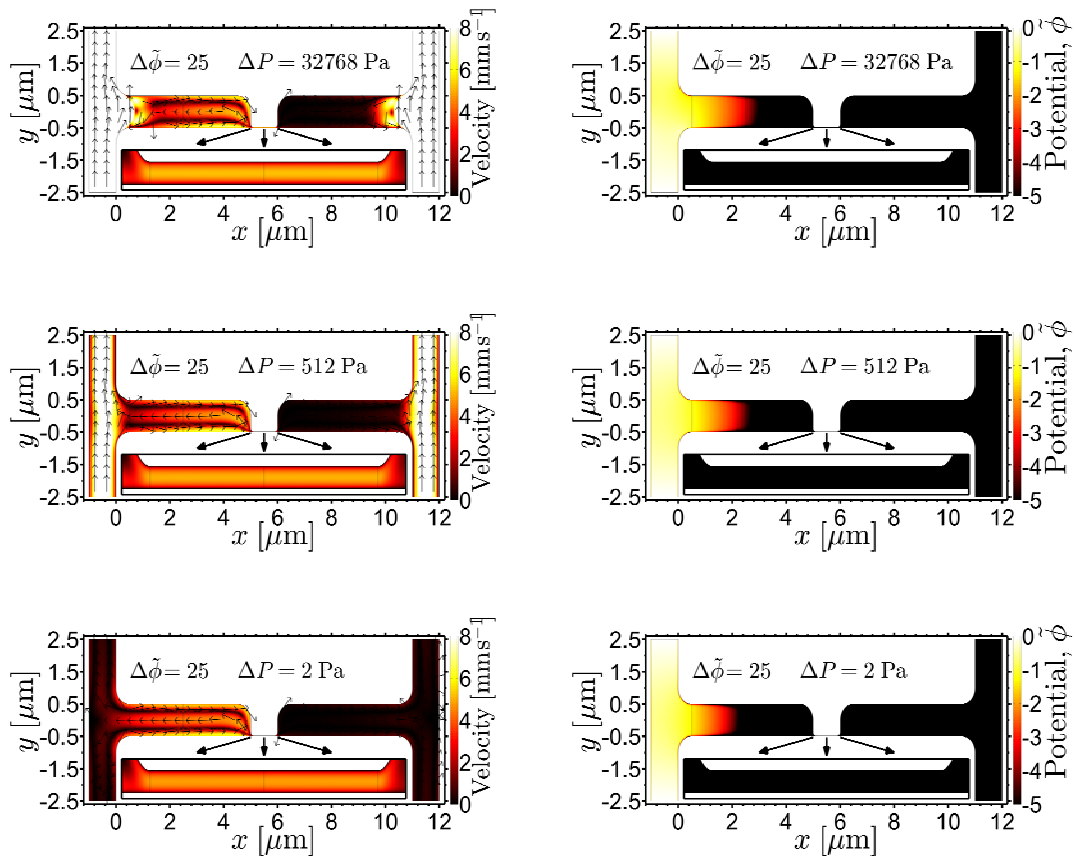


Figure 4.20: Plot of the the velocity (left column), and the electric potential (right column), for the full 2D system. Parameters as discussed in the previous chapter, matching a NaCl water solution.

Chapter 5

Conclusion and Outlook

A non ideal ion selection membrane, in the form of a nano channel, was investigated. It was found that such a structure, with a wall to wall size up to about 50 nm, was ion selective. This is large enough that they can be fabricated using current state of the art cleanroom fabrication processes. The effect of advection could enhance the ion selectivity, so that the selectivity remained high ($\eta > 10$) for larger nano channels. This was shown to be due to advective ion transport becoming equal if not larger than diffusion and electric transport. However, the large advection also meant a disruption of the depletion layer next to the channel, and the conductive behaviour of the connecting channels also changed compared to a normal ion selective membrane.

The 2D numerical model qualitatively agreed with the the 1D models developed by Dydek et al., [5], Yossifon et al., [18], and Andersen et al., [1]. The discrepancies were justified by geometric differences and too simplified models. The model developed by Nielsen and Bruus turned out to be very accurate in the limit where it applied, and the small remaining discrepancy could be explained by effects not included in the model near the ion selective nano channel. Through the gradual extension of the numerical model done throughout the thesis and the analysis it can be concluded that the numerical implementation is correct. Therefore the goal of having a working model to plan and compare to future experiments is achieved.

The effects of including water self-ionization was investigated in the model, and turned out to be negligible for the ion transport and ion concentration distributions for the range of parameters investigated. However more work should be applied for an extended parameter investigation.

The effect of flow controlled boundary conditions was briefly discussed. It should be possible to make more realistic boundary conditions by controlling the flow. However, depending on the exact geometry, this might also influence the transport throughout the system due to propagating flow rolls.

In the future, several things should be investigated. Perhaps most importantly the effect of a dynamic surface charge in the system. With the large pH variations observed, the assumption that it is constant might not hold. From an experimental point of view the possibility to drive the flushing channels in the H-model by electric field should be investigated. The numerical model can also be used to test different desalination devices by changing the geometry.

Bibliography

- [1] M. B. Andersen, M. van Soestbergen, A. Mani, H. Bruus, P. M. Biesheuvel, and M. Z. Bazant. Current-Induced Membrane Discharge. *Physical Review Letters*, 109(10):108301, September 2012.
- [2] Mathias B. Andersen. *Electrokinetics of nanochannels and porous membranes with dynamic surface charges*. PhD thesis, Technical University of Denmark, 2012. <http://web-files.ait.dtu.dk/bruus/TMF/publications/PhD/PhDthesisMBA.pdf>.
- [3] Mathias Bækbo Andersen, Jared Frey, Sumita Pennathur, and Henrik Bruus. Surface-dependent chemical equilibrium constants and capacitances for bare and 3-cyanopropyldimethylchlorosilane coated silica nanochannels. *Journal of colloid and interface science*, 353(1):301–10, January 2011.
- [4] Henrik Bruus. *Theoretical microfluidics*. Oxford University Press, 2nd edition, 2008.
- [5] E. Victoria Dydek, Boris Zaltzman, Isaak Rubinstein, D. S. Deng, Ali Mani, and Martin Z. Bazant. Overlimiting Current in a Microchannel. *Physical Review Letters*, 107(11):118301, September 2011.
- [6] Walter Frei. Comsol.com. <http://www.comsol.dk/blogs/solutions-linear-systems-equations-direct-iterative-solvers/>, 2013.
- [7] Kristian Lund Jensen, Jesper Toft Kristensen, Andrew Michael Crumrine, Mathias Bækbo Andersen, Henrik Bruus, and Sumita Pennathur. Hydronium-dominated ion transport in carbon-dioxide-saturated electrolytes at low salt concentrations in nanochannels. *Physical Review E*, 83(5):056307, May 2011.
- [8] Sung Jae Kim, Sung Hee Ko, Kwan Hyoungh Kang, and Jongyoon Han. Direct seawater desalination by ion concentration polarization. *Nature nanotechnology*, 5(4):297–301, April 2010.
- [9] Janina Kneipp, Harald Kneipp, Burghardt Wittig, and Katrin Kneipp. One- and Two-Photon Excited Optical pH Probing for Cells Using Surface-Enhanced Raman and Hyper-Raman Nanosensors. *Nano Letters*, 7(9):2819–2823, 2007.
- [10] J. A. Manzanares, S. Mafid, and H. J. Reiss. Numerical Simulation of the Nonequilibrium Diffuse Double Layer in Ion-Exchange Membranes. *Journal of Physical Chemistry*, 97:8524–8530, 1993.

- [11] Christoffer P. Nielsen and Henrik Bruus. Concentration polarization, surface currents and bulk advection in a microchannel. *Physical Review E*, 90(4):043020, August 2014.
- [12] Christoffer P. Nielsen and Henrik Bruus. Transport-limited water splitting at ion-selective interfaces during concentration polarization. *Physical Review E*, 89(4):042405, April 2014.
- [13] Victor V. Nikonenko, Anna V. Kovalenko, Mahamet K. Urtenov, Natalia D. Pismenskaya, Jongyoon Han, Philippe Sizat, and Gérald Pourcelly. Desalination at overlimiting currents: State-of-the-art and perspectives. *Desalination*, 342:85–106, June 2014.
- [14] Victor V. Nikonenko, Natalia D. Pismenskaya, Elena I. Belova, Philippe Sizat, Patrice Hugué, Gérald Pourcelly, and Christian Larchet. Intensive current transfer in membrane systems: modelling, mechanisms and application in electrodialysis. *Advances in colloid and interface science*, 160(1-2):101–23, October 2010.
- [15] Alexandre Persat, Robert D. Chambers, and Juan G. Santiago. Basic principles of electrolyte chemistry for microfluidic electrokinetics. Part I: Acid-base equilibria and pH buffers. *Lab on a chip*, 9(17):2437–53, September 2009.
- [16] Fredrik Persson, L. H. Thamdrup, M. B. L. Mikkelsen, S. E. Jaarlgard, P. Skafte-Pedersen, H. Bruus, and A. Kristensen. Double thermal oxidation scheme for the fabrication of SiO₂ nanochannels. *Nanotechnology*, 18(24):245301, June 2007.
- [17] I. Rubinstein, E. Staude, and O. Kedem. Role of the Membrane Surface in Concentration Polarization at Ion-Exchange Membrane. *Desalination*, 69:101–114, 1988.
- [18] Gilad Yossifon, Peter Mushenheim, Yu-Chen Chang, and Hsueh-Chia Chang. Nonlinear current-voltage characteristics of nanochannels. *Physical Review E*, 79(4):046305, April 2009.

Appendix A

1D Finite Element Code in Matlab

```
function [X,C]=FEM(N,L,BC1,BC2)
% Program by Rasmus Dybbro Engelholm to solve  $y''(x)+y(x)=0$  using the FEM.
% A function that takes inputs FEM(N,L,BC1,BC2) and gives an output, X,
% which is the basis function center coordinates and C, which is a
% vector with N elements containing the constant for each of the N basis
% functions, which is also the value of the solution function at that
% point. N is the number of basis functions or points. L is the length of
% the domain. BC1 is the value the function should take on the left
% boundary, while BC2 is the derivative it should have on the right
% boundary.

dx=L/N;      %Length between each mesh point

%Equation investigated:  $y''(x)+y(x)=0$ 
A=2/3*dx-2/dx;
B=dx/6+1/dx;

%Creating the matrix in sparse format: M.C=R
M=sparse(N,N);

for n=1:N
M(n,n)=A;
end
for n=1:N-1
M(n+1,n)=B;
M(n,n+1)=B;
end

% Setting axis
X=linspace(0,L,N)';
```

```
% BC 1: Set value in M
M(1,2)=0;

% BC 2: Set derivative in M
M(end,end-1)=-A;

%Set BC in result vector
R=sparse(N,1);
R(1,1)=A*BC1;
R(end,1)=A*BC2*dx;

%Solving problem:
C=M\R;

%Does BC match?
if full((C(end,1)-C(end-1,1))/dx) == BC2
    display('BC1 is matching')
end
if full(C(1,1)) == BC1
    display('BC2 is matching')
end
end
```

Appendix B

3D Images

In this appendix an image series to illustrate the differences between numerical model and real world system is shown. It starts from the simplest structure that can be fabricated (square channel with a narrow part) and ending in the structure that is the final model which is numerically investigated. First the flow channels are added, so that an imperfect reservoir can be modelled. Secondly the flow channels are rotated from the flat geometry that can be experimentally fabricated to the upright structure. If the channels are much wider than the smallest characteristic length, it is roughly translationally invariant in the width, and we can model it by a 2D cut.

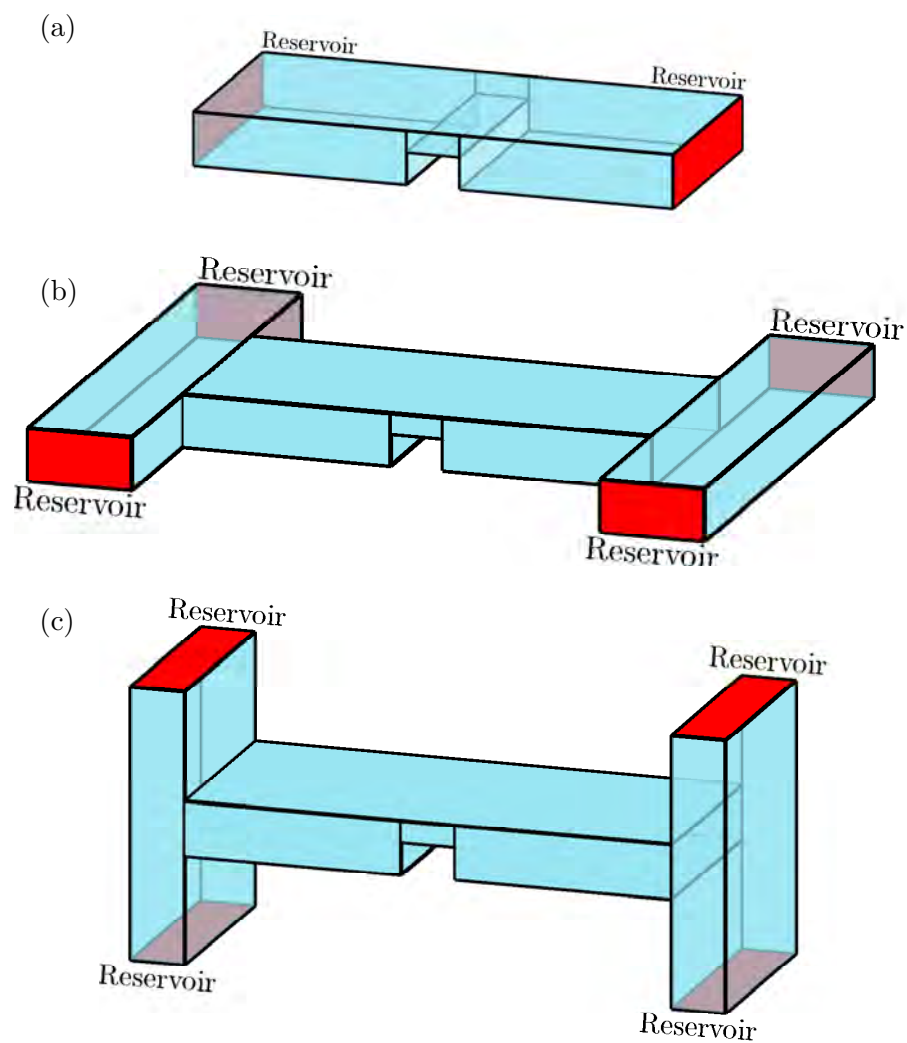


Figure B.1: Image series of the system ranging from the ideal system through the experimentally possible system to the numerically possible system. In the series the major steps are the nano channel as an ion selective membrane (a), the addition of flow control in the reservoirs (b), the rotation of the flow channels (c), which makes the figure translationally invariant in the third direction. The red color represents the reservoirs.